Deciphering Spatio-Temporal Variations in the Auroral Ionosphere using Magnetometer Data

Simon James Walker

Thesis for the degree of Philosophiae Doctor (PhD)
University of Bergen, Norway
2024

UNIVERSITY OF BERGEN

Deciphering Spatio-Temporal Variations in the Auroral Ionosphere using Magnetometer Data

Simon James Walker

Thesis for the degree of Philosophiae Doctor (PhD)
at the University of Bergen

Date of defense: 22.03.2024

Year: 2024

Title: Deciphering Spatio-Temporal Variations in the Auroral Ionosphere using Magnetometer Data

Name: Simon James Walker

Print: Skipnes Kommunikasjon / University of Bergen

Scientific environment

This research was conducted within the Department of Physics and Technology at the University of Bergen. It received funding from the Research Council of Norway as part of the Ionospheric Impact Response Analysis by Regional Information Integration (IIRARII) project, under the contract number 400844/F50. The thesis presented here is the culmination of work undertaken during my time as a member of the Birkeland Centre for Space Science (BCSS) Norwegian Centre of Excellence until its conclusion in 2023. Throughout this period I have also been a member of the Auroral Electrojet working group for NASA Electrojet Zeeman Imaging Explorer (EZIE) mission. I have also participated in a working group funded by the International Space Science Institute (ISSI): 'Understanding Mesoscale Ionospheric Electrodynamics Using Regional Data Assimilation'. Studies were complemented by a three-month research visit to the Finnish Meteorological Institute (FMI) in Helsinki.

Acknowledgements

The work for this thesis was conducted within the Dynamics of Asymmetric Geospace (DAG) group. I am deeply grateful to the entire group for their assistance, stimulating discussions, and the wonderful working environment provided during my three-year PhD journey.

A special thanks to my main supervisor, Kalle. For pushing me, securing funding for my position, and providing me with opportunities to work with diverse groups and projects. I am equally grateful to my co-supervisors, Jone and Spencer. I always enjoyed coming to your office to discuss new results or to get help to understand concepts. I particularly enjoyed the tangential discussions with Spencer because it always ended with new project ideas and greater understanding. On that note I must thank Kalle for his endless patience where he had to refocus us. I enjoyed sharing an office with Anders for the majority of my PhD which allowed us to discuss each other's work and ideas.

Despite COVID and living far from home, the support and encouragement from my family have helped me through the PhD. I started my university career 8 years ago in Aberystwyth and I do not think any of us would have predicted that I would complete a PhD.

Margot, your support during the intense weeks of writing this thesis was invaluable. Your help, encouragement, and cookies were the fuel that kept me going. I look forward to the opportunity to repay your kindness when you write your thesis.

Life on the fourth floor was made delightful by everyone's presence. The stress-relief, especially with Margot and Ingrid, often accompanied by gin, were much needed and deeply appreciated. A big thank you to Joe, Ingrid, Eldho, and Michael for the memorable activities outside work, from skiing, or at least falling down a slope wearing skis, to watching the barbie movie, I am still afraid to touch that pink glittery hat again now that everything has finally stopped being shiny.

My friends, both within and outside of work, have transformed Bergen into a cherished memory. The community at Hulen was a home away from home, and I am grateful to everyone who made me feel welcome in Norway. A special mention to my friend Chantelle: words cannot express how grateful I am, the help and support you have given during my PhD is immeasurable I certainly would not have made it here without you.

Lastly, I extend my gratitude to the Department of Physics and Technology. The opportunity to pursue my Masters and PhD here, along with engaging in outreach activities, has been a fulfilling experience.

Simon Walker
Bergen, January 2024

There was always a logical explanation for
everything, even if you had to make it up

Terry Pratchett

Abstract

The auroral ionosphere is a dynamic plasma environment dominated by the coupling of the solar wind plasma and magnetic field with the Earth's magnetosphere. The auroral displays, plasma motion and electric currents in the ionosphere are scaled and driven by the dayside coupling and the frequent transient explosive events on the nightside known as substorms. Historically, the electric currents in the polar ionosphere have been understood by the deflection of the magnetic field measured on the ground, and the overall auroral activity has typically been understood by the strength of this deflection. However, physics constrains the application of ground magnetometers for the study of the ionospheric electric currents. The magnetic field deflection underneath the layer of electric currents represents only a portion of the horizontal electric current in the ionosphere, typically referred to as the auroral electrojet. The advent of the space age has introduced magnetic field measurements above this layer of horizontal electric currents. Through these measurements, we can estimate the electric currents flowing along the magnetic field lines, called Birkeland currents, and the remaining horizontal current.

The work that makes up this thesis focuses on developing techniques that combine magnetic field measurements into a full picture of the ionospheric electric currents. In Paper I, we begin with combining measurements from ground magnetometers in Fennoscandia to robustly and routinely estimate the auroral electrojet current and the temporal derivatives of the magnetic field along a 1D slice where the estimations are considered most accurate. We use a technique that was developed for the NASA EZIE mission, that will be launched in the near future, and make remote measurements of the electrojet using the Zeeman effect. This study provides a unique dataset of these quantities between 2000 and 2020 to the scientific community. In this first paper, our primary focus is on the statistics of the dataset. We begin by validating it through comparison with an empirical model. More importantly, we explore the dependencies on local time, latitude and solar activity of large temporal derivatives in the radial magnetic field, which, prior to this study, had seen little attention. Large temporal derivatives in the magnetic field on ground have significant implications in terms of space weather as they can lead to the damage and destruction of modern infrastructure, such as power grids.

In Paper II, we continue with the dataset produced in Paper I, this time focusing on the electrojet currents we have estimated. Paper II is largely motivated by the necessity, for the field of space physics, of a global determination of the auroral oval, which has historically and in recent times presented a significant challenge. We design a routine to extract the properties of the electrojet currents such as their latitudinal extent and their total current strength. Using the latitudinal limits of the electrojets, we explore the collocation of the auroral oval with the electrojet. In particular, we build up a statistical picture in local time and latitude combining electrojet boundaries, measurements of auroral precipitating particles and auroral oval boundaries determined from satellite images. We conclude that there are clear trends between the auroral oval and the electrojet boundaries. Paper II motivates future work of estimating the global electrojet current and thus a global electrojet boundary. Such estimation is valuable for improving the statistical comparison with auroral imagery and determining an auroral oval proxy from electrojet boundaries.

In Paper III, we develop a robust and consistent methodology to directly estimate the full ionospheric portion of the substorm current wedge (SCW) using magnetometers on ground and on board the Iridium constellation of satellites. In contrast, previous studies have investigated this current system using only ground-based magnetometers. This is problematic as inferring the whole current system requires making the unrealistic assumption that gradients in the conductivity of the polar ionosphere in the region of the SCW are small. We investigate the formation, evolution and structure of the SCW to the extent permitted by the measurements. We also estimate the SCW using only ground magnetometers and make those strict assumptions about the conductivity, finding clear differences compared to the current wedge estimated from a combination of space and ground magnetometers. This comparison analysis shows that around the onset of a substorm the conductivity assumptions are invalid and the SCW structure cannot be inferred solely from ground-based magnetometers. Furthermore, we demonstrate that the intensification of the electrojet current, that is often used to infer the formation of the SCW, can occur without the formation of the SCW due to changes in the conductivity of the polar ionosphere associated with intense aurora. These results may have implications for the NASA EZIE mission, which will measure magnetic field perturbations that are located just beneath the ionosphere.

Abstrakt (Norsk)

Den polare ionosfæren er et dynamisk plasma-miljø dominert av koblingen mellom solvinden og jordens magnetosfære. Nordlyset, plasma-bevegelsen og elektriske strømmer i ionosfæren er skalert og drevet av dagsidekoblingen og de hyppige, kortvarige eksplosive hendelsene på nattsiden kjent som substormer. Historisk har de elektriske strømmene i den polare ionosfæren blitt forstått gjennom forstyrrelser i det magnetiske feltet målt på bakken, og den generelle nordlysaktiviteten har vanligvis blitt forstått ved styrken på denne forstyrrelsen. Fysikkens lover begrenser anvendelsen av bakkebaserte magnetometre for studier av de ionosfæriske elektriske strømmene. Magnetfeltforstyrrelsene under laget av elektriske strømmer representerer bare en del av den horisontale elektriske strømmen i ionosfæren, vanligvis kalt electrojet. Romalderen har gitt målinger av magnetfeltet over dette laget av horisontale elektriske strømmer. Gjennom disse målingene kan vi estimere de elektriske strømmene som flyter langs magnetfeltlinjene, kalt Birkelandstrømmer, og den gjenværende horisontale strømmen.

Arbeidet i denne avhandlingen fokuserer på å utvikle teknikker som kombinerer magnetfeltmålinger til et fullstendig bilde av de elektriske strømmene i ionosfæren. I Artikkel I kombinerer vi målinger fra bakkebaserte magnetometre i Fennoskandia for å estimere electrojeten og den tidsderiverte av det magnetiske feltet på en robust og rutinemessig måte langs en meridian der estimatene anses som mest nøyaktige. Vi bruker en teknikk som ble utviklet for NASA EZIE-misjonen, som vil bli skutt opp i verdensrommet i nær fremtid, og gjøre fjernmålinger av electrojeten ved hjelp av Zeeman-effekten. Denne studien genererer et unikt datasett av disse størrelsene mellom 2000 og 2020 tilgjengelig for det vitenskapelige samfunnet. I denne første artikkelen er vårt hovedfokus på statistikken til datasettet. Vi begynner med å validere det gjennom sammenligning med en empirisk modell. Viktigere er det at vi utforsker avhengighetene av lokaltid, breddegrad og solaktivitet av store tidsvariasjoner i det radielle magnetfeltet, som før denne studien hadde fått lite oppmerksomhet. Store tidsvariasjoner i magnetfeltet på bakken er et viktig aspekt av romvær ettersom de kan føre til skade og ødeleggelse av moderne infrastruktur, som strømnett.

I Artikkel II fortsetter vi med datasettet produsert i Artikkel I, denne gangen med fokus på elektrojetstrømmene vi har estimert. Artikkel II er i stor grad motivert av behovet for en global bestemmelse av nordlysovalen, som historisk og i nyere tid har vist seg å være utfordrende. Vi utvikler en rutine for å bestemme egenskapene til electrojetstrømmene, som deres breddegradsutstrekning og deres totale strømstyrke. Ved bruk av breddegradsgrensene for electrojetene utforsker vi samlokaliseringen av nordlysovalen med electrojetten. Spesielt bygger vi opp et statistisk bilde i lokaltid og breddegrad som kombinerer electrojetgrenser, målinger av partikkelnedbør og nordlysgrenser bestemt fra satellittbilder. Vi konkluderer med at det er klare sammenhengenger mellom nordlyovalen og electrojetgrensene. Artikkel II skaper grunnlag for fremtidig arbeid med å estimere den globale electrojeten og dermed en global electrojetgrense. En slik estimering vil være verdifull for å forbedre den statistiske sammenligningen med nordlysbilder og bestemme en nordlysoval-proxy fra electrojetgrenser.

I Artikkel III utvikler vi en robust og konsistent metodikk for å direkte estimere den fullstendige ionosfæriske delen av substorm-strømkilen (substorm current wedge, SCW) ved bruk av magnetometre på bakken og ombord på Iridium-satellittkonstellasjonen. Tidligere studier har hovedsakelig undersøkt dette strømsystemet kun ved bruk av bakkebaserte magnetometre. Dette er problematisk ettersom det å avlede hele strømsystemet krever urealistiske antagelser om ledningsevnen i ionosfæren. Vi undersøker dannelsen, utviklingen og strukturen til SCW så langt som målingene tillater. Vi estimerer også SCW ved bruk av bare bakkebaserte magnetometre, og finner tydelige forskjeller sammenlignet med SCW estimert fra en kombinasjon av rom- og bakkebaserte magnetometre. Denne sammenligningsanalysen viser at rundt begynnelsen av en substorm er ledningsevneantakelsene ugyldige og SCW-strukturen kan ikke utledes utelukkende fra bakkebaserte magnetometre. Videre demonstrerer vi at intensiveringen av electrojeten kan skje uten dannelsen av SCW på grunn av endringer i ledningsevnen til den polare ionosfæren assosiert med kraftig nordlys. Disse resultatene kan ha implikasjoner for NASA EZIE-satellittene, som vil måle magnetfeltforstyrrelser fra et område rett under ionosfæren.

Outline

This thesis consists of three papers, an introduction to the background theory that is relevant to the studies in the three papers, a detailed description of the data and methodology used in these studies and discussion on how the research in the thesis could be developed further.

The papers included in this thesis are:

1. S.J. Walker, K.M. Laundal, J.P. Reistad, A. Ohma, S.M. Hatch, (2023) *Statistical Temporal Variations in the Auroral Electrojet Estimated With Ground Magnetometers in Fennoscandia*, Space Weather **Volume: 21**
2. S.J. Walker, K.M. Laundal, J.P. Reistad, A. Ohma, S.M. Hatch, G. Chisham, M. Decotte, (2023) *A comparison of auroral oval proxies with the boundaries of the auroral electrojets*, Space Weather (in review, October 2023)
3. S.J.Walker, K.M. Laundal, J.P. Reistad, S.M. Hatch, A. Ohma, J. Gjerloev, (2024) *The Ionospheric Leg of the Substorm Current Wedge: Combining Iridium and Ground Magnetometers*, JGR Space Physics (in review, January 2024)

Through the course of this PhD I have also contributed to these papers:

A K.M. Laundal, J.P. Reistad, S.M. Hatch, M. Madelaire, S.J. Walker, A.Ø. Hovland, A. Ohma, V.G. Merkin, K.A. Sorathia, (2022) *Local Mapping of Polar Ionospheric Electrodynamics*, JGR Space Physics **Volume: 127**

B A.Ø. Hovland, K.M. Laundal, J.P. Reistad, S.M. Hatch, S.J. Walker, M. Madelaire, A. Ohma, (2022) *The Lompe code: A Python toolbox for ionospheric data analysis*, Frontiers in Astronomy and Space Sciences **Volume: 9**

C L. Juusola, A. Viljanen, N. Partamies, H. Vanhamaki, M. Kellinsalmi, S. Walker, (2023) *Three principal components describe the spatiotemporal development of mesoscale ionospheric equivalent currents around substorm onsets*, Annales Geophysicae **Volume: 41**

D A. Ohma, M. Madelaire, K.M. Laundal, J.P. Reistad, S.M. Hatch, S. Gasparini, S.J. Walker, (2023) *Background removal from global auroral images: Data driven dayglow modelling*, Earth and Planetary Physics **Volume: 8**

Contents

Chapter 1

Introduction

The heliosphere encompasses the solar system and is filled with a supersonic plasma known as the solar wind, emanating from the solar corona, and an interplanetary magnetic field (IMF) which is frozen into the solar wind and dragged away from the Sun. These elements collectively shape and control the Earth's magnetosphere and plasma environments. The dynamics of the solar wind and IMF and their coupling with the magnetosphere-ionosphere system are responsible for space weather (*Lockwood*, 2022).

Space weather makes up a range of interconnected phenomena that have far-reaching consequences on the technologies that make up the modern world. The longest observed space weather phenomena are the brilliant displays that make up the aurora borealis and aurora australis. These impressive lights are the result of energetic protons and electrons flowing along magnetic field lines impacting and exciting gas in the upper atmosphere. The extent and location of the aurora is dictated by the coupling of the IMF with the magnetosphere. For stronger coupling, the aurora reaches lower latitudes and is brighter and more dynamic (*Han et al.*, 2020).

When the IMF encounters the Earth's magnetic field, it may connect with the magnetic field lines in the dayside magnetosphere. This opens the magnetosphere, allowing solar wind plasma to enter the dayside polar atmosphere which typically generates weak aurora (*Mende et al.*, 2016). The solar wind remains frozen to the opened magnetic field lines and carries it into the nightside magnetosphere. This process stores magnetic energy in the nightside magnetic field (*Milan et al.*, 2007). This energy is released when the magnetic field lines of the magnetosphere become "closed" where they are no longer connected to the IMF. This allows the magnetic field lines to return to the dayside magnetosphere. These steps, and thus the coupling of the IMF and the Earth's magnetic field, create a circulation of magnetic field lines through the polar atmosphere that in turn creates a circulation of plasma (*Dungey*, 1961). The motion of magnetic flux and plasma and the solar wind coupling with the magnetosphere generates electric currents flowing horizontally through the polar atmosphere and vertically along magnetic field lines in and out of the polar atmosphere (*Milan et al.*, 2017).

The more intense and commonly observed aurora appears in the regions where the magnetic field is no longer connected to the IMF and is circulating towards the dayside. This aurora is a consequence of the processes surrounding the release of magnetic energy in the nightside magnetosphere, where charged particles are accelerated towards the polar atmosphere. The region where these aurora occur is called the auroral oval.

Its latitudinal extent holds key information on the opening and closing of magnetic flux and the amount of magnetic energy stored in the magnetotail (*Chisham et al.*, 2022; *Milan et al.*, 2008, 2017). Furthermore, in this region space weather hazards are greater. For example precipitating energetic particles may lead to a charge buildup in certain regions of a spacecraft. Subsequent discharges from the resulting potential difference may lead to minor and major failures in the satellite (*Anderson and Koons*, 1996).

The auroral oval is also the region where the electric currents and magnetic field disturbances are strongest and can vary significantly. This creates another space weather hazard. One immediately recognisable hazard is how the varying magnetic field presents a challenge when using the magnetic field for navigation. Simply put, a compass needle will no longer point towards magnetic north and the stronger the variation in the electric current the more variable the pointing of the needle. Furthermore, Faraday's law tells us that a varying magnetic field will induce a current in the ground or conductive materials. Thus, variations of the ionospheric currents can also induce a secondary current directly into networks of cables or an induced current in the ground can short circuit through the cables (*Boteler*, 2019; *Ebihara et al.*, 2021). Famously, during intense auroral activity in 1859, telegraph workers disconnected the power from the network to prevent any damage and found operators could still communicate up to two hours using purely the current induced in the wires (*Green et al.*, 2006). These currents have also been responsible for damage to power grids, degradation of pipes and much more (*Boteler*, 2019; *Taltavall*, 1915) and are thus a significant space weather hazard.

We can use measurements of the magnetic field to study ionospheric currents. At high latitudes, the field-aligned current (FAC) and a portion of the horizontal current create no magnetic field on the ground. The portion of the horizontal current that does create a magnetic field on the ground is called the auroral electrojet. By combining ground magnetic field measurements we can robustly estimate the auroral electrojet and understand where the large-scale electrojet current is located with respect to the auroral oval (*Feldstein et al.*, 1999). We can also study the magnetic field responsible for some of the space weather hazards described in the previous paragraph.

Using space-based magnetometers we can utilise the magnetic field measurements to study the field-aligned and the associated part of the horizontal current. The Iridium satellites are ideal for this due to their large coverage. The Active Magnetosphere and Planetary Electrodynamics Response Experiment (AMPERE) project showed that despite the noisy magnetic field measurements made by the Iridium constellation compared to science grade magnetometers, the large-scale FACs can be estimated routinely using a ten minute window of data (*Anderson et al.*, 2000, 2014; *Coxon et al.*, 2018; *Waters et al.*, 2020). However, the magnetic field from the auroral electrojets cannot be measured using the magnetometers on board the Iridium satellites but by combining space-based and ground-based magnetometers we can measure the total ionospheric current (*Green et al.*, 2007).

Explosive events known as substorms involve large releases of magnetic energy in the nightside magnetosphere (*Milan et al.*, 2006). The consequences are bright and dynamic aurora and a current system called the substorm current wedge (SCW). The SCW consists of FACs connecting the polar atmosphere to the nightside magnetosphere and horizontal currents in the polar atmosphere that connect the FACs (*McPherron et al.*, 1973). This current is poorly understood, and a number of competing theories about its formation and structure exist (*Gjerloev and Hoffman*, 2014; *Liu et al.*, 2013; *McPherron et al.*, 1973). Through using new techniques we can estimate in a consistent and robust manner this full current system using a combination of magnetic field measurements from the ground, to estimate the electrojet current, and Iridium, to estimate the field-aligned and associated part of the horizontal current (*Green et al.*, 2007).

There are **two main objectives** of this thesis. **The first objective** is to develop robust methodologies for estimating ionospheric currents using ground and space based magnetometers. **The second objective** is, through these estimations, to understand the extent to which ground magnetometers can be used to infer the properties of the SCW and the auroral oval.

This introduction gives context and highlights the motivation of this thesis. The core concepts and background theory are presented in Chapter 2 and 3. The core data used in the papers constituting this thesis are introduced in Chapter 4 as well as the steps that are taken from the raw measurements to the measurements used in the studies. The methodology relevant to these studies is described in detail in Chapter 5. A brief summary of the papers is provided in Chapter 6. Eventually, the studies and thesis are concluded in Chapter 7. Further development and application of the work is described in Chapter 8.

We conclude this introductory chapter by emphasising the purpose and objectives of the three papers that make up this thesis. Paper I focuses on a high density network of ground magnetometers in Fennoscandia using spherical elementary current systems and a similar inversion scheme to *Laundal et al.* (2022), which was designed for estimating currents from noisy remote magnetic field measurements with the Electrojet Zeeman Imaging Explorer (EZIE) satellite mission. We aimed to estimate the electrojet current along a magnetic meridian in Fennoscandia in a consistent and temporally comparable manner. Producing a dataset that spans two decades we demonstrate the advantages of combining magnetometers into a single inversion and how it can be used to investigate the temporal derivative in the radial magnetic field. We aimed to find latitude and local time hot spots for large temporal derivatives. We also aimed to show how the solar cycle modulates the occurrence of these large temporal derivatives. We also demonstrate how the dataset can be used to depict spatio-temporal variations of waves in the magnetic field.

In Paper II our objective was to extract properties of the electrojet from the dataset produced in Paper I, with particular focus on the boundaries of the electrojet. From these boundaries we aimed to understand the collocation of the electrojets and the auroral oval by comparing the electrojet-derived boundaries with boundaries based on auroral images and precipitation measurements. This work is relevant for a potential future application in which ground magnetometers are used to infer the location of the auroral zone globally.

One objective of Paper III is to estimate the full ionospheric current using ground and Iridium satellite based magnetometers. Contrary to a number of other assimilation techniques (such as *Richmond* (1992), *Laundal et al.* (2022) and *Kamide et al.* (1981)) we focus purely on magnetic field measurements and do not require estimates of the conductance. Making adaptions and developments to the inversion technique used in Paper I, we aimed to investigate the SCW by analysing the full estimated current during substorms with onset close to the centre of the analysis region. This allows us to also investigate the limitations of ground magnetometers when describing FACs; having estimated the FACs directly using space based magnetometers we compare them with the *equivalent* FACs determined from ground magnetometers. Such equivalent FACs have been interpreted as actual FACs in prior research (*Nishimura et al.*, 2020; *Weygand and Wing*, 2016; *Weygand et al.*, 2021). We aimed to determine where and when the equivalent FACs are a reasonable proxy for the FACs, and in particular how well the SCW can be quantified using only ground based magnetometers (*Gjerloev and Hoffman*, 2014). This is also relevant for the upcoming Electrojet Zeeman Imaging Explorer mission (EZIE), that will measure the magnetic field at approximately 80 km, as it will only be able to study the SCW through the equivalent FAC method. We return to the details of the relevance of the EZIE mission in Chapter 8.

Chapter 2

Space Physics Background

In this chapter we introduce the core theory of space physics applicable to this thesis, with particular attention to the nature and consequences of solar wind-IMF-magnetosphere-ionosphere coupling. This chapter covers the background necessary to understand the fundamental aspects of the current systems we discuss in Chapter 3, and introduces core concepts in greater detail than is provided in the papers that make up the main results of this thesis.

2.1 The Polar Ionospheric Plasma

The term ionosphere describes the portion of the atmosphere comprised of a quasi-neutral plasma. The plasma is generated primarily through photo-ionisation and as such the plasma density is strongly linked to solar illumination (*Chapman and Bartels*, 1962; *Rishbeth and Garriott*, 1969). Globally this leads to variations in the plasma density correlated with the solar cycle. In polar regions there are strong seasonal variations in the plasma density due to prolonged solar illumination in the summer and the lack of solar illumination in the winter.

Figure 2.1 shows the altitude profile of the conductivity of the ionosphere under sunlit conditions. The Pedersen and Hall conductivity, which is the horizontal conductivity parallel and perpendicular to the electric field respectively, peak between 100 and 130 km. Therefore, the majority of the horizontal ionospheric currents flow at these altitudes. The parallel conductivity is much higher (i.e., charged particles are much more mobile along field lines). All of these conductivities are greatly diminished below 80 km. Therefore, the majority of field-aligned currents diverge into the horizontal current in the same 100 to 130 km segment. Due to the nature of how we typically measure the auroral ionospheric currents, which we return to in Chapter 3, its three-dimensional nature is hard to investigate. Therefore, we often describe the horizontal ionospheric currents as being in a two dimensional sheet and the field aligned currents as having an unchanging magnitude above this sheet and being zero below (*Chapman and Bartels*, 1940; *Green et al.*, 2007; *Untiedt and Baumjohann*, 1993; *Vanhamäki and Juusola*, 2020). In this description conductivity is height integrated and referred to as the conductance with the same Hall, Pedersen and field-aligned decomposition. These details are returned to in section 3.1 where ionospheric Ohm's law is introduced.

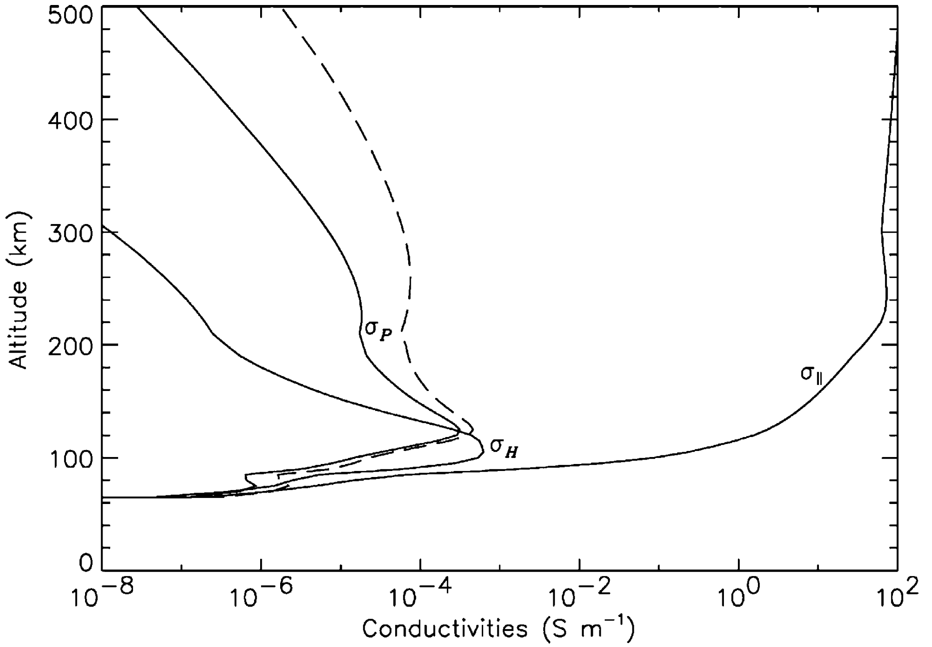

Figure 2.1: Altitude profile of the Hall (σ_H), Pedersen (σ_P) and parallel ($\sigma_\parallel$) conductivity at low latitude during solar minimum. Dashed line shows the Pedersen conductivity at solar maximum. Figure taken from Richmond (2007)

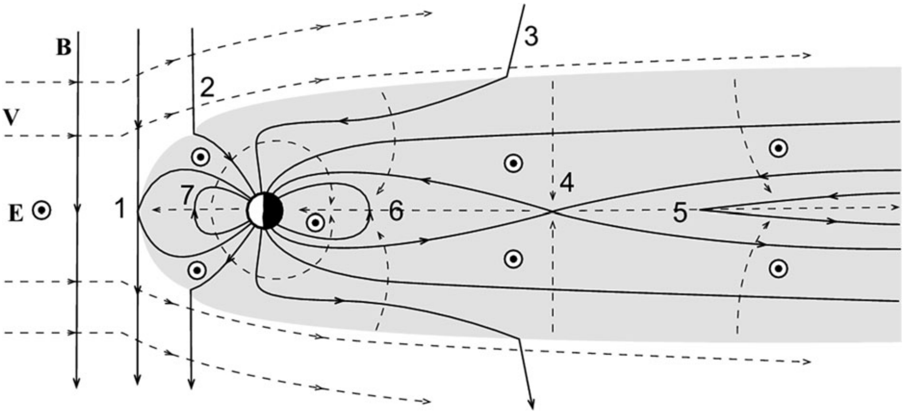

Figure 2.2: Schematic of the Dungey cycle taken from Seki et al. (2015)

In the polar ionosphere there is another significant source of ionisation and consequently a source of change in conductance (*Robinson et al.*, 1987). Precipitating energetic particles, which intensify during magnetic substorms that are discussed in section 2.3, impact and excite the auroral ionosphere. The relaxation of the exited atoms is responsible for the famous auroral displays known as the aurora borealis and aurora australis.

2.2 The Solar Wind Driving of the Magnetosphere and Polar Ionosphere

The interaction and coupling of the solar wind and IMF with the magnetosphere heavily dictate the dynamics of the polar ionosphere. In this section we summarise how the solar wind driving controls motion of the ionospheric plasma and magnetic flux.

2.2.1 Solar Wind-Magnetosphere Coupling

The solar wind is a quasi-neutral supersonic plasma emanating from the solar surface and due to certain magnetohydrodynamic (MHD) conditions the Sun's magnetic field is frozen into the solar wind and is dragged out into interplanetary space. Upon arrival at the Earth's magnetopause the orientation of the IMF is of significant importance for the interaction between the IMF and the magnetopause. A purely southward IMF is anti-parallel to the magnetosphere and, due to pressure from the solar wind and pressure from within the magnetosphere, magnetic re-connection can take place. This is a process where an in-flow of IMF magnetic flux re-configures to be connected to the Earth's magnetic field with orthogonal out-flowing reconnected magnetic flux. In space plasma physics we use the term "open magnetic field" to describe magnetic field lines connected to both the Earth's magnetic field and the IMF. A "closed magnetic field" is used to describe magnetic field lines with both footpoints on the Earth.

There have been numerous attempts to describe the relative contribution of different factors to the rate of magnetic re-connection at the subsolar magnetopause (*Lockwood*, 2022; *Milan et al.*, 2012). A commonly used proxy is the *Newell et al.* (2007) coupling function:

$$\varepsilon_N = v^{4/3}\left(\sqrt{B_y^2 + B_z^2}\right)^{2/3} \sin^{8/3}(\theta/2), \tag{2.1}$$

where v is the solar wind speed, B_y and B_z are components of the IMF in the geocentric solar magnetospheric (GSM) co-ordinate system and $\theta = \arctan2(B_y, B_z)$ is the IMF clock angle (*Newell et al.*, 2007). Although ε_N is not a measure of the subsolar magnetopause reconnection rate it is considered to be a good proxy. ε_N or similar functions are used in numerous models and predictions of auroral ionospheric dynamics and as a quantity to indicate activity levels. Given that the long term trends in IMF magnitude and the solar wind speed are correlated with the solar cycle, the reconnection rate and ε_N will also exhibit the solar cycle (*Newell et al.*, 2007).

When the IMF is oriented northward, $\sin^{8/3}(\theta/2)$ is zero and thus the rate of reconnection at the subsolar magnetopause is zero. However, there is still a coupling between the IMF and the magnetosphere. A northward oriented IMF can drape over the dayside magnetosphere and reconnect with the magnetic field lines in the lobes. Overall magnetic activity is significantly weaker during this coupling and has different consequences on the ionosphere.

The coupling function has a number of further limitations. Firstly, there are challenges surrounding the measurements of the properties of the solar wind and IMF. There are three solar wind monitors with halo orbits around the first Lagrangian point approximately 230 RE away from the Earth (1.5 million km) in the direction of the Sun. The Advanced Composition Explorer (ACE), the Deep Space Climate Observatory (DSCOVR) satellite and the Wind satellite. The nature of the orbits move them out of the Sun-Earth line: for Wind R$_{ZY}$ in geocentric solar ecliptic co-ordinates can be up to 100 R_E, for DSCOVR 50 R_E and ACE 40 R_E (*Borovsky*, 2008; *Lockwood*, 2022). This presents the problem that regardless of whether the time shifting of the measurements to the bow shock is accurate, the solar wind measured by these satellites is not the same solar wind that reaches the bow shock. The time shifting of the solar wind measurements is determined by the measured solar wind velocity, and is typically 40–50 minutes (*King and Papitashvili*, 2005). A second problem is what happens to the solar wind between the bow shock and the subsolar magnetopause. This plasma regime is turbulent and without measurements within this region we cannot always accurately predict the IMF magnetosphere coupling due to variations in the orientation of the IMF compared to what arrives at the bow shock.

2.2.2 Plasma Circulation in the Magnetosphere-Ionosphere System

The Dungey cycle is a simplistic steady state model where flux is constantly opened at the subsolar magnetopause by a southward oriented IMF and closed in the night side at the same rate (*Dungey*, 1961). Figure 2.2 shows the stages of the Dungey cycle where **1** marks the beginning of the cycle as an opening of magnetic flux at the subsolar magnetopause. This opening allows solar wind particles to enter the cusp, ionising a portion of the dayside ionosphere and can create dayside aurora (*Mende et al.*, 2016). The opened flux is then pulled across the polar cap (steps **2** and **3**), stimulating anti-sunward plasma motion due to the frozen-in condition. The open flux is then dragged into the magnetotail where it eventually reconnects (step **4**). A plasmoid then moves away from the Earth (step **5**) while the closed magnetic field dipolarises (towards step **6**) and the release of stored magnetic energy is transferred to the magnetotail plasma which precipitates leading to the processes discussed in Section 2.1. Once dipolarised (step **6**) the magnetic flux convects across the dawn and dusk flanks to the dayside and stimulates plasma motion (step **7**). Since the space plasma and magnetic fields move together in the magnetosphere, solar wind and the ionosphere, the global scale plasma circulation at high latitudes resembles a footprint of the Dungey cycle as described in the magnetosphere. This is shown in Figure 2.3 using black lines with arrows.

The plasma circulation during northward IMF is not captured by the Dungey cycle. A northward IMF does not reconnect at the subsolar magnetopause. IMF field lines are draped across the magnetosphere and reconnect with the field lines in the lobes as they are anti-parallel along the Sun-Earth line. Such interactions drive much weaker convection cells concentrated in the polar cap with anti-sunward motion at the centre of the cap and sunward motion on the edges (*Reistad et al.*, 2021).

The east-west component of the IMF also has a strong influence on the convection pattern as it influences the location of reconnection. During a southward IMF this compresses one cell and exaggerates the other. During a northward IMF a strong By component can reduce convection to a single cell. The strength of convection is also controlled by the dipole tilt due to effect on the location of reconnection and due to changes in solar illumination (*Pettigrew et al.*, 2010).

2.2.3 Expanding Contracting Polar Cap Paradigm

To maintain a steady state of opening and closing of flux in the Dungey cycle there has to be a constant population of open field lines convecting across the polar cap and closed field lines around the flanks. This description is not entirely accurate as it assumes a constant southward IMF and simplifies the magnetotail behaviour; topologically there is a distinct boundary that separates the open and closed field lines (OCB), shown as a red line in Figure 2.4. The polar cap (**P** in Figure 2.4) is the area of open flux. There is a second boundary in Figure 2.4 that describes the low latitude extent of auroral activity. The region contained within these two boundaries is know as the auroral oval (**A** in Figure 2.4) and describes the extent of energetic particle precipitation on closed field lines. Precipitation in the auroral oval and polar cap are typically of different energies as the magnetic field lines map to different regions of the magnetosphere and therefore different plasma populations (*Newell et al.*, 1996).

The typical description of the Dungey cycle assumes that the rate of reconnection is the same at the subsolar magnetopause and in the magnetotail. However, in reality they can be very different and this controls the latitude of the OCB. When reconnection occurs on the dayside it can cause a protrusion of the polar cap into the auroral oval, as shown by the hashed area in panel b of Figure 2.4, and when reconnection occurs on

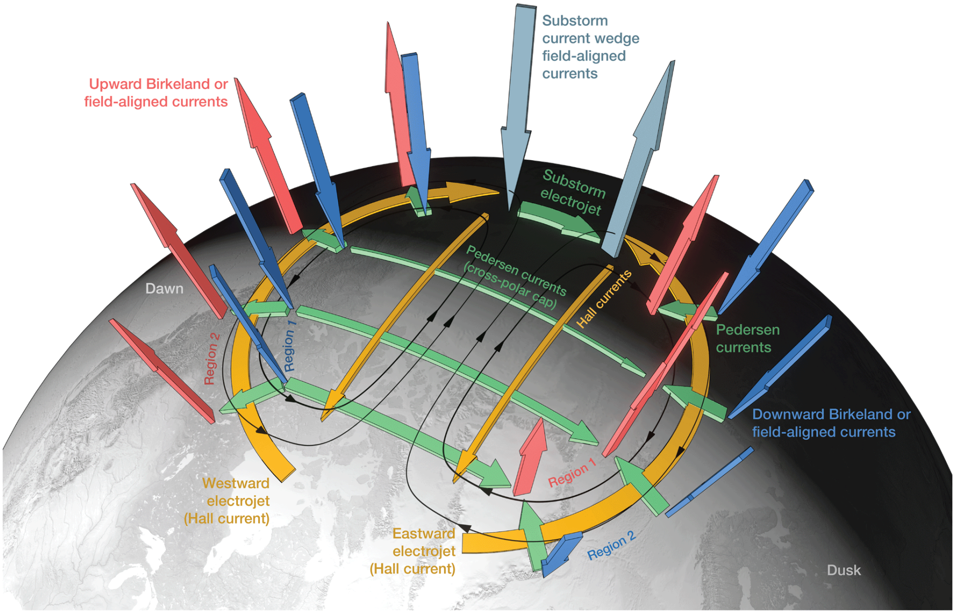

Figure 2.3: Figure demonstrating the Dungey cycle convection pattern (black arrows and lines) and polar ionospheric current systems taken from Palmroth et al. (2021).

the nightside the auroral oval protrudes into the polar cap, as shown by the hashed area in panel a of Figure 2.4. Over time, if the reconnection rate on the dayside is greater than on the nightside the polar cap increases in size. For the reverse the polar cap shrinks. Tracking the change in the area of the polar cap is considered to be currently one of the most accurate ways of determining the difference between the dayside and nightside reconnection rate. As we will discuss further in the Section 2.3, convection of open flux into the tail does not immediately instigate reconnection on the nightside. Therefore, calculating the amount of open flux can inform us of the extent of the loading of magnetic flux in the magnetotail (*Milan*, 2004).

The equatorward boundary of the auroral oval is also an important quantity because by defining the full extent of the auroral oval we describe the region of the magnetic field that takes part in the high latitude electrodynamics, including strong energetic particle precipitation and significant ionospheric currents (*Burrell et al.*, 2020; *Kilcommons et al.*, 2017; *Redmon et al.*, 2010). The equatorward boundary generally moves similarly to the polar cap boundary, i.e. as the polar cap expands the equatorward boundary of the auroral moves to lower latitudes and when it shrinks the equatorward boundary moves to higher latitudes. However, their motion is not necessarily synchronised. Typically the poleward boundary evolves on shorter time scales than the equatorward boundary (*Ohma et al.*, 2023). Defining the area covered by the auroral oval informs us of where space weather hazards are heightened and thus is important for managing a large variety of modern space- and ground-based technologies.

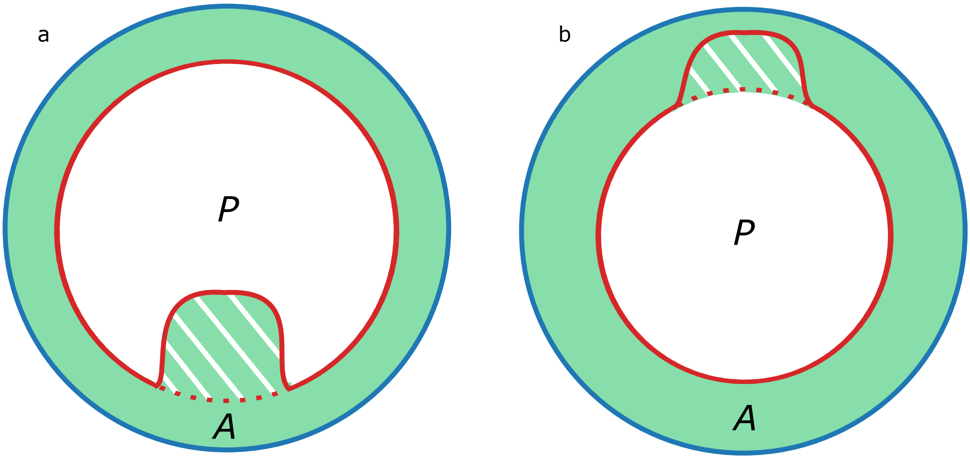

Figure 2.4: Figure demonstrating the expanding contracting polar cap paradigm taken from Ohma et al. (2023). Green represents closed magnetic flux and white represents open magnetic flux. A is the auroral oval and P is polar cap. The red line is the open close field line boundary and blue is equatorward boundary of the auroral oval.

2.2.4 Finding The Auroral Oval

Often, the poleward boundary of the global auroral oval can be a good proxy of the OCB (*Longden et al.*, 2010; *Sotirelis et al.*, 2005). The most direct way to identify the auroral oval is through measuring the precipitation as the plasma in different magnetosphere regions have significantly different precipitation characteristics (*Andersson et al.*, 2004; *Kilcommons et al.*, 2017; *Newell et al.*, 1996). *Kilcommons et al.* (2017) used the special sensor J (SSJ) particle detector on the Defense Meteorological Satellite Program (DMSP) satellites to define when the satellite was within the auroral oval. They define auroral precipitation as an integrated energy flux of electrons with kinetic energy between 1.3 and 30 keV that exceeds 10^9 eV/cm^2/s/sr. The poleward and equatorward extent of regions comprised of auroral precipitation then defines the auroral oval. However, the measurements by the DMSP satellites are 1-dimensional along the satellite orbit with typically large temporal and spatial gaps and thus it is not possible to use this approach to characterise the global auroral oval, except for in climatological average models. Additionally, the orbits of the DMSP satellites have significant biases in local times and there can be a large orbital angle with respect to the auroral oval or even cases where they do not enter the polar cap leading to poor boundary detection (*Decotte et al.*, 2023).

Satellite based auroral imagery has significant advantages over the approach of measuring the precipitation. The larger field of view can capture more of the auroral oval. The missions with the largest advantage over other approaches are those than can image the entire auroral oval within one image such as the Imager for Magnetopause-to-Aurora Global Exploration (IMAGE) satellite and the Polar satellite.

Figure 2.5 shows the detection of the auroral oval based on images from the Wideband Imaging Camera (WIC) onboard the IMAGE satellite, which is most sensitive to emissions due to electron precipitation, over a period of almost 7 hours (*Ohma et al.*, 2023). The nature of the orbit allows for long periods of continual observation of the polar ionosphere. This makes it ideal not only for capturing the entire auroral oval but also to study its evolution throughout the period of a substorm (introduced in the next section). The auroral boundaries identified through images are not exactly the same as those obtained using particle precipitation measurements and in *Longden et al.* (2010) they adjust these boundaries using a local time dependent systematic offset from those obtained using DMSP based on statistics from conjunctions (*Chisham et al.*, 2022; *Ohma et al.*, 2023). Despite the systematic differences, the auroral boundaries determined from global auroral imagery serve as a good proxy for monitoring changes in the inferred polar cap and auroral zone extent with high temporal resolution.

Figure 2.5 shows that the auroral oval is not always clearly delineated in auroral images, here based on WIC. The last two panels show that the auroral emissions are not distinguishable above the dayglow on the dayside. When approached algorithmically, studies such as *Chisham et al.* (2022); *Longden et al.* (2010) often discard dayside boundary estimates. Particularly for the last two panels, where it would be challenging to even draw boundaries by eye on the dayside. Figure 2.5 shows global boundaries even for the last two images however this is due to the approach in *Ohma et al.* (2023) which involves a global fit of initial boundaries determined from pixel intensity profiles. As a result the dayside equatorward boundary is primarily dictated by a sophisticated temporal and spatial interpolation from nearby boundaries.

The largest challenge for this approach to determining the auroral oval is the scarcity of satellites capable of global auroral imagery. At the time of this thesis it has been over a decade since the last mission to image the entire auroral oval. Furthermore, continual global auroral imagery has not been available during any of the global auroral imagery missions. We discuss this challenge and investigate a different approach using high latitude ground magnetometers that measure the ionospheric current in the auroral ionosphere to obtain an auroral oval proxy in Paper II. An approach using ground magnetometers has a significant advantage over the others mentioned in this section due to continual operation in the auroral zone, longevity of operation (ground magnetometers are one of the oldest measurements of the polar ionospheric dynamics) and thanks to large networks temporal and spatial data gaps have a limited impact. The largest challenge is the indirectness of the measurement in relation to precipitation.

2.3 Substorms

While the Dungey cycle model can explain a large amount of polar ionospheric dynamics, its simplistic and steady state nature falls short of capturing several aspects of the behaviour of the magnetotail. Open flux entering the magnetotail does not immediately reconnect and close. The onset of a substorm is associated with the eventual near Earth reconnection in the tail, leading to a release of energy and the dipolarisation of the stretched magnetic field lines (*Angelopoulos et al.*, 2008; *Juusola et al.*, 2011). This has significant dynamic consequences on the auroral ionosphere in terms of energetic particle precipitation, plasma convection and the ionospheric current systems. This section describes the typical substorm, highlighting how its progression has historically been identified.

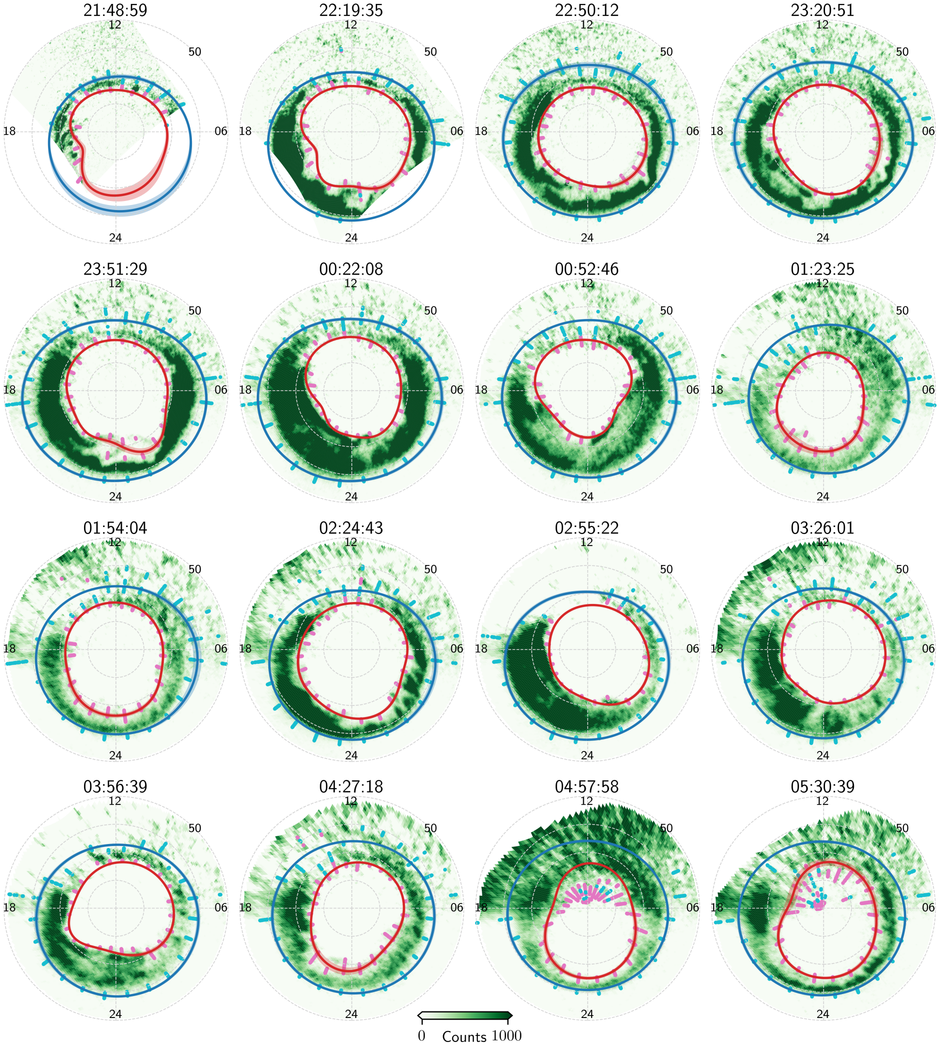

Figure 2.5: Time evolution of the auroral oval using images from the IMAGE satellite taken from Ohma et al. (2023). The red line is the poleward boundary of the auroral oval and the blue line is the equatorward boundary.

2.3.1 The Phases of a Substorm

Substorms are best explained through their phases. *McPherron* (1970) describes three substorm phases: growth, expansion and recovery. Historically, the phases of substorms have either been defined through observations of the visible aurora or the variation of the magnetic field measured on ground (*Akasofu*, 1964). The typical growth phase diverges from the Dungey cycle. Instead of open flux moving into the magnetotail and there immediately undergoing reconnection, the magnetotail becomes loaded with open flux. Typically there must be a southward IMF for around 30 minutes to load enough flux into the magnetotail, however, the time history of the IMF may reduce the necessary period (*Juusola et al.*, 2011; *Partamies et al.*, 2013). In auroral zone magnetometers on the night side the growth phase can be observed as a slight increase in the northward component which is related to the thinning of the magnetotail current sheet (*Runov et al.*, 2021). In Figure 2.6 the increase in the northward component is small and appears shortly before the onset. In visible aurora, observations of the growth phase can be identified by the relatively slow equatorward motion of auroral arcs and diffuse aurora (*Akasofu*, 1964).

The growth phase ends as reconnection begins in the magnetotail, closing the loaded open flux. The onset is regarded as the singular point where the growth phase ends and the expansion phase begins and is identified by the first signatures of the expansion phase. This first signature varies in time depending on the chosen observational data and thus the onset can be inconsistent (*Juusola et al.*, 2011). In ground magnetometers the signature is a sudden intensification of the westward electrojet which, as shown in Figure 2.6, is observed as a sharp decrease in the northward component. Auroral observations show a sudden localised brightening at the equatorward edge of the auroral oval. The onset marks the start of the expansion phase which covers the most dynamic and intense auroral activity of the substorm. Figure 2.6 shows that the westward electrojet continually strengthens during the expansion phase. Overall, the expansion phase involves an intensification of ionospheric currents and numerous dynamic arcs with significant motion (*Akasofu*, 1964). The most intense auroral precipitation is concentrated within the auroral bulge. The expansion phase has a typical length of 20-30 minutes (*Partamies et al.*, 2013).

The recovery phase is the final phase and represents a relaxation of the magnetosphere. The magnetotail reconnection rate reduces, and auroral activity weakens (*Juusola et al.*, 2011). Figure 2.6 shows the recovery phase as a decaying northward component and thus a decaying electrojet strength. In the recovery phase omega band auroral structures can appear and the overall dynamics and brightness of the aurora also decays (*Akasofu*, 1964). The recovery phase can last up to three hours. Typical lengths are at least an hour (*Partamies et al.*, 2013). The end of the recovery phase represents a return of the system to the state before the substorm, as shown in Figure 2.6 where the northward component approaches 0 nT. It is not uncommon that a new substorm commences before the end of the recovery phase, particularly during periods of high activity.

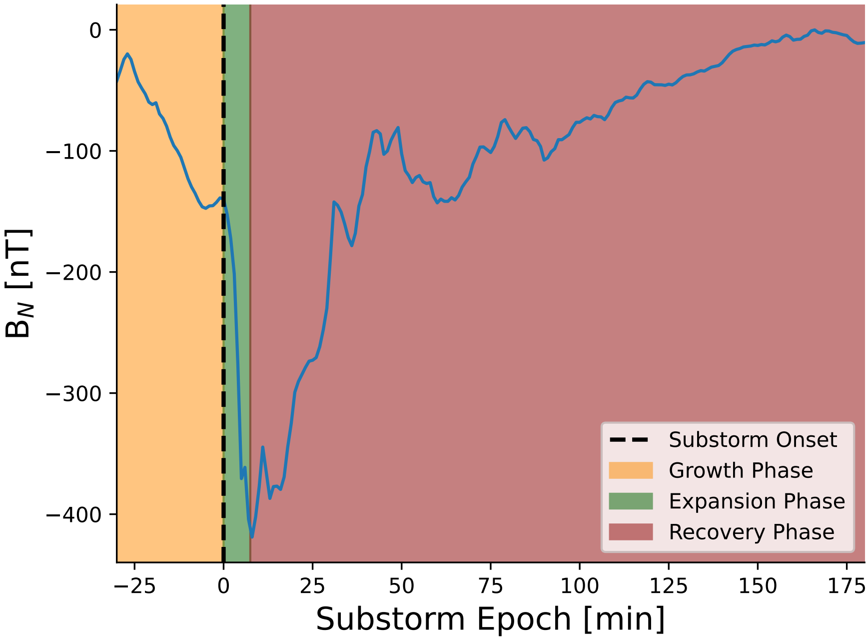

Figure 2.6: Phases of a substorm detected by Forsyth et al. (2015) at 07:51 on the 1st of June 2011 at the location of the magnetometer at Fort McMurray. The northward component of the magnetic field in geographic co-ordinates is shown by a blue line.

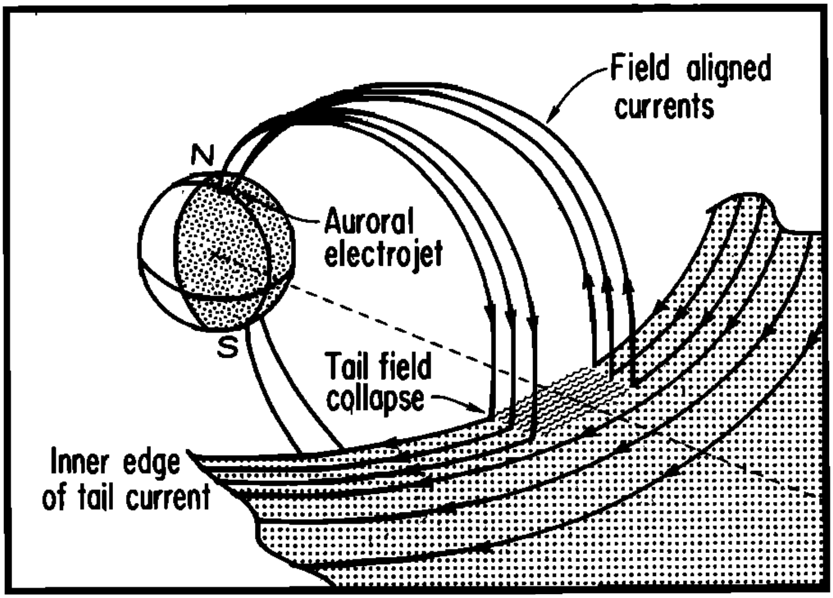

Figure 2.7: Schematic of the substorm current wedge (SCW) taken from McPherron et al. (1973)

2.3.2 Substorm Current Wedge

The expansion phase of the substorm marks a period of dipolarisation of magnetotail flux which stimulate field aligned plasma flows into the aurora zone. The dipolarisation front affects the cross tail current and causes it to short circuit along field lines that map close to the substorm onset location (*Clauer and McPherron*, 1974; *Kepko et al.*, 2015). Figure 2.7 shows that the cross tail current flowing westward diverts along field lines into the ionosphere where it flows westward and then flows out of the ionosphere along field lines returning to the cross tail current. This current system is known as the substorm current wedge (SCW) and it weakens and disappears during the recovery phase.

Figure 2.3 shows the ionospheric part of the SCW, demonstrating how the SCW adds to the electrojet in this region. However, the exact nature of this we return to in the next chapter where the definition of the electrojet is stated more precisely. In the next chapter we also discuss how the ionospheric current systems can be measured through the magnetic field and why the SCW cannot be measured directly using only magnetometers below the ionospheric current layer.

The difficulties in measuring the ionospheric leg of the SCW have prompted the development of new theories regarding its structure and formation. *Gjerloev and Hoffman* (2014) suggested a double wedge structure closing in the ionosphere at two different latitudes and with field lines mapping into different regions of the magnetotail. Another theory is that the SCW is an ensemble of smaller scale "wedgelets" (*Liu et al.*, 2013). During the expansion phase of a substorm the magnetotail can dipolarise through localised dipolarisation flux bundles each triggering small SCWs that are referred to as "wedgelets" (*Juusola et al.*, 2011; *Merkin et al.*, 2019). The sum of these wedgelets can show the same signatures as the double wedge or single wedge if the current cannot be resolved at small enough scales to discern between the neighbouring upward and downward FACs (*Liu et al.*, 2015).

Chapter 3

Understanding the Polar Ionospheric Currents

The most common means of estimating the polar ionospheric current is through their magnetic field signature. However, this is not without its challenges. Understanding the nature of these measurements is important when inferring the behaviour and structure of the polar ionospheric currents. Moreover, the description of ionospheric currents varies depending on the approach: some are simplified for ease of understanding, others are based on assumptions about physics, and some depend on the type of available measurements. In this chapter we discuss and describe strategies for interpreting the ionospheric currents from magnetic field measurements and common ways the ionospheric currents are decomposed.

3.1 Ionospheric Ohm's Law

The ionospheric Ohms law originates from the two-fluid momentum equation, assuming that inertia, gravity, and plasma pressure gradients are neglected. With these assumptions the electric current density can be related to the electric field in the reference frame of the neutral atmosphere, via conductivity. This gives rise to a decomposition of the current into components parallel and perpendicular to the electric field, the Pedersen and Hall currents respectively (*Boström*, 1970; *Vasyliunas*, 2012). Under the assumption of radial magnetic field lines, which is a close approximation in the auroral zone, and zero electric field parallel to the magnetic field, the ionospheric Ohm's law can be height integrated:

$$\mathbf{J} = \Sigma_P \mathbf{E}'_\perp + \frac{\Sigma_H \mathbf{B} \times \mathbf{E}'}{B} \tag{3.1}$$

where $\mathbf{J}$ is the height integrated ionospheric current density, Σ_P is the Pedersen conductance, Σ_H is the Hall conductance, $\mathbf{B}$ is the Earth's main magnetic field and $\mathbf{E}'$ is the electric field in the frame of the neutral wind. The height integration becomes useful at the altitudes of the conductivity peaks (as shown in Figure 2.1 and discussed in section 2.1) as we can treat the horizontal ionospheric current as a sheet and the field aligned currents as closing perfectly within the sheet. As we discuss further in the remainder of the thesis, the three dimensional structure of the ionosphere (i.e. its variation over height) is not possible to resolve when magnetic field measurements originate above or below the current layer. Thus the currents must be treated as a current sheet. In this description the horizontal current is the sum of the Hall and Pedersen current, $\Sigma_H \frac{\mathbf{B}\times\mathbf{E}'}{B}$ and $\Sigma_P \mathbf{E}'_\perp$, respectively.

Solar quiet (Sq) currents make up a part of the Hall and Pedersen currents. They are a result of solar irradiance driven neutral winds that have a local time dependence and flow anti-sunward (*Chapman and Bartels*, 1962; *Pedatella et al.*, 2011). They arise through the electric field in the neutral frame:

$$\mathbf{E}' = \mathbf{E} + \mathbf{u} \times \mathbf{B} \tag{3.2}$$

where $\mathbf{u}$ is the velocity of the neutral wind. The Sq currents have a seasonal and solar cycle dependence and thus vary on much longer time scales than the solar wind coupling driven component of the Hall and Pedersen currents, which vary greatly depending on geomagnetic activity and thus on time scales of substorms. Consequently, the Sq currents constitute a background onto which solar wind coupling driven component of the Hall and Pedersen currents are superimposed. We return to the removal of this background to more accurately investigate the geomagnetic activity related components of the Hall and Pedersen currents in Chapter 4.

Figure 2.3 shows the polar ionospheric currents described as Hall and Pedersen currents. The Hall current flows anti-sunward on the dawn and dusk flanks and sunward across the polar cap. In Figure 2.3 the Pedersen currents are depicted as closing the Region 1 FACs across the polar cap dawn to dusk and closing the Region 1 and 2 FACs on the dawn and dusk flanks in the opposite direction. Although this is a common description, it is only the case when the Pedersen currents are curl-free, which we discuss further in the next section. Furthermore, Figure 2.3 describes the electrojets as Hall currents, which also is a common approximation, but is only true if the Hall currents can be considered to be divergence-free. We explain this further in Section 3.2 and 3.3.

3.2 Helmholtz Decomposition

The horizontal ionospheric current can be subjected to Helmholtz decomposition (*Helmholtz*, 1858) which means that it can be uniquely decomposed into a divergence-free (DF) and a curl-free current (CF) component:

$$\mathbf{J} = \mathbf{J}^{DF} + \mathbf{J}^{CF} \tag{3.3}$$

where $\mathbf{J}^{DF}$ and $\mathbf{J}^{CF}$ are the DF and CF current respectively. The source and sink of the CF current is the FACs into and out of the ionosphere (*Vanhamäki and Juusola*, 2020). Returning to ionospheric Ohm's law and the Hall and Pedersen decomposition of the horizontal current, the Hall current is typically dominated by the DF current and the Pedersen by the CF current. When the conductance gradients parallel to the convection (i.e perpendicular to the electric field) are zero and the magnetic field can be treated as radial (which is a reasonable approximation at high latitudes) the Hall current can be considered DF and the Pedersen current can be considered CF (*Laundal et al.*, 2015, 2018). We return to this in more detail in the next section.

3.3 The electrojet, equivalent current, and Fukushima's theorem

The equivalent ionospheric current is another concept used in the study of ionospheric currents that comes directly from measurements and from the long history of having only ground magnetometers. The equivalent current is a horizontal ionospheric current that is consistent with the magnetic field perturbations we measure on ground. The orientation and relative magnitude of this equivalent ionospheric current is often represented by the magnetometer measurements rotated 90° clockwise (*Gjerloev and Hoffman*, 2014). Due to the vagueness of the term in literature, in this thesis we will describe the equivalent ionospheric current as a horizontal current that is determined from ground magnetometers once other non-ionospheric sources have been removed (discussed further in Section 3.4). Given that historically the auroral electrojets have been measured and understood through ground based magnetometers, the auroral electrojets are an equivalent current. Thus, variations in the ground magnetic field during substorms represent changes in the auroral electrojets. Indices such as the auroral lower (AL) and auroral upper (AU) are based on auroral zone magnetometers and are used to describe how the eastward and westward electrojet, respectively, are changing over time.

It is important to understand the nature of the current systems we measure through observations of the magnetic field. *Fukushima* (1994) and *Boström* (1964) both show that the magnetic field measured on ground does not directly inform us of the full ionospheric current system. Figure 3.1 shows that a current loop is not related to a displacement of the magnetic field below the horizontal component. Thus a current system composed of a radial FAC and a curl-free closure current through the ionosphere cannot be measured through its magnetic field on ground. This is why the existence of Birkeland currents could not be confirmed without satellite borne magnetometers (*Fukushima*, 1994; *Zmuda et al.*, 1966). If we combine this with the knowledge of Helmholtz decomposition (section 3.2) we can conclude that in the polar ionosphere, where magnetic field lines are closest to radial, the equivalent currents, and therefore the auroral electrojet, can be considered to be the divergence-free component of the total horizontal current.

Despite the availability of various space-borne magnetometers that can measure the FACs, ground magnetometers are still more abundant and also located closer to the horizontal current, with areas of high density coverage by networks such as the International Monitor for Auroral Geomagnetic Effects (IMAGE) network. Thus the understanding derived from ground based magnetometers still remains important for a comprehensive view of the ionospheric current system.

To better understand how to interpret the equivalent current derived from measurements below the ionosphere, we return to the ionospheric Ohm's law and the Helmholtz decomposition (equations 3.1 and 3.3). The curl of the horizontal current is the same as the curl of the DF current. The last section showed that ground based magnetometers at high latitudes measure only the DF current. Therefore, the curl of the horizontal current can be found using only ground based magnetometers. Considering only the

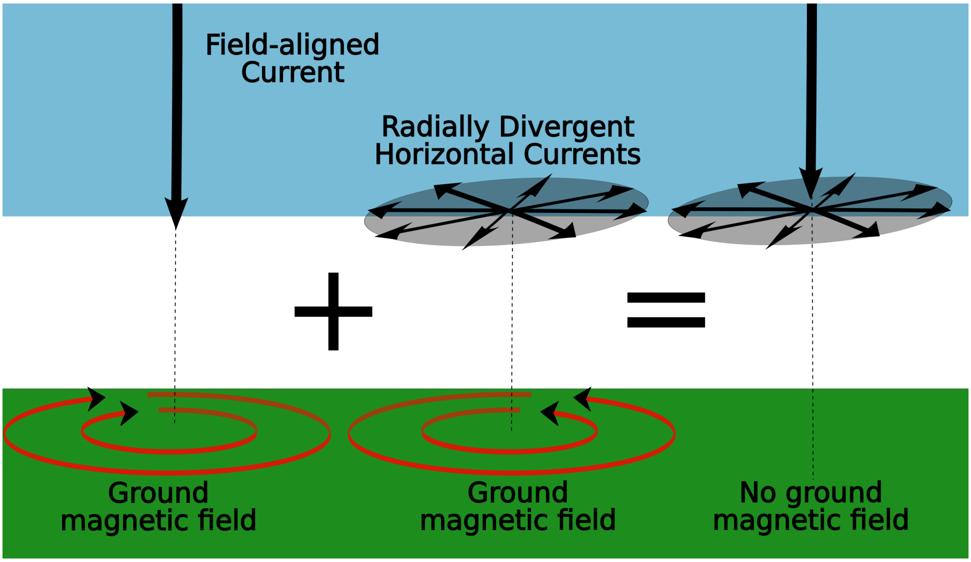

Figure 3.1: Schematic of Fukushima's theorem, demonstrating that CF currents can not be measured by their magnetic field on ground taken from Wikipedia (`https://en.wikipedia.org/wiki/File:Fukushima-cancelation.svg`)

field-aligned, which is assumed radial, component of the curl of the horizontal current:

$$\hat{r}\cdot(\nabla\times\mathbf{J}) = -\nabla\Sigma_H\cdot\mathbf{E}' - \Sigma_H\nabla\cdot\mathbf{E}' - \hat{r}\cdot(\mathbf{E}'\times\nabla\Sigma_P) \tag{3.4}$$

leaves us with a quantity which we call the equivalent FAC (EFAC) (*Amm et al.*, 2002) because of its relation to the field-aligned current, discussed below.

The divergence of the horizontal current:

$$\nabla\cdot\mathbf{J} = -j_r = \nabla\Sigma_P\cdot\mathbf{E}' + \Sigma_P\nabla\cdot\mathbf{E}' - \hat{r}\cdot(\mathbf{E}'\times\nabla\Sigma_H) \tag{3.5}$$

is the FAC. It is also the same as the divergence of the CF current which, as described in the previous section, has no magnetic field signature below the ionospheric current layer and thus requires space based magnetometers.

Using the notation in equation 3.4 and 3.5 one can recognise similarities. If we make the assumption that the last term in equation 3.4 and 3.5 is zero (i.e. $\hat{r}\cdot(\mathbf{E}'\times\nabla\Sigma_{P,H})=0$) then the FAC can be expressed by the radial component of the curl of the horizontal current divided by the ratio of the Hall to Pedersen conductance ($\alpha = \frac{\Sigma_H}{\Sigma_P}$):

$$j_r = -\nabla\cdot\mathbf{J} = \frac{1}{\alpha}\hat{r}\cdot(\nabla\times\mathbf{J}) \tag{3.6}$$

thus the polarity and structure of the FACs can be determined from the EFAC and thus indirectly from ground magnetometers (*Laundal et al.*, 2022). A number of studies have used this approach to investigate the FACs (*Nishimura et al.*, 2020). *Weygand and Wing* (2016) confirmed the similarity between region 1 and 2 current boundaries determined from the curl of the horizontal current and determined from magnetometers on the DMSP satellites.

The validity of the assumption of zero conductance gradient perpendicular to the electric field is the biggest challenge of using the EFAC to study the FAC. In areas of high energetic particle precipitation, such as the auroral bulge, conductance gradients are high (*Aksnes et al.*, 2002), consequently the polarity and structure of the FAC cannot be determined from the equivalent FAC. However, along auroral structures and during low activity the conductance gradients perpendicular to the electric field are small, therefore under these conditions the EFACs can be used to investigate the FACs (*Marghitu*, 2013). The precise location and time at which these assumptions break down and the degree to which this causes the equivalent FACs to differ from the FACs has not been thoroughly investigated, especially around the time and location of substorms. This is of particular importance for studying the substorm current wedge and the inaccuracies in studying the ionospheric current leg of the substorm current wedge from ground. Novel investigations of these limitations are carried out in Paper III.

3.4 Geomagnetically Induced Currents

There are a number of different currents which affect the magnetic fields we measure that are not based in the ionosphere. Arguably, the most significant in the polar regions are the geomagnetically induced currents (GICs), due to their influence on magnetic field measurements taken on ground, at low Earth orbit, and altitudes in between. GICs are currents induced in the ground due to the varying magnetic field associated with varying ionospheric currents. GICs have such a large effect on the measured magnetic field that during active periods they can contribute up to 40% of the AL index (*Tanskanen et al.*, 2001). This can lead to significantly over estimated ionospheric currents if one does not account for the GICs. If we consider the ground conductivity to peak at a certain depth and the horizontal conductivity distribution to be uniform, the GICs can be considered a mirror of the ionospheric current at the depth of the peak (*Juusola et al.*, 2016). However, in areas with highly structured conductance this assumption does not hold. One big example is the steep conductance gradient between the ground and the sea. Figure 3.2 shows that there is a rapid change from crustal conductivity to the highly conducting sea water and this has significant implications on coastal magnetic field measurements (e.g. Bjørnøya) in particular on the radial component (*Juusola et al.*, 2020). Furthermore, Figure 3.2 shows that there are large variations in the ground conductance depending on depth (*Korja et al.*, 2002). We describe methods to remove the influence of GICs on magnetometers in detail in Section 5.3 as it has significant importance for the research within this thesis.

3.5 Estimating Ionospheric Currents using Data Assimilation

Combining magnetometer measurements can enable a more full understanding of the ionospheric currents, which we will return to in Chapter 5. It is also possible to combine magnetometer measurements with other measurements to estimate the full ionospheric current. This is can be useful when the magnetometer measurement cannot measure the full current. It can also help to deal with spatial gaps in data, or to use magnetometers to

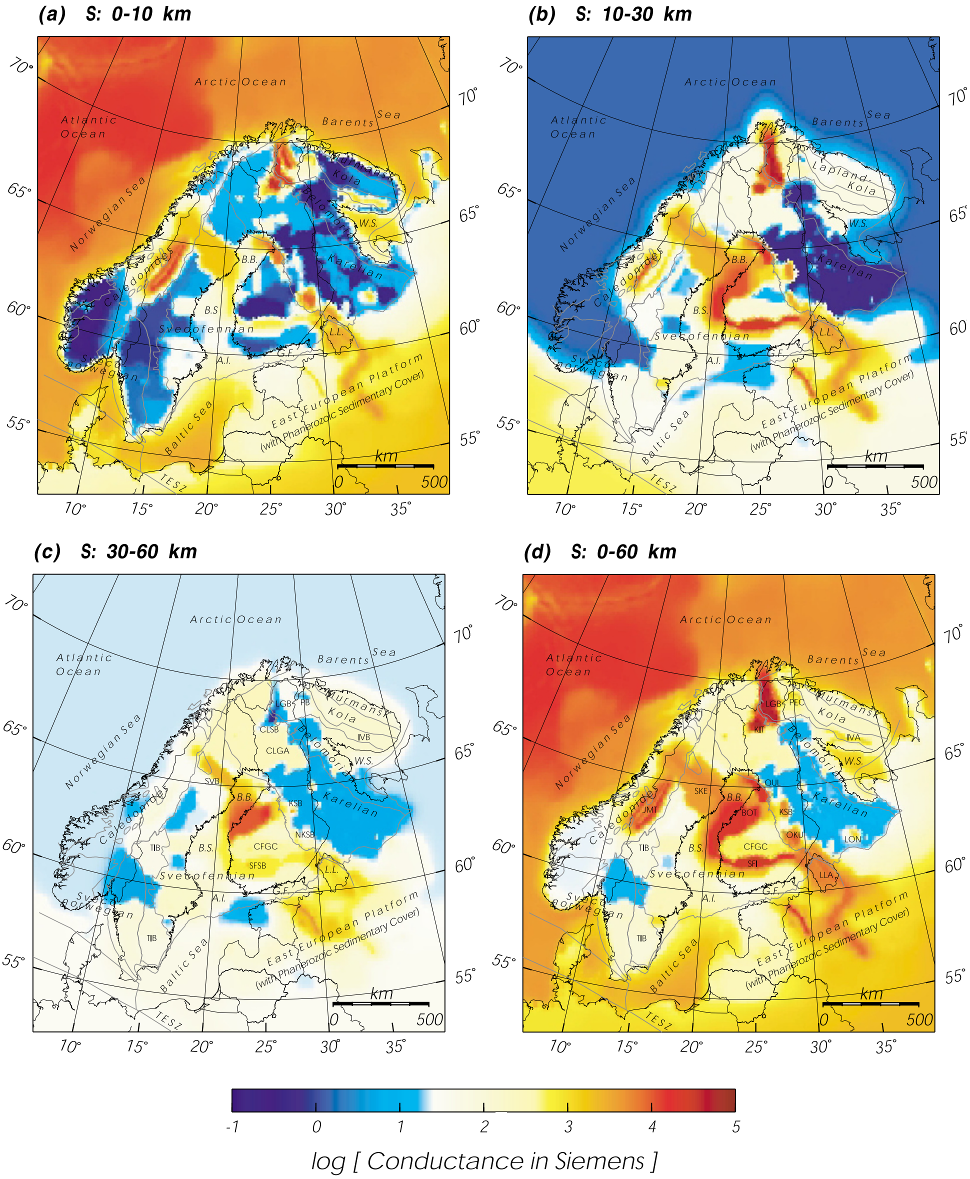

Figure 3.2: Conductance at various depths in the region of Fennoscandia taken from Korja et al. (2002) where S is the depth range.

help understand other parts of the ionospheric dynamics such as the plasma convection velocity and the electric field. Data assimilation techniques can be used to accomplish this by relating different measurements, such as measurements of the magnetic field and electric field, through ionospheric Ohm's law (equation 3.1). In this section we describe three different techniques which require knowledge of the ionospheric conductance to relate the measurements through ionospheric Ohm's law.

The Kamide-Richmond-Matsushita (KRM) method uses only ground magnetometer measurements and conductance as input, and outputs the electric field and the total current system via ionospheric Ohm's law (*Kamide et al.*, 1981). The first step is to use spherical harmonics to create a divergence-free horizontal current that fits the ground based magnetic field measurements. Then by taking the curl of ionospheric Ohm's law, they derive a partial differential equation that only depends on the divergence-free current and conductance. The electric field is found by solving this equation. Using this derived electric field and the model of the conductance the field aligned and total horizontal current can be found.

Another technique builds upon the KRM method. The Assimilative Mapping of Ionospheric Electrodynamics (AMIE) project aims to estimate the electric field and a 2D horizontal representation of the ionospheric current and field aligned currents by fitting the available measurements, such as ground and space based magnetic field measurements. In areas of few measurements, statistical expectations also contribute to the fit (*Knipp et al.*, 1994; *Richmond*, 1992; *Richmond and Kamide*, 1988; *Richmond et al.*, 1998). AMIE is a two-step procedure: The first step is to estimate the Hall and Pedersen conductance using relevant measurements and statistics. The second step is to relate magnetic field measurements, electric field measurements, and other relevant measurements and statistical models through the ionospheric Ohm's law to map the electrodynamics.

In the first step the Hall and Pedersen conductance are found through a spherical cap harmonic fit of statistical models. The second step involves a spherical cap harmonic fit of the electric potential where coefficients are found through a least squares fit to the weighted measurements, where indirect measurements of the electric field such as the magnetic field are related through the conductance found in step one. The model then can be evaluated at any latitude and local time. The horizontal current is then found using the conductance and electric field, and the field aligned current is found through the divergence of the horizontal current.

Finally, the Local mapping of polar electrodynamics (Lompe) method has a similar approach to AMIE, where the same types of measurements can be used to model the polar electrodynamics by relating them through the ionospheric Ohm's law (*Laundal et al.*, 2022). One distinct difference is the use of Spherical Elementary Current Systems (SECS), which we will return to in Section 5.1, as these are the same basis functions we use in this thesis. The benefit of SECS in this context is that they have a short reach, making them ideal for regional analysis. Also unlike AMIE, Lompe does not by default supplement the measurement with statistical models but rather uses regularisation to encourage physically realistic structures. We return to this in detail in

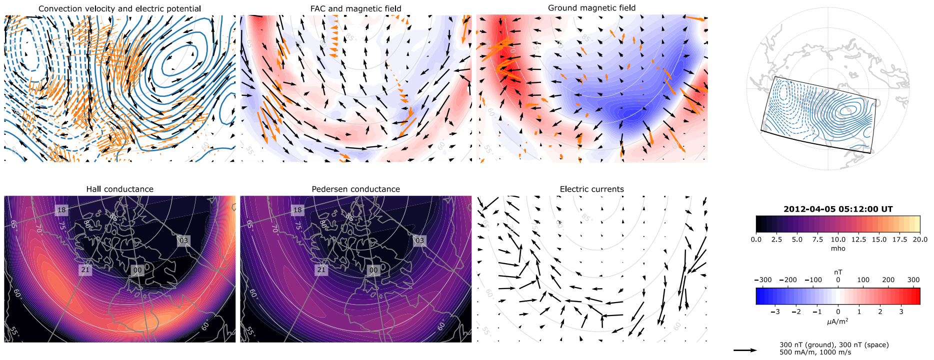

Figure 3.3: Figure showing an example Lompe inversion from Laundal et al. (2022). Orange arrows show the input measurements, black arrows show the estimated component and the Hall and Pedersen conductance is through a model. The top right panel shows the location and extent of the regional analysis.

Section 5.4.

Figure 3.3 shows an example of the application of the Lompe technique. The input measurements are shown in orange. These measurements include line of site convection speed from SuperDARN radars (top left panel of Figure 3.3), space based magnetic field measurements from Iridium (top second from left panel of Figure 3.3) and ground based magnetic field measurements provided by SuperMAG (top second from right panel of Figure 3.3). Lompe relates all measurements to the electric field. For magnetometers this is done through ionospheric Ohm's law, via user-defined conductance which may be based on a model, as is the case in Figure 3.3, or through optical observations of the aurora. Once the electric field is estimated, the magnetic field in space and ground, ionospheric horizontal and field aligned current and convection velocity can be calculated at any location in the analysis grid.

The measurement error can be provided to the Lompe inversion to weight the importance of the data in the inversion. Furthermore, the weights can also be manipulated to intentionally increase the impact of particular types of measurement. One example is when focusing on convection velocities across the OCB. Ground magnetometer measurements have an almost insignificant measurement error compared to SuperDARN measurements, but are a much more indirect measurement of the convection, and therefore rely on an accurate conductance model. Therefore, one can increase the weighting of the SuperDARN measurements so Lompe prioritises the fit of these measurements, despite the measurement uncertainty, while still taking advantage of the ground magnetometer measurements to help produce realistic convection velocities in areas of little or no radar backscatter. Thus this flexibility in Lompe allows us to focus on different aspects of the polar ionospheric electrodynamics and produce more reliable estimates of those quantities.

The regional approach, which we also use in this study, allows Lompe to focus on regions of high measurement density to resolve smaller spatial structures (compared to AMIE and KRM) while retaining the ability for global estimates of the polar ionospheric electrodynamics.

The main caveat of all the methods described in this section is the reliance on conductance models/ measurements. Currently there is poor accuracy of conductance models particular when modelling conductance during disturbed periods such as substorms. Measurements of the conductance are also challenging, currently there are no global auroral images to determine the conductance or other measurements that can retrieve global conductance. Despite this common limitation, Lompe has an advantage over the other methods because it can be applied regionally and therefore does not necessarily require global conductance and could then fix its region to the field of view of auroral imagery, for example the SSUSI instrument on some of the DMSP satellites (*Carter et al.*, 2023). As we return to in Chapter 4 and 5, in Paper I we focus only on ground magnetometers and estimate the divergence-free current. In Paper III we use space and ground based magnetometers to estimate the full ionospheric current such that we are not limited by the need for conductance, while still taking advantage of high-density measurement regions by using SECS as in the Lompe method.

Chapter 4

Data

In the following chapter we introduce and describe the magnetic field measurements we use in Papers I and III to estimate the ionospheric currents.

4.1 Ground Magnetometers

Ground magnetometers play an integral role in all the papers that make up this thesis. As explained in Chapter 3, the magnetic field measured on ground can be interpreted as the superposition of the magnetic field from an equivalent horizontal ionospheric current and an equivalent ground current. At high latitudes the equivalent ionospheric current can be considered to be the divergence-free part of the height-integrated horizontal current, and thus ground magnetometer measurements can be used to reconstruct the first term of the Helmholtz decomposition of the actual horizontal current given by Equation 3.3.

4.1.1 SuperMAG Baseline Technique

In Paper I we use a fixed set of twenty ground magnetometers in Fennoscandia, shown as green stars in Figure 4.1, to constrain a grid of spherical elementary current systems, whose grid edges are shown with green lines in Figure 4.1. The magnetometer data was obtained through the SuperMAG collaboration (*Gjerloev*, 2012) which has taken steps to remove the background magnetic field.

There are many methods to remove the background magnetic field. Different magnetometer chains have different approaches, but SuperMAG applies the same methodology across all magnetometers to ensure a certain level of consistency. It is for this reason and due to ease of data access that we obtain the data from SuperMAG rather than directly from the individual providers. For the case of Paper I the magnetometer providers are the International Monitor for Auroral Geomagnetic Effects (IMAGE) network, the Danish Technical University (DTU) and the Institute of Geophysics, Polish Academy of Sciences (IGF PAS).

Gjerloev (2012) describes the method used to calculate the background magnetic field in order to study the polar ionospheric currents. The background is separated into three components: (1) A slowly varying component that consists primarily of the main

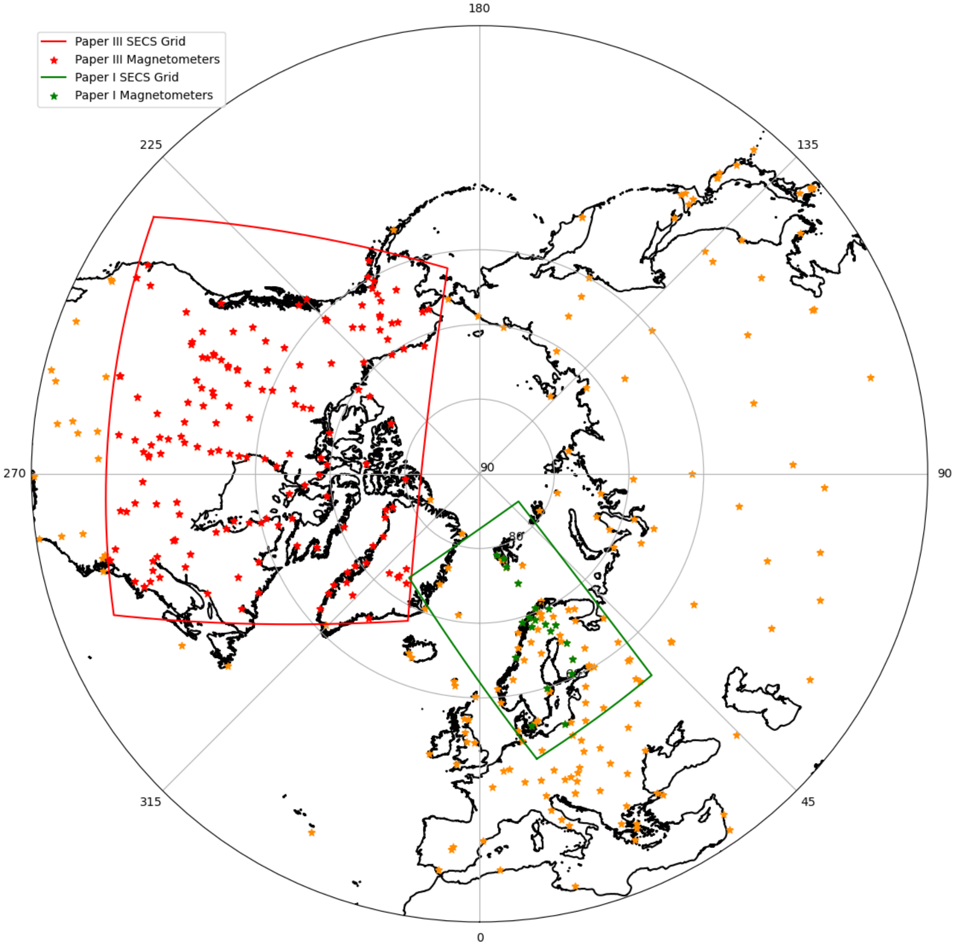

Figure 4.1: Geographic map of magnetometers available through SuperMAG. Orange stars show magnetometers that are not used in the papers of this Thesis. Red lines show the perimeter of the grid of SECS used in Paper III and red stars show magnetometers that satisfy the location requirements of Paper III and are used in the study when data is available. Green lines show the perimeter of the grid of SECS used in Paper I and the green stars show the fixed set of twenty magnetometers used in the study.

magnetic field, (2) a diurnal component consisting of primarily the solar quiet current system and temperature effects on the instruments and (3) a quiet time residual. To calculate the slowly varying component first the daily typical value is calculated using a 17 day or more sliding window (the window is increased until the probability distribution of the magnetic field measurements in the window is desirable, see equation 8 of *Gjerloev* (2012)). The definition of a typical value is explained fully in *Gjerloev* (2012). It is designed to be a representative value for a set of values as an improved metric over the mean or median and is defined either by the mode or the magnitude of a Gaussian fit (criteria for choosing one or the other is explained in *Gjerloev* (2012)). Weighted smoothing is then applied based only on data prior to the point being smoothed and finally, the daily values are resampled to one minute resolution using the cubic convolution interpolation method (*Park and Schowengerdt*, 1983). The result is the slowly varying component (1).

The first step for calculating the diurnal component (2) is to determine daily typical values and resample them to 1 minute resolution using the cubic convolution interpolation method. This is then subtracted from the dataset and diurnal variations are determined from the residual. A window of at least 3 days (the window is increased until the probability distribution is desirable, see equation 8 of *Gjerloev* (2012)) is used to calculate the typical value every 30 minutes from the residual. A weighted fit is then applied to the typical values where the larger the window needed the smaller its weight in the fit. Finally, the 30 minute values are then resampled to one minute resolution using the cubic convolution interpolation method. The result is the diurnal component (2).

The quiet time residual is determined by removing the previous two background components (1) and (2) during official quiet days. The typical value for these days is assumed to be zero and the offset is the quiet time residual (3).

4.1.2 Pre-processing of the SuperMAG Data

SuperMAG provides data in a local magnetic co-ordinate system where the radial component is oriented downwards and is directly determined from the magnetometer, the northward component is oriented as the direction of the magnetic field during quiet periods and the orientation of the eastward component is orthogonal to the northward and radial component. In Paper I we rotate the measurements from the SuperMAG local magnetic co-ordinate system into the geodetic co-ordinate system using the CHAOS magnetic field model (*Finlay et al.*, 2020). We use CHAOS version 7.2 and incorporate both the core and crustal models to calculate the declination angle (i.e. the offset between local magnetic north and geodetic north) at the magnetometer site and thus rotate the horizontal component.

In Paper III we also obtain the magnetometer data from SuperMAG. The selection of magnetometers is variable depending on those available at the time of the inversion and is restricted to be within a spatial window that extends two grid points outside the grid of SECS indicated by the red line in Figure 4.1. Magnetometers within the spatial window are shown as red stars. By the time we started to work on Paper III, SuperMAG began to also provide the measurements in the geodetic co-ordinate system, rotated from their local co-ordinate system using the declination angle derived with the

International Geomagnetic Reference Field (IGRF) (*Alken et al.*, 2021).

4.2 Iridium Magnetometers

In Paper III we investigate the full ionospheric current. To do this we also need space-based magnetometers to measure the CF current. The Iridium satellite constellation consists of over 70 satellites, orbiting at approximately 780 km altitude and have magnetometers onboard for attitude control as part of their operation. Magnetic field measurements are made with a resolution of 48 nT and 11 times per second but are reduced to one per 19.44 seconds in the standard mode when sent to ground, however there is a burst mode that is one per 2.16 seconds that is used infrequently (*Anderson et al.*, 2000). In 1999 JHU/APL received access to this data for scientific purposes and *Anderson et al.* (2000) showed how they can be used to estimate the FACs. This and further studies developed into the Active Magnetosphere and Planetary Electrodynamics Response Experiment (AMPERE) project which provides FACs in both hemispheres based on a spherical cap harmonic fit of the Iridium magnetic field measurements within a ten minute window at 2 minute intervals. A key advantage of Iridium is the sheer number and density of satellites, and therefore magnetic field measurements. Despite the magnetometers not being of the same quality and accuracy as those on board scientific mission satellites the number of measurements allows the signal of the large scale currents to be clear.

We only use the AMPERE FACs as a basis for comparison and as a form of validation in Paper III. The AMPERE project also provides the Iridium magnetic field measurements that we use in Paper III to derive the FACs and the CF current. These magnetic field measurements have been pre-processed by AMPERE following the methodology in *Anderson et al.* (2000). The first step of this methodology is to rotate the IGRF magnetic field model into the spacecraft frame (i.e. along track, cross track etc) and subtract it from the measurements. Secondly, a correction matrix is derived through the correlation of measurements with the main field. Finally, long-term trends are removed using a Fourier transform of the data and zeroing coefficients with periods longer than 26 minutes. After this pre-processing *Anderson et al.* (2000) used 3.5 times the median of the distribution of the absolute values as a threshold for insignificant magnetic field measurements. Values below this threshold, which was typically in the range of 70 to 100 nT, were considered noise. AMPERE provide the measurements in the Earth Centred Inertial (ECI) co-ordinate system so we use tools made available by astropy (*Collaboration et al.*, 2022) to convert the measurements from ECI into the geographic system.

The spatial distribution is also challenging. Figure 4.2 shows the passes and measurements of Iridium satellites, using different colours, during the window needed to create the estimated currents seen in the left column of Figure 4 in Paper III. We can see that the 10 minute window used by both Paper III and the AMPERE project is necessary for good satellite coverage. There is still large spacing between the orbits so a larger SECS grid with greater node spacing compared to Paper I was needed to capture enough Iridium measurements for reliable estimates of the curl-free currents. The orbital spacing also demonstrates why we must focus on the large scales FACs

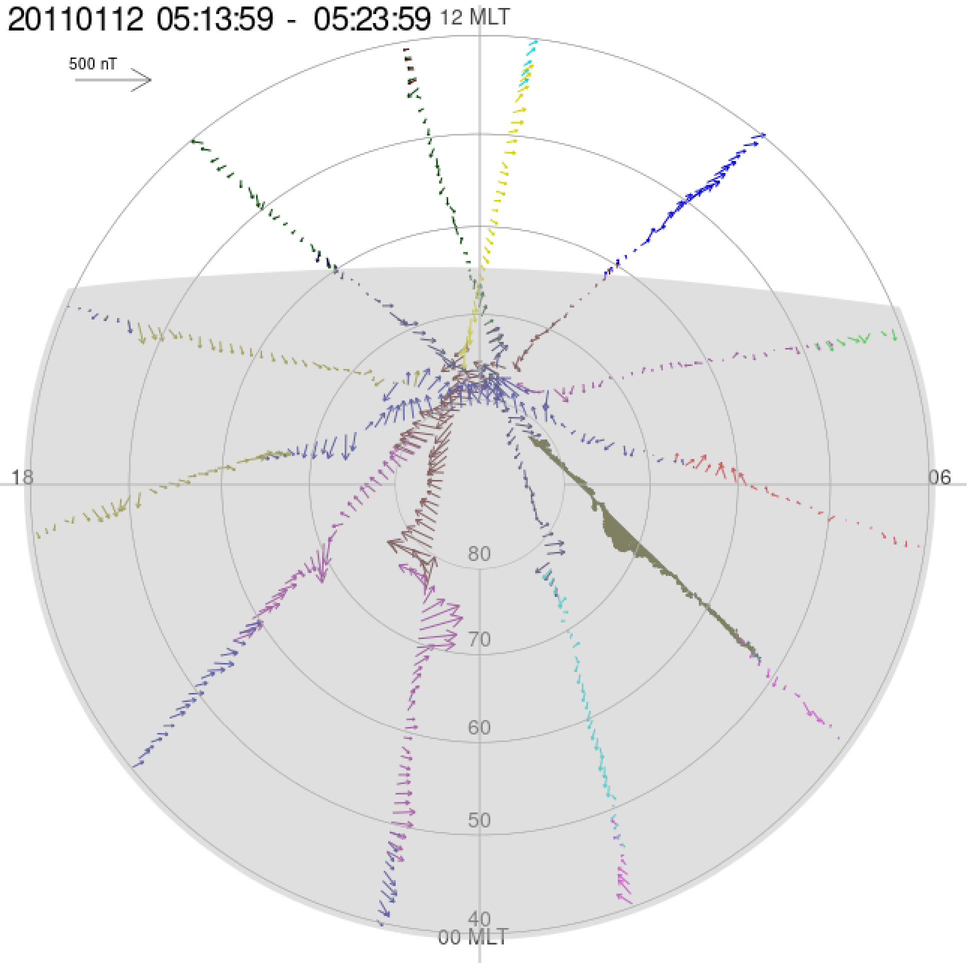

Figure 4.2: Map of the Northern Hemisphere showing the path of the Iridium satellites and their magnetic field measurements within a ten minute window centred at 05:19 UT, on the 12th of January 2011. This is the same window as is used to estimate currents in the left column of Figure 4 of Paper III. Figure taken from Ampere site (`https://ampere.jhuapl.edu/products/`).

when using only Iridium magnetic field measurements. Furthermore, we elected to place the grid of SECS over North America to reduce the gaps in the distribution of ground magnetometers. (Much of this larger grid would be over the ocean if centred in Fennoscandia.)

Chapter 5

Methodology

The development of inversion techniques that combine magnetic field measurements to robustly estimate the divergence-free and curl-free ionospheric currents is integral to the papers and the work that makes up this thesis. In this chapter we describe and discuss the basis functions used, inversion techniques used and how we limit the influence of GICs on our estimations of the ionospheric current.

5.1 Spherical Elementary Current Systems

The SECS basis functions were initially designed to describe the ionospheric current system, utilising Helmholtz decomposition, representing it as a superposition of appropriately scaled DF SECS and/or CF SECS on a 2D shell. The SECS technique was first introduced by *Amm* (1997) and further elaborated on by *Vanhamäki and Juusola* (2020). The elementary functions are expressed as:

$$\mathbf{J}^{DF}(\mathbf{r}) = \sum_i \frac{I_i^{DF}\hat{\mathbf{e}}_{\phi_i}}{4\pi R}\cot\left(\frac{\theta_i}{2}\right), \tag{5.1}$$

$$\mathbf{J}^{CF}(\mathbf{r}) = \sum_i \frac{I_i^{CF}\hat{\mathbf{e}}_{\theta_i}}{4\pi R}\cot\left(\frac{\theta_i}{2}\right). \tag{5.2}$$

where $\mathbf{J}^{DF}$ is the DF current at location $\mathbf{r}$, $\mathbf{J}^{CF}$ is the CF current at location $\mathbf{r}$, I^{DF} and I^{CF} are the amplitudes of the DF and CF SECS, respectively, and θ_i is the angular distance between the location of the i'th SECS pole and $\mathbf{r}$. In the case of Paper I we encounter a problem with singularities when evaluating currents along the meridian, and implemented the modification of J^{DF} within 50 km of a DF SECS as described by Equation 2.44 in *Vanhamäki and Juusola* (2020).

Given that the ionospheric current can be decomposed into DF and CF currents (see Section 3.2), SECS can be used to model these components separately. For cases when the full ionospheric current is desired one can take the sum of the DF and CF currents. The amplitude of each SECS node also contains additional information about the ionospheric current system. The scale of a CF SECS represents its divergence and thus when divided by the SECS grid area provides the FACs in and out of the 2D current shell. On the other hand, the scale of the DF SECS represents its curl and when divided

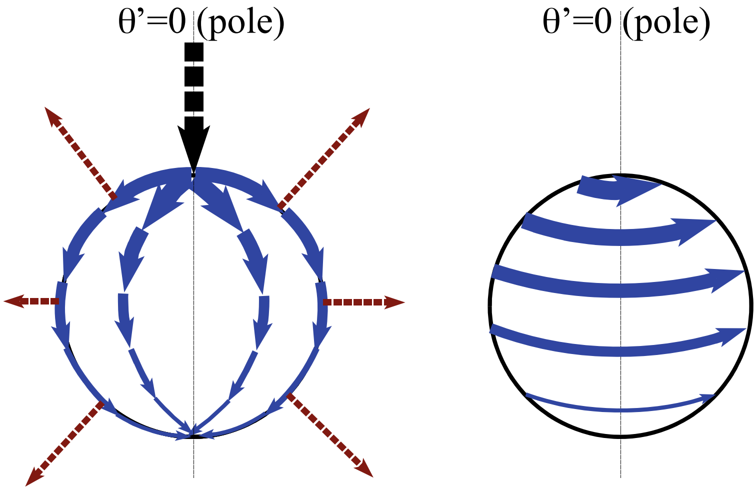

Figure 5.1: Figure showing the current of a curl-free (left panel) and divergence-free (right panel) spherical elementary current system. Figure is taken from Vanhamäki and Juusola (2020).

by the grid area provides the equivalent FACs (see Section 3.3 for a discussion about when the equivalent FAC and FAC are equal).

One advantage of the SECS technique is the linear relationship between the amplitudes of the SECS nodes and their magnetic field as described by *Amm and Viljanen* (1999) and *Vanhamäki and Juusola* (2020):

$$\Delta B^{DF}_{\theta_i}(\theta_i, r) = \frac{-\mu_0 I_i^{DF}}{4\pi r \sin\theta_i} \begin{cases} \frac{s-\cos\theta_i}{\sqrt{1+s^2-2s\cos\theta_i}} + \cos\theta_i & r < R \\ \frac{1-s\cos\theta_i}{\sqrt{1+s^2-2s\cos\theta_i}} - 1 & r > R \end{cases} \tag{5.3}$$

$$\Delta B^{DF}_{\phi_i}(\theta_i, r) = 0 \tag{5.4}$$

$$\Delta B^{DF}_{r}(\theta_i, r) = \frac{\mu_0 I_i^{DF}}{4\pi r} \begin{cases} \frac{1}{\sqrt{1+s^2-2s\cos\theta_i}} - 1 & r < R \\ \frac{s}{\sqrt{1+s^2-2s\cos\theta_i}} - s & r > R \end{cases} \tag{5.5}$$

$$s = \min(r, R)/\max(r, R). \tag{5.6}$$

$$\Delta B^{CF}_{\phi}(\theta_i, r) = \frac{-\mu_0 I_i^{CF}}{4\pi r} \begin{cases} 0 & r < R \\ \cot(\frac{\theta_i}{2}) & r > R \end{cases} \tag{5.7}$$

where R is the radial distance from the centre of the Earth to the current shell and r is the radius at which the magnetic field is evaluated.

5.2 SECS Grid

Where we place the SECS nodes has a large impact on the currents we can estimate. The density of the grid of nodes sets a lower limit of the spatial scales of the currents we

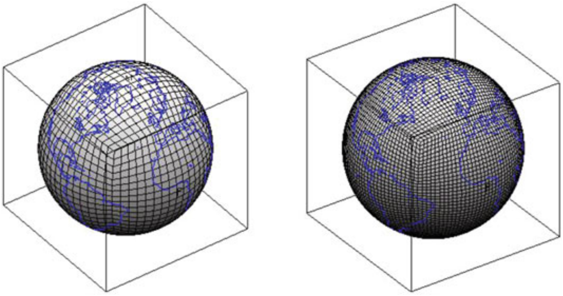

Figure 5.2: Two examples of mapping the cube surfaces to the globe for a low (left) and high (right) density grid. Figure has been taken from Croisille (2013).

can resolve with the SECS representation. One common choice is to place the SECS on a grid of constant longitude and latitude spacing (*Vanhamäki and Juusola*, 2020). However, this leads increasing SECS density at higher latitudes. A consequence is a latitude dependence in the resolvable current structure that may not be justified by measurements or the physical nature of the currents.

In this thesis we use the cubed sphere projection to create our grid of SECS. Introduced by *Sadourny* (1972), developed by *Ronchi et al.* (1996) and implemented for the use with SECS by *Laundal et al.* (2021), the cubed sphere projection places the Earth at the centre of a cube (as shown in Figure 5.2) where locations can be mapped to a cube face from the Earth and vice versa. In the global application the centre of one cube face is aligned with the geographic pole. However, for the regional application in this thesis we place the centre of one cube face in the centre of our analysis region and its orientation can be specified as desired. An equally spaced grid on a cube face relates to a quasi constant grid area on the Earth, unaffected by latitude. While there may be other methods to create a constant grid density in physical space, our opting to use the cubed sphere projection is also motivated by the ability to calculate gradient operators through finite differences. The calculation of gradients is important in Section 5.4 where we discuss how we solve the SECS under-determined inverse problem. The code for working with cubed sphere coordinates and projections has been provided by *Laundal and Reistad* (2022) and its use in SECS has been demonstrated previously by *Laundal et al.* (2021) and *Laundal et al.* (2022).

5.3 Accounting for Geomagnetically Induced Currents

In section 3.4 we introduced GICs and how they can affect the magnetic field measurements. In this section we describe methods that have been used to account for these currents to more accurately estimate ionospheric currents.

One method is to entirely ignore the GICs and assume that the magnetic field measured is purely a result of the ionospheric current. At high altitudes above the ionospheric currents the GICs have less influence, making it more appropriate to ignore their influence. Furthermore, above the ionospheric current layer a separation into ionospheric and GIC contributions is not possible without assuming a relationship between the ionospheric current and the GICs. However, for ground based magnetometers in particular, ignoring the contribution of GICs can cause significantly over estimated ionospheric currents. During disturbed periods a significant portion of the measured magnetic field is due to the GICs (*Juusola et al.*, 2020; *Tanskanen et al.*, 2001). Ground-based magnetometer measurements are more susceptible to small-scale structures in GICs than satellite-based magnetometer measurements purely by virtue of proximity. Ignoring the GICs can alter the entire vector of the estimated ionospheric currents rather than just the magnitude (*Juusola et al.*, 2020).

Another method, which is common among the remaining techniques discussed in this section, is to place a set of DF SECS in the ground as well as the ionosphere. The magnetic field is then said to be the superposition of the magnetic field from appropriately scaled ionospheric and ground SECS. If the ground SECS pole amplitudes are treated as independent variables, the size of the inverse problem increases as more SECS amplitudes must be estimated. This allows the solution to be malleable to complex ground conductivity structure (e.g. Figure 3.2 shows large variations in ground conductance in Fennoscandia).

The image current technique also places DF SECS in the ground to represent the magnetic field of the GICs and treat the magnetic field measurements as a superposition of the magnetic field from the ionospheric and ground SECS (*Juusola et al.*, 2016). In this method the ground conductivity is treated as uniform with a peak at a certain depth, allowing the GICs to be considered as a mirror of the ionospheric current. To define the relationship between the ground and ionospheric SECS the radial magnetic field of the currents is assumed to cancel at a depth, R_c. The scale of the ground SECS then becomes a linear function of the ionospheric SECS (*Juusola et al.*, 2016):

$$I_i^G = -\frac{I_i^I R_I}{R_c} \tag{5.8}$$

where I_i^I is the amplitude of the i'th ionospheric SECS, I_i^G is the amplitude of the i'th ground SECS and R_I is the radial position of the layer of the ionospheric SECS. The radial position of the layer of the ground SECS can be expressed in terms of the cancellation depth and the radial position of the layer of ionospheric SECS:

$$R^G = \frac{R_c^2}{R_I} \tag{5.9}$$

The magnetic field of the GICs can now be calculated from Equations 5.3 to 5.5, with $R = R_G$ and amplitudes expressed as functions of the SECS pole along the same radial axis in the ionosphere.

The advantage of this method is that the problem remains the same size as only one set of SECS amplitudes must be found. However, this methods neglects the complexities of the ground conductivity. As mentioned above, ignoring these complexities not only affects the accuracy of the magnitude of the estimated ionospheric current but also to some extent the direction.

The final method we describe is more physically realistic but also much more computationally arduous, and is not used in this thesis. To start with the ground conductivity must be known, and thus the method is reliant on accurate 3D magnetotelluric surveys, such as the one shown in Figure 3.2. Furthermore, the time history of the magnetic field measurements must be known. This enables a 3D understanding of the GICs as the strength and depth of the GICs is dependent on the frequency of the magnetic field variations (*Grayver et al.*, 2021). In order to realistically perform this approach, a sensible limit for the time history must be chosen that includes the frequencies of magnetic field variations that are responsible for the majority of the GICs.

This first method (completely ignore GICs) is not appropriate as the GICs are known to have a significant influence on the ground magnetometers (*Tanskanen et al.*, 2001). The second method, which treats a set of ground SECS pole amplitudes as independent parameters, can be problematic due to the distribution of measurements. Close to magnetometers this approach may be sensible as shown by *Juusola et al.* (2020), but away from measurements the freedom in this model can create unrealistically complex GICs which in turn create poor estimates of the ionospheric currents. We use the third method (image currents) as a sensible middle ground. The model solution is no more computationally heavy than ignoring the GICs altogether. Treating areas of sea as a mirror current is arguably sensible and the regularisation technique that we explain in the next section helps the inversion ignore signatures of the magnetic field that are due to highly structured currents in the ground. We set the cancellation depth (R_c) at 500 km. The fourth method is most physical but is computationally heavy due to the need of time history and is reliant on accurate magnetotelluric surveys.

5.4 Solving the Inverse Problem

In Paper I and III we describe the relationship between magnetic field measurements and SECS amplitudes through linear relationship:

$$G\mathbf{m} = \mathbf{d}, \tag{5.10}$$

where G is the matrix relating the measurement location to the magnetic field produced by the SECS through Equations 5.3–5.7, **m** is a vector containing the SECS amplitudes and **d** is a vector containing the magnetic field measurements. In both Paper I and III this linear relationship represents an under-determined inverse problem as we have a far greater number of SECS nodes than measurements. We tackle this in very similar ways in both Paper I and III by guiding the solution with prior expectations of the current structure. In Paper I we are tasked with only estimating the DF current and follow on from similar previous studies (*Laundal et al.*, 2021) and use Tikhonov regularisation. The implementation of regularisation is best illustrated via a cost function. Starting with the standard least squares approach to the solution of an inverse problem, the cost function f is:

$$f = ||G\mathbf{m} - \mathbf{d}||^2 \tag{5.11}$$

where the solution **m** can be found by minimising f, the squared difference between the model and the data.

With Tikhonov regularisation we apply extra components to the cost function that are based on our understanding and expectation of the DF ionospheric currents. Firstly, we minimise the complexity of the model solution, as ground based magnetometers are 110 km from the ionospheric currents, and the distance between magnetometers is even greater, so we cannot resolve structures of smaller scales. Secondly, the electrojets are typically aligned in the magnetic east-west direction with smooth gradients so we add a term to the cost function to penalise solutions with large gradients of the DF currents in the magnetic east-west direction. The cost function is thus:

$$f = ||G\mathbf{m} - \mathbf{d}||^2 + \lambda_1 ||I\mathbf{m}||^2 + \lambda_2 ||L_e\mathbf{m}||^2, \tag{5.12}$$

where I is an $N \times N$ identity matrix (N is the number of SECS) and L_e is an $N \times N$ matrix that, when multiplied with $\mathbf{m}$ produces the directional derivative in the magnetic east direction of the components in $\mathbf{m}$ (the SECS amplitudes). L_e is calculated using finite differences (*Laundal et al.*, 2021). The first term remains the squared model difference, the second term is the squared length of the model vector and the last term is the sum of the squared magnitudes of the magnetic eastward gradients of the SECS amplitudes. The regularisation parameters λ_1 and λ_2 are used to scale the importance of the different terms in f. A careful balance must be found to encourage the expected behaviour while ensuring that the total regularisation is not more important than the difference between the model and data. A correct choice of regularisation parameters will produce currents close to the expected structure when the data supports it while also being able to disagree with the expected structure when an alternative structure is indicated by the data. In Paper I we test a number of events in order to choose appropriate values for λ_1 and λ_2 paying particular attention to events that disagree with the expected current structure such as northward orientated DF current that is clearly indicated by the magnetic field measurements.

In Paper III we also make use of Tikhonov regularisation in the application of DF and CF SECS with one modification, the first regularisation term is replaced with a forward difference matrix in both the directions in the cubed sphere grid. This adaptation gave the solution the freedom for larger model amplitudes within coherent structures. Paper III is focused on estimating the full ionospheric current during substorms and comparing the FACs with the equivalent FACs. The regularisation approach allowed for the encouragement of the electrojet structures in the DF currents and region 1 and 2 current systems in the CF currents. Furthermore, we are able to focus on currents of the scale of the substorm current wedge and the use of a consistent regularisation approach for both DF and CF SECS, with the same scale of importance, allowed for a coherent full ionospheric current to be estimated and for a substantiated comparison of the FACs and equivalent FACs.

Chapter 6

Summary and Discussion of Papers

In this chapter we summarise the three papers that constitute the research of this thesis. Each paper has a focus on the development of inversion techniques and datasets to unravel the nature of the polar ionospheric currents through measurements of the magnetic field. The overarching objective is the development of robust inversion techniques for estimating the divergence-free and curl-free ionospheric currents, using them to explore the limits of what can be understood of the entire polar ionospheric current system and the auroral oval from ground-based magnetometers. We eventually discuss the uncertainties related to the data and techniques used in this thesis.

6.1 Summary of papers

Paper I: Statistical Temporal Variations in the Auroral Electrojet Estimated With Ground Magnetometers in Fennoscandia

S.J. Walker, K.M. Laundal, J.P. Reistad, A. Ohma, S.M. Hatch (2023), Space Weather, volume: 21

Paper I focuses on estimating the DF current using SECS and twenty ground magnetometers in Fennoscandia. Consistency in the model inversion is key in Paper I for ensuring temporal comparability. We choose a fixed set of ground magnetometers and do not estimate the DF current if any are missing. As a consequence there can be large data gaps but we are able to make estimates spanning from 2000 to 2020 due to the longevity of the operation of the chosen magnetometers. The fixed set of magnetometers coupled with a geographically fixed grid of DF elementary systems ensures constant model geometry. Without such restrictions, changes in the estimated parameters could be attributable to changes in magnetometer distribution and model geometry rather than being solely attributable to changes in the ionospheric current system.

We also highlight the importance of the placement of the elementary systems. We follow the example of *Laundal et al.* (2022) and use a cubedsphere grid that has nearly constant spacing in distance. Prior studies have often placed elementary systems with constant latitude and longitude spacing, however, this creates a problem of increasing grid density at higher latitudes (*Vanhamäki and Juusola*, 2020). Another reason we use a cubedsphere grid is related to how we solve the inverse problem. Section 5.4 demonstrates that SECS manifests as an under-determined linear inverse problem between the scales of each system and the magnetic field measurements. How we solve this inverse problem will shape the currents we estimate and as such it is vital that we impart prior knowledge of the structure of the ionospheric currents to encourage realistic solutions. The cubedsphere grid allows us to easily calculate the gradient of the scales of the elementary systems and, just like the implementation in *Laundal et al.* (2022), we utilise this to impart the expectation of magnetically east-west aligned structures. This is achieved by penalising solutions that have large gradients in the magnetic east-west direction. Additionally, we penalise solutions with a large euclidean norm of the elementary system scales vector to encourage smaller model complexity.

Using this SECS inversion scheme we evaluate the DF current and radial magnetic field along the 105° magnetic meridian for every minute the twenty magnetometers are available concurrently. This meridian is chosen as it passes through the region of highest magnetometer density, ensuring high confidence in the estimated parameters. The first result of Paper I is the dataset of 1-minute resolution DF currents and ground magnetic field along the magnetic meridian spanning 2000-2020 and totalling approximately eleven years, due to data gaps in the magnetometers. We then validate the dataset by comparing average maps of the DF currents and radial magnetic field with those produced by the Average Magnetic Field and Polar current Systems (AMPS) empirical model (*Laundal and Toresen*, 2018).

We go on to explore the temporal derivative of the radial magnetic field, a key aspect of this dataset in contrast to empirical models. When focusing on the latitudinal profile, we find two clear peaks in the probability of large derivatives. The largest is close to the coast of Norway and the other is in the region of Svalbard. Being coastal there is a distinct possibility that these are related to the sharp conductance gradients that occur between the highly conducting sea and land. Furthermore, the lack of magnetometers between the Norwegian coast and Svalbard could be the cause of a reduced probability of large derivatives in this area, as the regularisation will impart small gradients in the absence of data. However, these are not the only possible hypotheses; the high latitude peak can be created by the high latitude return currents and the second peak by the electrojets. An analysis of a local and latitude distribution of derivatives of a magnitude greater than 25 nT/min shows that the latitude of the peaks is consistent for all local times but their magnitude is local time-dependent. The low latitude peak shows the highest occurrence probability pre-midnight, which is consistent with the occurrence of substorms where large variations in the electrojet are expected. The high latitude peak shows the highest probability pre-midnight and around 9 MLT. The first could again be explained by substorms but the second is not easily explained. We propose two hypotheses: (1) ULF waves have been shown to occur more frequently in this area by *Nosé et al.* (1995). We show in Paper I that ULF waves persist in our dataset and therefore it may be the cause of the large derivatives. (2) *Madelaire et al.* (2022) showed that current vortices are created in this region by rapid solar wind pressure increases and thus these currents could be the cause of the occurrence of large derivatives.

The key components of Paper I are the production and validation of the dataset of DF currents and magnetic field perturbations and the demonstration of how it can be used to improve our understanding of the polar electrojets, with special emphasis on its temporal variation.

Paper II: A comparison of auroral oval proxies with the boundaries of the auroral electrojets

S.J. Walker, K.M. Laundal, J.P. Reistad, A. Ohma, S.M. Hatch, G. Chisham, M. Decotte (in review as of October 2023), Space Weather

The main goal of Paper II is to estimate the boundaries of the auroral electrojet using the dataset produced in Paper I and to understand its limitations as an auroral oval boundary proxy.

Boundaries of the auroral oval have long been sought after as they contain a significant amount of information about the magnetospheric and ionospheric state with descriptive capabilities for the location and strength of space weather hazards. The poleward boundary is particularly important as it can be used to infer the boundary between open and closed magnetic flux and thus allows us to calculate the amount of open flux in the polar cap. The expanding contracting polar cap paradigm explains in detail how changes in the open closed boundary (OCB) can tell us about the loading and unloading of magnetic flux in the magnetotail (see Section 2.2.3) (*Cowley and Lockwood*, 1992; *Lockwood and Cowley*, 1992; *Milan*, 2013).

The boundaries of the auroral oval have commonly been measured using auroral imagery or by directly measuring precipitating auroral energy particles. *Chisham et al.* (2022) found boundaries of the auroral oval from global satellite imagery and *Kilcommons et al.* (2017) and *Decotte et al.* (2023) demonstrate how to detect the auroral oval from DMSP particle precipitation measurements. The challenges of these two approaches are global coverage and longevity. Satellite global auroral imagery has not existed anywhere near as long as ground magnetometers and there are significant gaps due to a lack of overlapping missions and due to satellite orbits. Additionally, observational challenges such as dayglow can render the task of estimating global boundaries from imaging impossible. The DMSP satellites have existed since the 1960s but they do not have global coverage or continual auroral observations and their sun-synchronous orbits provide poor coverage of some local times. These difficulties motivate an investigation of an auroral oval proxy from the dataset produced in Paper I. The dataset in Paper I is restricted to a magnetic meridian and thus a global auroral oval proxy cannot be inferred from the dataset. However, if a comparison with other auroral oval proxies indicates that an auroral oval proxy based on the electrojets is feasible, in the future a global estimation of the electrojet could be produced. Furthermore, the temporal coverage of ground-based magnetometers can reveal patterns and trends that are not so clear in other datasets and allow for robust statistics.

We analyse the eastward component of the DF current found in Paper I. We identify boundaries of eastward and westward sections of the current for each minute of data using a set of gradient and absolute value criteria. This allows us to produce a new dataset containing the boundaries, the total current and the peak value of up to three eastward and three westward current sections. We then define the electrojet as the current section with the greatest absolute total current. These electrojet boundaries are compared with the electron precipitation auroral oval, as detected by DMSP and by the SI13 imager on the IMAGE satellite, and with the proton precipitation auroral oval, as detected by DMSP and by the SI12 imager on the IMAGE satellite. We produce average local and latitude maps of the different boundary datasets and analyse two events where a DMSP satellite is in close proximity to the magnetic meridian. On average the proton auroral oval is a closer match to the electrojet boundaries than the electron auroral oval. One event agrees with this statement and the other is only a match for the equatorward boundaries, demonstrating that the average maps do not tell the whole story. Furthermore, with increasing proximity to the discontinuities of the electrojets (pre-midnight and pre-midday) we find the boundary distribution becomes more bimodal. Therefore, the electrojet boundaries in these regions are not easily defined. Hence, subsequent inferences about the auroral oval from the electrojet in these regions should be be done with great care.

This study not only identifies challenges with determining the extent of the auroral oval from the boundaries of the electrojet but also demonstrates the value of creating this boundary dataset. We also find that the auroral oval varies depending on the chosen dataset, most clearly in the comparison between the electron and proton auroral oval. This variation can affect the description of the polar ionospheric dynamics. In particular, for this study we find the electrojet can often exist outside the limits of the electron auroral oval but on average remains inside or close to the proton auroral oval. This finding contradicts the description found in previous work where the auroral oval is determined from electron precipitation and the electrojet is simply assumed to exist inside the auroral oval (*Feldstein and Starkov*, 1967; *Johnsen*, 2013; *Newell et al.*, 1996). Finally, Paper II highlights the importance of understanding the location of the electrojet and provides a more detailed description of the electrojet in comparison to the auroral magnetic indices. With and without global auroral imagery the electrojet boundaries can inform us of the strength and location of space weather hazards and are a valuable tool for understanding the polar ionospheric dynamics.

Paper III: The Ionospheric Leg of the Substorm Current Wedge: Combining Iridium and Ground Magnetometers

S.J. Walker, K.M. Laundal, J.P. Reistad, S.M. Hatch, A. Ohma, J. Gjerloev (In review as of January 2024), JGR Space Physics

Paper III aims to resolve the full ionospheric current through the sum of the DF current, CF current and FAC to study the ionospheric portion of the substorm current wedge and explore the limitations of understanding the full ionospheric current from ground-based magnetometers.

Just like in Paper I we use ground magnetometers to constrain a cubedsphere grid of DF SECS. We also place CF SECS on the same cubedsphere grid and constrain them using magnetic field measurements from the Iridium satellites. We calculate equivalent FACs (described in section 3.3) by dividing the amplitude of each DF SECS pole by the corresponding grid area, and calculate FACs by dividing the amplitude of the CF SECS by the grid area. We focus on a larger region in North America to capture more Iridium measurements and for the same reason we use a window of ten minutes to capture more data. The ground magnetometer measurements are averaged across this window. We also modify the inversion scheme for Paper III compared to Paper I by replacing the zeroth order Tikhonov term with a forward difference matrix to minimise the difference in the amplitude of neighbouring SECS. Similar spatial scales for the DF and CF currents are important to coherently estimate the full ionospheric current and make justified comparisons between the equivalent FACs and the FACs. Therefore, the inversion and scaling of the regularisation is consistent for the DF and CF SECS. Furthermore, it is kept consistent across time and events to enable comparison of different events.

We compare the FACs produced by the AMPERE project and by our CF SECS approach as a form of validation. Finding that although AMPERE can produce greater spatial variability, there is enough similarity to prove our approach is a valid interpretation of the Iridium magnetometer data. We then create an events list of 18 substorms to study. These are selected because they occurred in three substorm lists: *Forsyth et al.* (2015); *Newell and Gjerloev* (2011); *Ohtani and Gjerloev* (2020) and occurred close to the centre of the grid of SECS during the years 2011 and 2012. We separate these events into typical and atypical depending on the current structure, where typical is a clear current wedge structure by Epoch +20 min from substorm onset. Out of the 18 events 12 are considered typical and 6 atypical.

We pick one typical event to analyse a time series of the full current (DF + CF) and an equivalent full current surrounding the onset. The equivalent full current is found by treating equivalent FACs as the FACs (i.e. setting $\alpha = 1$ in equation 3.6) and interpreting the CF current from this. Thus the equivalent full current is purely determined from ground magnetometers. We do the same for the remaining 17 events but show only substorm Epoch 20. We find that the equivalent FACs become increasingly dissimilar to the FACs closer to the onset location. Temporally they become more dissimilar post onset time. We attribute this increasing dissimilarity to a change in the Hall and Pedersen conductance that leads to the assumption, $\hat{r} \cdot (E \times \nabla\Sigma_{P,H}) = 0$, becoming more invalid. The SML index and enhancement of equivalent FACs show that for all these events there is a strengthening of the westward electrojet despite the lack of SCW in the atypical events.

To investigate how the change in conductance alters the relationship between the equivalent FACs and the FACs we use a combination of Lompe and AMPS (*Laundal and Toresen*, 2018). We supply the AMPS FACs under typical conditions to Lompe and then calculate the equivalent FACs for two different conductance scenarios. The first conductance scenario is purely solar EUV-driven. The second scenario is solar

EUV-driven plus a Gaussian around the substorm onset to mimic the auroral bulge. We find that an enhancement of equivalent FACs and therefore the westward electrojet can occur with no change in the FACs and purely due to the change in conductance. This explains the results we see but raises concerns for studies that interpret the enhancement of the westward electrojet as the creation of the closure current of the SCW.

The key findings of Paper III are that the FACs should not be interpreted from the equivalent FACs, and thus from ground magnetometers, surrounding substorms without measurements of the conductance. Additionally, the enhancement of the westward electrojet can be a false indicator of the formation of the SCW.

6.2 Discussion of Uncertainties

Uncertainties are a big challenge in under-determined inverse problems. In our case there are multiple sources of uncertainty, some of which are hard or even impossible to quantify.

The first source of uncertainty is within the data. Ground magnetometers are considered to have a low measurement error but beyond the uncertainty inherent in the instrument there are several ways the uncertainty enters the measurements prior to the inversion. One example is the uncertainty in the baseline subtraction (described in section 4.1.1). If the main field is over- or under-determined there will be a constant offset in the measurements. Furthermore, while we only describe one method for the removal of a baseline, there are a large number of different techniques that settle on different values (*Janzhura and Troshichev*, 2008; *Van De Kamp*, 2013). Transient external noise such as short-lived magnetic field sources (e.g. passing electrical devices) would not be captured by baseline determination due to variations on similar time scales as those of ionospheric current origin.

The Iridium magnetometers have the same source of uncertainty through baseline determination, and the AMPERE project distributes the data with the baseline, determined through their method, already removed. Iridium magnetometers were not designed for scientific application, and so are not as accurate. They have a resolution of 48 nT and the threshold for noise can vary between 70 and 100 nT (*Anderson et al.*, 2000).

In linear inverse problems the measurement error can be carried through the inversion using the covariance matrix. In techniques such as Lompe, the covariance matrix weights the measurements such that the fitting of more accurate data is prioritised. The covariance matrix can then be carried through to an uncertainty in the model parameters, in this case the amplitude of the SECS, and consequently through to the estimated quantities. In a well-determined problem with a uniform distribution of magnetometers such uncertainties may be an indicator of the accuracy of the model compared to the real currents. However, we do not have this situation and must impose prior information to aid the solution. We achieve this by employing Tikhonov regularisation where the regularisation parameters are chosen through a trade-off between expected structure and data fit. Therefore our inversion does not match the data perfectly. The higher the amount of regularisation (λ_1 and λ_2 in equation 5.12) the greater its importance compared to the data model fit and therefore less of the measurement uncertainty carries through to the model variance. In fact, the model variance decreases with increasing regularisation. Yet increasing regularisation will typically lead to a poorer data-model misfit. At high enough regularisation the model variance approaches zero but the magnetic field measurements no longer have influence over the estimated currents. To know the true accuracy of the estimated parameters one must also know the reality; this would only be possible with, for example, a synthetic MHD model.

Using an MHD model to obtain the model accuracy is unrealistic as the model accuracy will vary depending on the differences between the currents and the expected structure encouraged through regularisation. Moreover, current MHD models are incapable of generating realistic ground-induced currents. Thus true model accuracy is not viable.

In Papers I and III, we outline our steps to reach the chosen regularisation scaling and these steps describe a sensible approach to understanding the model accuracy. They entail achieving a careful balance between data model misfit and the encouragement of expected structure. While this does not provide a numerical model accuracy, one can understand that in high-density measurement regions the model accuracy is high while in less dense regions the model is the product of measurement extrapolation and expected structure and thus must be interpreted with care.

For the estimation of the divergence-free currents in Papers I and III there are uncertainties due to the separation of the contributions of ionospheric currents and GICs on the measurements at ground magnetometers. Placement of the magnetic contributions into the wrong system will lead to incorrect estimations of the ionospheric current.

In Paper I we are strict in our estimation of the divergence-free current and ground magnetic field perturbations by evaluating along a single magnetic meridian which has a high magnetometer density to produce a solution well constrained by data. The spacing of the evaluation points in latitude reflects the limits in the spatial resolution of the model and reduces the effect of current location uncertainty. This plays an important role in Paper II, where the electrojet boundaries are identified along with the total current and other properties. Where in Paper II the resolution of the evaluation points along the meridian limits the freedom of boundary locations preventing unrealistic accuracy of the electrojet boundaries with respect to the magnetometer dataset used. Furthermore, the magnetometer density reduces at the latitudinal limits of the data set produced in Paper I. This implied decrease in model accuracy leads us to ignore boundaries close to these limits in Paper II.

Chapter 7

Conclusions

This thesis has focused on the development of new inversion schemes for combining magnetic field measurements to produce robust estimates of the ionospheric current. A primary goal has been to use the estimated ionospheric current to understand the appropriateness of studying the substorm current wedge from ground magnetometers and the feasibility of a ground-based magnetometer proxy of the auroral oval.

Paper I demonstrates the advantages of an inversion combining magnetic field measurements and the temporal extent of ground magnetometers for the statistical analysis of the temporal derivatives of the magnetic field. The availability of ground-based magnetometer measurements over multiple decades allowed for robust statistical determination of the occurrence of large temporal derivatives in the radial magnetic field, a quantity that identifies hot spots for GICs. Furthermore, the mapping technique allowed us to determine latitudinal variations beyond what can be inferred from individual magnetometers. Additionally, we show that our dataset is a great tool for visualising and investigating magnetospheric waves with periods greater than 1 minute, such as ultra-low frequency waves.

In Paper II we show that the electrojet profiles we estimated in Paper I can provide information about variations in the auroral oval. We derive electrojet boundaries that show similarity with the auroral oval boundaries, in particular the boundaries of the proton aurora. Given that estimates of global auroral boundaries derived from global auroral imagery are relatively scarce, any information about the auroral oval that we can obtain from the electrojet is invaluable. The dataset we create includes, in addition to boundaries, the total current of the electrojet and its peak value. While global electrojet boundaries were not produced in this study, the statistical analysis motivates such a future study, which we return to in chapter 8. Paper II demonstrates that we can produce more detailed metrics on the electrojet on a routine basis in comparison to the auroral magnetic indices (e.g. AL and AU).

In Paper III we developed on the inversion techniques to robustly estimate the total ionospheric current based on space and ground magnetometers. We show that the ionospheric leg of the substorm current wedge can be estimated by taking the sum of independently estimated divergence-free and curl-free currents. We show that FAC structure, polarity and strength cannot be inferred from ground-based magnetometers through the EFAC technique (the curl of the divergence-free current) during substorms and in regions surrounding the onset. We also conclude that intensification of the westward electrojet can occur without the intensification of FACs and therefore without the formation of the substorm current wedge. This is due to changes in the conductance associated with increased energetic particle precipitation. Additionally, we find that despite taking strict measures to ensure the validity of our substorm events (the substorm must be present in three ground-based magnetometer substorm lists) the substorm current wedge was only present in two-thirds of the events. Therefore, substorms identified using ground-based magnetometers do not guarantee the presence of the substorm current wedge. These results are relevant for interpreting the magnetic field measurements from EZIE in terms of the substorm current wedge, which we return to in Chapter 8.

In summary, we have developed a robust methodology to routinely estimate the auroral electrojet, its boundaries, peak intensity, and total current. The dataset of estimated currents and ground magnetic field has been shown to be a valuable asset to study statistical trends in the auroral electrojet and to gauge the hot spots of space weather hazards. The boundaries of the electrojets are shown to hold key information about the location of the auroral oval, demonstrating ground magnetometers can be used in isolation to infer the extent of the auroral oval when more direct proxies are not available. Despite the historical use of magnetic field measurements made below the ionospheric current in the study of the substorm current wedge, and consequently, in the development of theories surrounding its structure, we have also demonstrated that when used in isolation, these measurements can lead to incorrect inferences about the substorm current wedge. In fact, for a significant number of events studied in Paper III, the same ground-based signatures appear with or without the occurrence of the substorm current wedge.

Chapter 8

Future Prospects

A number of components of the work and papers that make up this thesis can be continued, built upon and applied in new ways. In this chapter we introduce some of these future prospects and why they would be beneficial.

8.1 Expanding upon the new methodology developed

Paper I and III focus on the application and development of inversion techniques for estimating the ionospheric currents. The clearly outlined methodology and publicly available code make the work repeatable. As such the approach in Paper I can be applied to other regions of ground magnetometers and this will allow us to discern what features of the statistics are due to geographical effects and which are the result of the ionospheric currents. For example we are unable to determine whether the peaks in the occurrence of large temporal derivatives of the radial magnetic field are a result of the steep ground conductance gradients or variations in the equivalent current. Repeating this study in a new region, such as north America, could help us to understand and separate the different contributions.

Paper II estimated the boundaries of the auroral electrojet which informs us where there is an increase in GIC related space weather hazards. The electrojet boundaries were shown to often be close to the auroral oval, particularly when described by proton precipitation, away from the pre-midday and pre-midnight electrojet discontinuities. This paper motivates the creation of a global electrojet boundary. One potential way to do this would be to repeat Paper I evaluating at a set increment of magnetic longitude, until 360° are covered, and with a new grid of SECS for each meridian using the available magnetometers and applying the electrojet algorithm from Paper II. Another option is a global fit of the ground magnetometers to estimate the electrojet current using spherical harmonics or applying SECS globally, similar to how Lompe is used in *Hovland et al.* (2022). A global electrojet boundary would expand the basis for comparison with global auroral boundaries derived from auroral images, such as those presented by *Chisham et al.* (2022) and *Ohma et al.* (2023), both event-wise and statistically, to obtain offsets for an electrojet based auroral oval proxy and for an improved understanding of what conditions prevent a reasonable auroral oval proxy based on the electrojet. This approach might provide an alternative means for estimating the boundaries of the auroral oval when a more established approach, such as estimation via global images, is impossible due to either a lack of data (e.g., there is currently no global auroral imagery mission) or challenges associated with the methodology (e.g., dayglow removal). In addition, global properties of the electrojet such as the latitudinal integral of the eastward vector of the electrojet or its peak value can describe the electrojet in greater detail than compared to the auroral magnetic indices (e.g. AL/SML, AU/SMU).

Paper III successfully estimated the large scale substorm current wedge but demonstrated that estimates of the full current made exclusively via magnetic field measurements below the ionospheric current layer are not reliable without knowledge of the ionospheric conductance. The future mission Electrojet Zeeman Imaging Explorer (EZIE) satellites, that we discuss further in the next section, will resolve the mesoscale divergence-free current but cannot directly measure the curl-free current. The spatial scale of the estimated currents in Paper III is mostly limited by the spacing of the Iridium satellites orbits rather than the ground based magnetometers. On an event by event basis the Iridium satellites could be supplemented by including other satellite based magnetometers. As examples there are the *Swarm* collection of satellites, DMSP satellites, Ørsted and many more. An advantage of the lowest flying LEO satellites such as *Swarm* is that they can be used to constrain both the DF and CF currents. With this approach we would have a better chance of discerning between the single substorm current wedge, double wedge, or ensemble of wedgelets (*Gjerloev and Hoffman*, 2014; *Liu et al.*, 2013; *McPherron et al.*, 1973). If we find such events where spaced-based magnetometer density is sufficiently high that the distribution of the ground based magnetometers or their distance to the ionospheric current layer is the limiting factor in the resolvable scale size then the EZIE mission may be of greater use. However with currently available space-based magnetometers such an event is unlikely.

The KRM method described in section 3.5 uses only ground-based magnetometers to interpret the full ionospheric current by relating the equivalent current to the electric field through the conductance using ionospheric Ohm's Law. Given that Paper I has provided the equivalent current along a single meridian, we suggest that it may be advantageous to incorporate this dataset into a 1D approach similar to the KRM method. In this way also the FAC and electric field could be obtained along this meridian when the conductance can be defined either through measurements or statistical models.

8.2 Future Magnetic Field Measurements

Magnetic field measurements for estimating ionospheric currents are continually improving. The global network of ground based magnetometers has increased immensely in density and coverage over the last two decades and longer, primarily in the northern polar ionosphere. Furthermore, the temporal resolution of the available measurements has been improving: While the default globally is typically one minute, the IMAGE network provides measurements at a resolution of at least 10 s from all 58 magnetometers (for 53 of those magnetometers measurements are provided at a resolution of 1 s). Similarly, in recent years the SuperMAG collaboration has begun to provide a data product with a temporal resolution of 1 s for a selection of magnetometers. Space-based magnetometers are also seeing an increase in coverage which has made studies like Paper III possible. In this section we will discuss where magnetic field measurements for estimating the ionospheric current are going in the future and could go in the future and the implications for the progression of the studies within this thesis.

The Electrojet Zeeman Imaging Explorer (EZIE) satellites will be the first of their kind. They are designed to study the magnetic field below the ionospheric current layer through remote measurements (*Laundal et al.*, 2021; *Yee et al.*, 2021). They will measure the spectra of Oxygen emissions from about 80 km and how it is affected by the magnetic field through the Zeeman effect. The change in the spectra of the Oxygen emissions and their polarisation can be used to retrieve the magnitude and orientation of the magnetic field at around 80 km. This approach yields magnetic field measurements that are very noisy; however, *Laundal et al.* (2021) has shown that the techniques used in Paper I can be applied to the simulated EZIE magnetic field measurements to produce accurate estimates of the divergence-free current. There will be three satellites each with four beams (i.e. four tracks of measurements per satellite) in a "pearls on a string" orbit essentially measuring the magnetic field vector at approximately 80 km. This will allow the estimation of significantly smaller scale divergence-free currents compared to ground magnetometers and LEO satellites due to the physical spacing of the measurements and the proximity to the ionospheric current layer. These measurements have implications for Paper I and II. The electrojet current can be estimated at a greater spatial resolution leading to more accurate estimates of the electrojet boundaries and the other properties estimated in Paper II. The influence of GICs on the measurements is reduced due to the distance to the ground; these measurements are thus less affected by the steep conductance gradients between the sea and land. As previously mentioned, these measurements have little impact on Paper III as the spatial resolution of the full current of the ionospheric leg of the substorm current wedge is limited by the measurements of the curl-free current and EZIE will not be capable of such measurements.

The distance from the ionospheric current layer to the ground based magnetometers is a physical limitation of the scale sizes of the divergence-free currents that can be resolved using such measurements. There are few regions in the world that have such high density of magnetometers that the distance from the ionospheric current sets the limit of the scale sizes that can be resolved in the equivalent current. Increasing the density of ground magnetometers is obviously the solution for improving the spatial scales in the estimated divergence-free currents in Paper I and III, however, this is costly for conventional magnetometers. Low-cost magnetometers have been introduced as a part of an outreach concept for the EZIE mission, called "EZIE mags". They incorporate Raspberry Pi technology and will be distributed to a selection of high schools as not only a tool for learning, but also as a contribution to science. While these lost-cost magnetometers are not as accurate as the conventional ground magnetometers, preliminary tests have shown comparable signals to nearby observatory magnetometers. Introducing these magnetometers in the auroral zone can enable the estimated divergence-free currents to be at the finest possible spatial scales at which can be achieved from ground and will be more financially achievable than with current magnetometers. This is directly applicable for Paper I and II allowing the current to be resolved at smaller spatial scales and thus more accurate and higher resolution electrojet boundaries can be retrieved. There are still benefits for having an even greater density of magnetometers beyond what is necessary to resolve the divergence-free current at the highest resolution achievable from ground. This can help with identification and elimination of anomalous measurements, a greater understanding of the background magnetic field, such as magnetic anomalies, and deal with periods when magnetometers are not available which has limited the temporal coverage of the dataset produced in Paper I.

As demonstrated by Paper III and AMPERE, The Iridium constellation has shown that commercial satellite programs with magnetometers on board for operational purposes can be a significant contribution to science. If similar agreements with other such satellite programs could be reached to obtain magnetometer measurements, the FAC resolution could be significantly improved. This would have direct implications for Paper III allowing us to resolve more detail of the substorm current wedge and to better address the different theories on the formation and structure of the substorm current wedge.

Bibliography

Akasofu, S. I. (1964), The development of the auroral substorm, *Planetary and Space Science*, *12*(4), 273–282, doi:10.1016/0032-0633(64)90151-5. 2.3.1, 2.3.1, 2.3.1

Aksnes, A., J. Stadsnes, J. Bjordal, N. Østgaard, R. R. Vondrak, D. L. Detrick, T. J. Rosenberg, G. A. Germany, and D. Chenette (2002), Instantaneous ionospheric global conductance maps during an isolated substorm, *Annales Geophysicae*, *20*(8), 1181–1191, doi:10.5194/ANGEO-20-1181-2002. 3.3

Alken, P., E. Thébault, C. D. Beggan, H. Amit, J. Aubert, J. Baerenzung, T. N. Bondar, W. J. Brown, S. Califf, A. Chambodut, A. Chulliat, G. A. Cox, C. C. Finlay, A. Fournier, N. Gillet, A. Grayver, M. D. Hammer, M. Holschneider, L. Huder, G. Hulot, T. Jager, C. Kloss, M. Korte, W. Kuang, A. Kuvshinov, B. Langlais, J. M. Léger, V. Lesur, P. W. Livermore, F. J. Lowes, S. Macmillan, W. Magnes, M. Mandea, S. Marsal, J. Matzka, M. C. Metman, T. Minami, A. Morschhauser, J. E. Mound, M. Nair, S. Nakano, N. Olsen, F. J. Pavón-Carrasco, V. G. Petrov, G. Ropp, M. Rother, T. J. Sabaka, S. Sanchez, D. Saturnino, N. R. Schnepf, X. Shen, C. Stolle, A. Tangborn, L. Tøffner-Clausen, H. Toh, J. M. Torta, J. Varner, F. Vervelidou, P. Vigneron, I. Wardinski, J. Wicht, A. Woods, Y. Yang, Z. Zeren, and B. Zhou (2021), International Geomagnetic Reference Field: the thirteenth generation, *Earth, Planets and Space*, *73*(1), 1–25, doi:10.1186/s40623-020-01288-x. 4.1.2

Amm, O. (1997), Ionospheric Elementary Current Systems in Spherical Coordinates and Their Application, *J. Geomag. Geoelectr*, *49*(7), 947–955, doi:10.5636/jgg.49.947. 5.1

Amm, O., and A. Viljanen (1999), Ionospheric disturbance magnetic field continuation from the ground to the ionosphere using spherical elementary current systems, *Earth, Planets and Space*, *51*(6), 431–440, doi:10.1186/BF03352247. 5.1

Amm, O., M. J. Engebretson, T. Hughes, L. Newitt, A. Viljanen, and J. Watermann (2002), A traveling convection vortex event study: Instantaneous ionospheric equivalent currents, estimation of field-aligned currents, and the role of induced currents, *Journal of Geophysical Research: Space Physics*, *107*(A11), 1–1, doi:10.1029/2002JA009472. 3.3

Anderson, B. J., K. Takahashi, and B. A. Toth (2000), Sensing global Birkeland currents with iridium® engineering magnetometer data, *Geophysical Research Letters*, *27*(24), 4045–4048, doi:10.1029/2000GL000094. 1, 4.2, 4.2, 6.2

Anderson, B. J., H. Korth, C. L. Waters, D. L. Green, V. G. Merkin, R. J. Barnes, and L. P. Dyrud (2014), Development of large-scale Birkeland currents determined from the Active Magnetosphere and Planetary Electrodynamics Response Experiment, *Geophysical Research Letters*, *41*(9), 3017–3025, doi:10.1002/2014GL059941. 1

Anderson, P. C., and H. C. Koons (1996), Spacecraft Charging Anomaly on a Low-Altitude Satellite in an Aurora, *Journal of Spacecraft and Rockets*, *33*(5), 734–738, doi:10.2514/3.26828. 1

Andersson, L., W. K. Peterson, and K. M. McBryde (2004), Dynamic coordinates for auroral ion outflow, *Journal of Geophysical Research: Space Physics*, *109*(A8), 8201, doi:10.1029/2004JA010424. 2.2.4

Angelopoulos, V., J. P. McFadden, D. Larson, C. W. Carlson, S. B. Mende, H. Frey, T. Phan, D. G. Sibeck, K. H. Glassmeier, U. Auster, E. Donovan, I. R. Mann, I. J. Rae, C. T. Russell, A. Runov, X. Z. Zhou, and L. Kepko (2008), Tail reconnection triggering substorm onset, *Science*, *321*(5891), 931–935, doi:10.1126/science.1160495. 2.3

Borovsky, J. E. (2008), Flux tube texture of the solar wind: Strands of the magnetic carpet at 1 AU?, *Journal of Geophysical Research: Space Physics*, *113*(A8), doi: 10.1029/2007JA012684. 2.2.1

Boström, R. (1964), A model of the auroral electrojets, *Journal of Geophysical Research*, *69*(23), 4983–4999, doi:10.1029/JZ069I023P04983. 3.3

Boström, R. (1970), *Electrodynamics of the ionosphere*, KTH Royal Institute of Technology. 3.1

Boteler, D. H. (2019), A 21st Century View of the March 1989 Magnetic Storm, *Space Weather*, *17*(10), 1427–1441, doi:10.1029/2019SW002278. 1

Burrell, A. G., G. Chisham, S. E. Milan, L. Kilcommons, Y. J. Chen, E. G. Thomas, and B. Anderson (2020), AMPERE polar cap boundaries, *Annales Geophysicae*, *38*(2), 481–490, doi:10.5194/angeo-38-481-2020. 2.2.3

Carter, J. A., S. E. Milan, C. Forsyth, M. E. Lester, M. T. Walach, J. Gjerloev, L. J. Paxton, and B. J. Anderson (2023), Mean Energy Flux, Associated Derived Height-Integrated Conductances, and Field-Aligned Current Magnitudes Evolve Differently During a Substorm, *Journal of Geophysical Research: Space Physics*, *128*(2), e2022JA030,942, doi:10.1029/2022JA030942. 3.5

Chapman, S., and J. Bartels (1940), Geomagnetism, Vol. II: Analysis of the Data, and Physical Theories, *Geomagnetism*. 2.1

Chapman, S., and J. Bartels (1962), *Geomagnetism*, vol. 1, Clarendon Press. 2.1, 3.1

Chisham, G., A. G. Burrell, E. G. Thomas, and Y. J. Chen (2022), Ionospheric Boundaries Derived From Auroral Images, *Journal of Geophysical Research: Space Physics*, *127*(7), doi:10.1029/2022JA030622. 1, 2.2.4, 2.2.4, 6.1, 8.1

Clauer, C. R., and R. L. McPherron (1974), Mapping the local time-universal time development of magnetospheric substorms using mid-latitude magnetic observations, *Journal of Geophysical Research*, *79*(19), 2811–2820, doi:10.1029/ja079i019p02811. 2.3.2

Collaboration, T. A., A. M. Price-Whelan, P. L. Lim, N. Earl, N. Starkman, L. Bradley, D. L. Shupe, A. A. Patil, L. Corrales, C. E. Brasseur, M. Nöthe, A. Donath, E. Tollerud, B. M. Morris, A. Ginsburg, E. Vaher, B. A. Weaver, J. Tocknell, W. Jamieson, M. H. v. Kerkwijk, T. P. Robitaille, B. Merry, M. Bachetti, H. M. Günther, P. Authors, T. L. Aldcroft, J. A. Alvarado-Montes, A. M. Archibald, A. Bódi, S. Bapat, G. Barentsen, J. Bazán, M. Biswas, M. Boquien, D. J. Burke, D. Cara, M. Cara, K. E. Conroy, S. Conseil, M. W. Craig, R. M. Cross, K. L. Cruz, F. DEugenio, N. Dencheva, H. A. R. Devillepoix, J. P. Dietrich, A. D. Eigenbrot, T. Erben, L. Ferreira, D. Foreman-Mackey, R. Fox, N. Freij, S. Garg, R. Geda, L. Glattly, Y. Gondhalekar, K. D. Gordon, D. Grant, P. Greenfield, A. M. Groener, S. Guest, S. Gurovich, R. Handberg, A. Hart, Z. Hatfield-Dodds, D. Homeier, G. Hosseinzadeh, T. Jenness, C. K. Jones, P. Joseph, J. B. Kalmbach, E. Karamehmetoglu, M. Kałuszyński, M. S. P. Kelley, N. Kern, W. E. Kerzendorf, E. W. Koch, S. Kulumani, A. Lee, C. Ly, Z. Ma, C. MacBride, J. M. Maljaars, D. Muna, N. A. Murphy, H. Norman, R. OSteen, K. A. Oman, C. Pacifici, S. Pascual, J. Pascual-Granado, R. R. Patil, G. I. Perren, T. E. Pickering, T. Rastogi, B. R. Roulston, D. F. Ryan, E. S. Rykoff, J. Sabater, P. Sakurikar, J. Salgado, A. Sanghi, N. Saunders, V. Savchenko, L. Schwardt, M. Seifert-Eckert, A. Y. Shih, A. S. Jain, G. Shukla, J. Sick, C. Simpson, S. Singanamalla, L. P. Singer, J. Singhal, M. Sinha, B. M. Sipőcz, L. R. Spitler, D. Stansby, O. Streicher, J. Šumak, J. D. Swinbank, D. S. Taranu, N. Tewary, G. R. Tremblay, M. d. Val-Borro, S. J. V. Kooten, Z. Vasović, S. Verma, J. V. d. M. Cardoso, P. K. G. Williams, T. J. Wilson, B. Winkel, W. M. Wood-Vasey, R. Xue, P. Yoachim, C. Zhang, A. Zonca, and A. P. Contributors (2022), The Astropy Project: Sustaining and Growing a Community-oriented Open-source Project and the Latest Major Release (v5.0) of the Core Package*, *The Astrophysical Journal*, *935*(2), 167, doi:10.3847/1538-4357/AC7C74. 4.2

Cowley, S. W. H., and M. Lockwood (1992), Excitation and decay of solar wind-driven flows in the magnetosphere-ionosphere system, *Annales geophysicae*, *10*(1-2), 103–115. 6.1

Coxon, J. C., S. E. Milan, and B. J. Anderson (2018), A Review of Birkeland Current Research Using AMPERE, *Electric Currents in Geospace and Beyond*, pp. 257–278, doi:10.1002/9781119324522.CH16. 1

Croisille, J. P. (2013), Hermitian compact interpolation on the cubed-sphere grid, *Journal of Scientific Computing*, *57*(1), 193–212, doi:10.1007/s10915-013-9702-3. 5.2

Decotte, M., K. M. Laundal, S. M. Hatch, and J. P. Reistad (2023), Auroral Oval Morphology: Dawn-Dusk Asymmetry Partially Induced by Earth's Rotation, *Journal of Geophysical Research: Space Physics*, *128*(6), e2023JA031,345, doi:10.1029/2023JA031345. 2.2.4, 6.1

Dungey, J. W. (1961), Interplanetary magnetic field and the auroral zones, *Physical Review Letters*, *6*(2), 47–48, doi:10.1103/PhysRevLett.6.47. 1, 2.2.2

Ebihara, Y., S. Watari, and S. Kumar (2021), Prediction of geomagnetically induced currents (GICs) flowing in Japanese power grid for Carrington-class magnetic storms, *Earth, Planets and Space*, *73*(1), 1–10, doi:10.1186/s40623-021-01493-2. 1

Feldstein, Y. I., and G. V. Starkov (1967), Dynamics of auroral belt and polar geomagnetic disturbances, *Planetary and Space Science*, *15*(2), 209–229, doi:10.1016/0032-0633(67)90190-0. 6.1

Feldstein, Y. I., L. I. Gromova, A. Grafe, C. I. Meng, V. V. Kalegaev, I. I. Alexeev, and Y. P. Sumaruk (1999), Dynamics of the auroral electrojets and their mapping to the magnetosphere, *Radiation Measurements*, *30*(5), 579–587, doi:10.1016/S1350-4487(99)00219-X. 1

Finlay, C. C., C. Kloss, N. Olsen, M. D. Hammer, L. Tøffner-Clausen, A. Grayver, and A. Kuvshinov (2020), The CHAOS-7 geomagnetic field model and observed changes in the South Atlantic Anomaly, *Earth, Planets and Space*, *72*(1), 1–31, doi:10.1186/s40623-020-01252-9. 4.1.2

Forsyth, C., I. J. Rae, J. C. Coxon, M. P. Freeman, C. M. Jackman, J. Gjerloev, and A. N. Fazakerley (2015), A new technique for determining Substorm Onsets and Phases from Indices of the Electrojet (SOPHIE), *Journal of Geophysical Research: Space Physics*, *120*(12), 10,592–10,606, doi:10.1002/2015JA021343. 2.6, 6.1

Fukushima, N. (1994), Some topics and historical episodes in geomagnetism and aeronomy, *Journal of Geophysical Research*, *99*(A10), 19,113, doi:10.1029/94ja00102. 3.3

Gjerloev, J. W. (2012), The SuperMAG data processing technique, *Journal of Geophysical Research: Space Physics*, *117*(9), doi:10.1029/2012JA017683. 4.1.1, 4.1.1

Gjerloev, J. W., and R. A. Hoffman (2014), The large-scale current system during auroral substorms, *Journal of Geophysical Research: Space Physics*, *119*(6), 4591–4606, doi:10.1002/2013JA019176. 1, 1, 2.3.2, 3.3, 8.1

Grayver, A. V., A. Kuvshinov, and D. Werthmüller (2021), Time-Domain Modeling of Three-Dimensional Earth's and Planetary Electromagnetic Induction Effect in Ground and Satellite Observations, *Journal of Geophysical Research: Space Physics*, *126*(3), e2020JA028,672, doi:10.1029/2020JA028672. 5.3

Green, D. L., C. L. Waters, H. Korth, B. J. Anderson, A. J. Ridley, and R. J. Barnes (2007), Technique: Large-scale ionospheric conductance estimated from combined satellite and ground-based electromagnetic data, *Journal of Geophysical Research: Space Physics*, *112*(5), n/a–n/a, doi:10.1029/2006JA012069. 1, 2.1

Green, J. L., S. Boardsen, S. Odenwald, J. Humble, and K. A. Pazamickas (2006), Eyewitness reports of the great auroral storm of 1859, *Advances in Space Research*, *38*(2), 145–154, doi:10.1016/J.ASR.2005.12.021. 1

Han, Y., B. Han, Z. Hu, X. Gao, L. Zhang, H. Yang, and B. Li (2020), Prediction and variation of the auroral oval boundary based on a deep learning model and space physical parameters, *Nonlinear Processes in Geophysics*, *27*(1), 11–22, doi:10.5194/NPG-27-11-2020. 1

Helmholtz, H. (1858), Über Integrale der hydrodynamischen Gleichungen, welche den Wirbelbewegungen entsprechen, *Journal fur die Reine und Angewandte Mathematik*, *1858*(55), 25–55, doi:10.1515/crll.1858.55.25. 3.2

Hovland, A., K. M. Laundal, J. P. Reistad, S. M. Hatch, S. J. Walker, M. Madelaire, and A. Ohma (2022), The Lompe code: A Python toolbox for ionospheric data analysis, *Frontiers in Astronomy and Space Sciences*, *9*, 1025,823, doi:10.3389/FSPAS.2022.1025823/BIBTEX. 8.1

Janzhura, A. S., and O. A. Troshichev (2008), Determination of the running quiet daily geomagnetic variation, *Journal of Atmospheric and Solar-Terrestrial Physics*, *70*(7), 962–972, doi:10.1016/J.JASTP.2007.11.004. 6.2

Johnsen, M. G. (2013), Real-time determination and monitoring of the auroral electrojet boundaries, *Journal of Space Weather and Space Climate*, *3*, A28, doi:10.1051/swsc/2013050. 6.1

Juusola, L., N. Østgaard, E. Tanskanen, N. Partamies, and K. Snekvik (2011), Earthward plasma sheet flows during substorm phases, *Journal of Geophysical Research: Space Physics*, *116*(10), doi:10.1029/2011JA016852. 2.3, 2.3.1, 2.3.1, 2.3.1, 2.3.2

Juusola, L., K. Kauristie, H. Vanhamäki, A. Aikio, and M. van de Kamp (2016), Comparison of auroral ionospheric and field-aligned currents derived from Swarm and ground magnetic field measurements, *Journal of Geophysical Research A: Space Physics*, *121*(9), 9256–9283, doi:10.1002/2016JA022961. 3.4, 5.3

Juusola, L., H. Vanhamäki, A. Viljanen, and M. Smirnov (2020), Induced currents due to 3D ground conductivity play a major role in the interpretation of geomagnetic variations, *Annales Geophysicae*, *38*(5), 983–998, doi:10.5194/angeo-38-983-2020. 3.4, 5.3, 5.3

Kamide, Y., A. D. Richmond, and S. Matsushita (1981), Estimation of ionospheric electric fields, ionospheric currents, and field-aligned currents from ground magnetic records, *Journal of Geophysical Research*, *86*(A2), 801, doi:10.1029/ja086ia02p00801. 1, 3.5

Kepko, L., R. L. McPherron, O. Amm, S. Apatenkov, W. Baumjohann, J. Birn, M. Lester, R. Nakamura, T. I. Pulkkinen, and V. Sergeev (2015), Substorm Current Wedge Revisited, *Space Science Reviews*, *190*(1-4), 1–46, doi:10.1007/s11214-014-0124-9. 2.3.2

Kilcommons, L. M., R. J. Redmon, and D. J. Knipp (2017), A new DMSP magnetometer and auroral boundary data set and estimates of field-aligned currents in dynamic auroral boundary coordinates, *Journal of Geophysical Research: Space Physics*, *122*(8), 9068–9079, doi:10.1002/2016JA023342. 2.2.3, 2.2.4, 6.1

King, J. H., and N. E. Papitashvili (2005), Solar wind spatial scales in and comparisons of hourly Wind and ACE plasma and magnetic field data, *Journal of Geophysical Research: Space Physics*, *110*(A2), A02,104, doi:10.1029/2004JA010649. 2.2.1

Knipp, D. J., B. A. Emery, and G. Lu (1994), Application of the Assimilative Mapping of Ionospheric Electrodynamics (AMIE) Procedure to CUSP Identification, *Physical Signatures of Magnetospheric Boundary Layer Processes*, pp. 401–420, doi:10.1007/978-94-011-1052-5_28. 3.5

Korja, T., M. Engels, A. A. Zhamaletdinov, A. A. Kovtun, N. A. Palshin, M. Y. Smirnov, A. D. Tokarev, V. E. Asming, L. L. Vanyan, and I. L. Vardaniants (2002), Crustal conductivity in Fennoscandia - A compilation of a database on crustal conductance in the Fennoscandian Shield, *Earth, Planets and Space*, *54*(5), 535–558, doi:10.1186/BF03353044/METRICS. 3.4, 3.2

Laundal, K., and J. Reistad (2022), klaundal/secsy: secsy, doi:10.5281/ZENODO.5962562. 5.2

Laundal, K. M., and M. Toresen (2018), klaundal/pyAMPS: pyAMPS 0.1.0, doi:10.5281/ZENODO.1182931. 6.1, 6.1

Laundal, K. M., S. E. Haaland, N. Lehtinen, J. W. Gjerloev, N. Østgaard, P. Tenfjord, J. P. Reistad, K. Snekvik, S. E. Milan, S. Ohtani, and B. J. Anderson (2015), Birkeland current effects on high-latitude ground magnetic field perturbations, *Geophysical Research Letters*, *42*(18), 7248–7254, doi:10.1002/2015GL065776. 3.2

Laundal, K. M., C. C. Finlay, N. Olsen, and J. P. Reistad (2018), Solar Wind and Seasonal Influence on Ionospheric Currents From Swarm and CHAMP Measurements, *Journal of Geophysical Research: Space Physics*, *123*(5), 4402–4429, doi:10.1029/2018JA025387. 3.2

Laundal, K. M., J.-H. H. Yee, V. G. Merkin, J. W. Gjerloev, H. Vanhamäki, J. P. Reistad, M. Madelaire, K. Sorathia, and P. J. Espy (2021), Electrojet estimates from mesospheric magnetic field measurements, *Journal of Geophysical Research: Space Physics*, *126*(5), 1–17, doi:10.1029/2020ja028644. 5.2, 5.4, 5.4, 8.2

Laundal, K. M., J. P. Reistad, S. M. Hatch, M. Madelaire, S. J. Walker, A. Ø. Hovland, A. Ohma, V. G. Merkin, and K. A. Sorathia (2022), Local Mapping of Polar Ionospheric Electrodynamics, *Journal of Geophysical Research: Space Physics*, *127*(5), doi:10.1029/2022JA030356. 1, 3.3, 3.5, 3.3, 5.2, 6.1

Liu, J., V. Angelopoulos, A. Runov, and X. Z. Zhou (2013), On the current sheets surrounding dipolarizing flux bundles in the magnetotail: The case for wedgelets, *Journal of Geophysical Research: Space Physics*, *118*(5), 2000–2020, doi:10.1002/JGRA.50092. 1, 2.3.2, 8.1

Liu, J., V. Angelopoulos, X. Chu, X. Z. Zhou, and C. Yue (2015), Substorm current wedge composition by wedgelets, *Geophysical Research Letters*, *42*(6), 1669–1676, doi:10.1002/2015GL063289. 2.3.2

Lockwood, M. (2022), Solar WindMagnetosphere Coupling Functions: Pitfalls, Limitations, and Applications, *Space Weather*, *20*(2), e2021SW002,989, doi:10.1029/2021SW002989. 1, 2.2.1, 2.2.1

Lockwood, M., and S. W. H. Cowley (1992), Ionospheric convection and the substorm cycle, in *Substorms 1, Proceedings of the First International Conference on Substorms, ICS-1*, edited by C. Mattock, Eur. Space Agency Publ., Noordvijk. 6.1

Longden, N., G. Chisham, M. P. Freeman, G. A. Abel, and T. Sotirelis (2010), Estimating the location of the open-closed magnetic field line boundary from auroral images, *Annales Geophysicae*, *28*(9), 1659–1678, doi:10.5194/ANGEO-28-1659-2010. 2.2.4, 2.2.4

Madelaire, M., K. M. Laundal, J. P. Reistad, S. M. Hatch, A. Ohma, and S. Haaland (2022), Geomagnetic Response to Rapid Increases in Solar Wind Dynamic Pressure: Event Detection and Large Scale Response, *Frontiers in Astronomy and Space Sciences*, *9*, 188, doi:10.3389/fspas.2022.904620. 6.1

Marghitu, O. (2013), Auroral Arc Electrodynamics: Review and Outlook, *Auroral Phenomenology and Magnetospheric Processes: Earth and Other Planets*, pp. 143–158, doi:10.1029/2011GM001189. 3.3

McPherron, R. L. (1970), Growth Phase of Magnetospheric Substorms, *Journal of Geophysical Research: Space Physics*, *75*(28), 5592–5599, doi:https://doi.org/10.1029/JA075i028p05592. 2.3.1

McPherron, R. L., C. T. Russell, and M. P. Aubry (1973), Satellite studies of magnetospheric substorms on August 15, 1968: 9. Phenomenological model for substorms, *Journal of Geophysical Research*, *78*(16), 3131–3149, doi:10.1029/JA078I016P03131. 1, 2.7, 8.1

Mende, S. B., H. U. Frey, and V. Angelopoulos (2016), Source of the dayside cusp aurora, *Journal of Geophysical Research: Space Physics*, *121*(8), 7728–7738, doi:10.1002/2016JA022657. 1, 2.2.2

Merkin, V. G., E. V. Panov, K. A. Sorathia, and A. Y. Ukhorskiy (2019), Contribution of Bursty Bulk Flows to the Global Dipolarization of the Magnetotail During an Isolated Substorm, *Journal of Geophysical Research: Space Physics*, *124*(11), 8647–8668, doi:10.1029/2019JA026872. 2.3.2

Milan, S. E. (2004), Dayside and nightside contributions to the cross polar cap potential: placing an upper limit on a viscous-like interaction, *Annales Geophysicae*, *22*(10), 3771–3777, doi:10.5194/ANGEO-22-3771-2004. 2.2.3

Milan, S. E. (2013), Modeling Birkeland currents in the expanding/contracting polar cap paradigm, *J. Geophys. Res. Space Physics*, *118*, 5532–5542, doi:10.1002/jgra.50393. 6.1

Milan, S. E., J. A. Wild, B. Hubert, C. M. Carr, E. A. Lucek, J. M. Bosqued, J. F. Watermann, and J. A. Slavin (2006), Flux closure during a substorm observed by

Cluster, Double Star, IMAGE FUV, SuperDARN, and Greenland magnetometers, *Annales Geophysicae*, *24*(2), 751–767, doi:10.5194/ANGEO-24-751-2006. 1

Milan, S. E., G. Provan, and B. Hubert (2007), Magnetic flux transport in the Dungey cycle: A survey of dayside and nightside reconnection rates, *Journal of Geophysical Research: Space Physics*, *112*(A1), 1209, doi:10.1029/2006JA011642. 1

Milan, S. E., P. D. Boakes, and B. Hubert (2008), Response of the expanding/contracting polar cap to weak and strong solar wind driving: Implications for substorm onset, *Journal of Geophysical Research: Space Physics*, *113*(A9), 9215, doi: 10.1029/2008JA013340. 1

Milan, S. E., J. S. Gosling, and B. Hubert (2012), Relationship between interplanetary parameters and the magnetopause reconnection rate quantified from observations of the expanding polar cap, *Journal of Geophysical Research: Space Physics*, *117*(A3), 3226, doi:10.1029/2011JA017082. 2.2.1

Milan, S. E., L. B. Clausen, J. C. Coxon, J. A. Carter, M. T. Walach, K. Laundal, N. Østgaard, P. Tenfjord, J. Reistad, K. Snekvik, H. Korth, and B. J. Anderson (2017), Overview of Solar WindMagnetosphereIonosphereAtmosphere Coupling and the Generation of Magnetospheric Currents, doi:10.1007/s11214-017-0333-0. 1

Newell, P. T., and J. W. Gjerloev (2011), Substorm and magnetosphere characteristic scales inferred from the SuperMAG auroral electrojet indices, *Journal of Geophysical Research: Space Physics*, *116*(12), n/a–n/a, doi:10.1029/2011JA016936. 6.1

Newell, P. T., Y. I. Feldstein, Y. I. Galperin, and C.-I. Meng (1996), Morphology of nightside precipitation, *Journal of Geophysical Research: Space Physics*, *101*(A5), 10,737–10,748, doi:10.1029/95JA03516. 2.2.3, 2.2.4, 6.1

Newell, P. T., T. Sotirelis, K. Liou, C. I. Meng, and F. J. Rich (2007), A nearly universal solar wind-magnetosphere coupling function inferred from 10 magnetospheric state variables, *Journal of Geophysical Research: Space Physics*, *112*(1), 1206, doi:10.1029/2006JA012015. 2.2.1, 2.2.1

Nishimura, Y., L. R. Lyons, C. Gabrielse, J. M. Weygand, E. F. Donovan, and V. Angelopoulos (2020), Relative contributions of large-scale and wedgelet currents in the substorm current wedge, *Earth, Planets and Space*, *72*(1), 1–10, doi: 10.1186/S40623-020-01234-X/FIGURES/6. 1, 3.3

Nosé, M., T. Iyemori, M. Sugiura, and J. A. Slavin (1995), A strong dawn/dusk asymmetry in Pc5 pulsation occurrence observed by the DE1 satellite, *Geophysical Research Letters*, *22*(15), 2053–2056, doi:10.1029/95GL01794. 6.1

Ohma, A., K. Laundal, M. Madelaire, S. M. Hatch, S. Gasparini, J. P. Reistad, S. J. Walker, and M. Decotte (2023), Excitation and decay of the auroral oval, *Authorea Preprints*, doi:10.22541/ESSOAR.169447428.84472457/V1. 2.2.3, 2.4, 2.2.4, 2.2.4, 2.5, 8.1

Ohtani, S., and J. W. Gjerloev (2020), Is the Substorm Current Wedge an Ensemble of Wedgelets?: Revisit to Midlatitude Positive Bays, *Journal of Geophysical Research: Space Physics*, *125*(9), e2020JA027,902, doi:10.1029/2020JA027902. 6.1

Palmroth, M., M. Grandin, T. Sarris, E. Doornbos, S. Tourgaidis, A. Aikio, S. Buchert, M. A. Clilverd, I. Dandouras, R. Heelis, A. Hoffmann, N. Ivchenko, G. Kervalishvili, D. J. Knudsen, A. Kotova, H. L. Liu, D. M. Malaspina, G. March, A. Marchaudon, O. Marghitu, T. Matsuo, W. J. Miloch, T. Moretto-Jørgensen, D. Mpaloukidis, N. Olsen, K. Papadakis, R. Pfaff, P. Pirnaris, C. Siemes, C. Stolle, J. Suni, J. Van Den Ijssel, P. T. Verronen, P. Visser, and M. Yamauchi (2021), Lower-Thermosphere-ionosphere (LTI) quantities: Current status of measuring techniques and models, *Annales Geophysicae*, *39*(1), 189–237, doi:10.5194/ANGEO-39-189-2021. 2.3

Park, S. K., and R. A. Schowengerdt (1983), Image reconstruction by parametric cubic convolution, *Computer Vision, Graphics, and Image Processing*, *23*(3), 258–272, doi:10.1016/0734-189X(83)90026-9. 4.1.1

Partamies, N., L. Juusola, E. Tanskanen, and K. Kauristie (2013), Statistical properties of substorms during different storm and solar cycle phases, *Annales Geophysicae*, *31*(2), 349–358, doi:10.5194/ANGEO-31-349-2013. 2.3.1, 2.3.1, 2.3.1

Pedatella, N. M., J. M. Forbes, and A. D. Richmond (2011), Seasonal and longitudinal variations of the solar quiet (Sq) current system during solar minimum determined by CHAMP satellite magnetic field observations, *Journal of Geophysical Research: Space Physics*, *116*(4), 4317, doi:10.1029/2010JA016289. 3.1

Pettigrew, E. D., S. G. Shepherd, and J. M. Ruohoniemi (2010), Climatological patterns of high-latitude convection in the Northern and Southern hemispheres: Dipole tilt dependencies and interhemispheric comparisons, *Journal of Geophysical Research: Space Physics*, *115*(7), doi:10.1029/2009JA014956. 2.2.2

Redmon, R. J., W. K. Peterson, L. Andersson, E. A. Kihn, W. F. Denig, M. Hairston, and R. Coley (2010), Vertical thermal O+ flows at 850 km in dynamic auroral boundary coordinates, *Journal of Geophysical Research: Space Physics*, *115*(A11), 0–08, doi:10.1029/2010JA015589. 2.2.3

Reistad, J. P., K. M. Laundal, N. Østgaard, A. Ohma, A. G. Burrell, S. M. Hatch, S. Haaland, and E. G. Thomas (2021), Quantifying the Lobe Reconnection Rate During Dominant IMF By Periods and Different Dipole Tilt Orientations, *Journal of Geophysical Research: Space Physics*, *126*(11), e2021JA029,742, doi:10.1029/2021JA029742. 2.2.2

Richmond, A. D. (1992), Assimilative mapping of ionospheric electrodynamics, *Advances in Space Research*, *12*(6), 59–68, doi:10.1016/0273-1177(92)90040-5. 1, 3.5

Richmond, A. D. (2007), Ionosphere, *Encyclopedia of Geomagnetism and Paleomagnetism*, pp. 452–454, doi:10.1007/978-1-4020-4423-6_159. 2.1

Richmond, A. D., and Y. Kamide (1988), Mapping electrodynamic features of the high-latitude ionosphere from localized observations: Technique, *Journal of Geophysical Research: Space Physics*, *93*(A6), 5741–5759, doi:10.1029/JA093IA06P05741. 3.5

Richmond, A. D., G. Lu, B. A. Emery, and D. J. Knipp (1998), The Amie procedure: Prospects for space weather specification and prediction, *Advances in Space Research*, *22*(1), 103–112, doi:10.1016/S0273-1177(97)01108-3. 3.5

Rishbeth, H., and O. K. Garriott (1969), III. Photochemical Processes in the Ionosphere, in *Introduction to Ionospheric Physics*, *International Geophysics*, vol. 14, edited by H. Rishbeth and O. K. Garriott, pp. 87–125, Academic Press, doi:https://doi.org/10.1016/S0074-6142(09)60023-1. 2.1

Robinson, R. M., R. R. Vondrak, K. Miller, T. Dabbs, and D. Hardy (1987), On calculating ionospheric conductances from the flux and energy of precipitating electrons, *Journal of Geophysical Research*, *92*(A3), 2565, doi:10.1029/ja092ia03p02565. 2.1

Ronchi, C., R. Iacono, and P. S. Paolucci (1996), The ".Cubed sphere": A new method for the solution of partial differential equations in spherical geometry, *Journal of Computational Physics*, *124*(1), 93–114, doi:10.1006/jcph.1996.0047. 5.2

Runov, A., V. Angelopoulos, A. V. Artemyev, J. M. Weygand, S. Lu, Y. Lin, and X. J. Zhang (2021), Global and local processes of thin current sheet formation during substorm growth phase, *Journal of Atmospheric and Solar-Terrestrial Physics*, *220*, 105,671, doi:10.1016/J.JASTP.2021.105671. 2.3.1

Sadourny, R. (1972), Conservative Finite-Difference Approximations of the Primitive Equations on Quasi-Uniform Spherical Grids, *Monthly Weather Review*, *100*(2), 136–144, doi:10.1175/1520-0493(1972)100<0136:CFAOTP>2.3.CO;2. 5.2

Seki, K., A. Nagy, C. M. Jackman, F. Crary, D. Fontaine, P. Zarka, P. Wurz, A. Milillo, J. A. Slavin, D. C. Delcourt, M. Wiltberger, R. Ilie, X. Jia, S. A. Ledvina, M. W. Liemohn, and R. W. Schunk (2015), A Review of General Physical and Chemical Processes Related to Plasma Sources and Losses for Solar System Magnetospheres, doi:10.1007/s11214-015-0170-y. 2.2

Sotirelis, T., J. M. Ruohoniemi, R. J. Barnes, P. T. Newell, R. A. Greemvald, J. P. Skura, and C. I. Meng (2005), Comparison of SuperDARN radar boundaries with DMSP particle precipitation boundaries, *Journal of Geophysical Research: Space Physics*, *110*(A6), 6302, doi:10.1029/2004JA010732. 2.2.4

Taltavall, T. R. (1915), Aurora and Earth currents, *Telegr. Teleph. Age Telegr. Teleph. Radio*, *33*(23), 549. 1

Tanskanen, E. I., A. Viljanen, T. I. Pulkkinen, R. Pirjola, L. Häkkinen, A. Pulkkinen, and O. Amm (2001), At substorm onset, 40% of AL comes from underground, *Journal of Geophysical Research: Space Physics*, *106*(A7), 13,119–13,134, doi:10.1029/2000ja900135. 3.4, 5.3, 5.3

Untiedt, J., and W. Baumjohann (1993), Studies of polar current systems using the IMS Scandinavian magnetometer array, *Space Science Reviews*, *63*(3-4), 245–390, doi:10.1007/BF00750770. 2.1

Van De Kamp, M. (2013), Harmonic quiet-day curves as magnetometer baselines for ionospheric current analyses, *Geoscientific Instrumentation, Methods and Data Systems*, *2*(2), 289–304, doi:10.5194/GI-2-289-2013. 6.2

Vanhamäki, H., and L. Juusola (2020), Introduction to Spherical Elementary Current Systems, in *Ionospheric Multi-Spacecraft Analysis Tools*, pp. 5–33, Springer International Publishing, doi:10.1007/978-3-030-26732-2_2. 2.1, 3.2, 5.1, 5.1, 5.1, 5.2, 6.1

Vasyliunas, V. M. (2012), The physical basis of ionospheric electrodynamics, *Annales Geophysicae*, *30*(2), 357–369, doi:10.5194/angeo-30-357-2012. 3.1

Waters, C. L., B. J. Anderson, D. L. Green, H. Korth, R. J. Barnes, and H. Vanhamäki (2020), Science Data Products for AMPERE, *Ionospheric Multi-Spacecraft Analysis Tools*, pp. 141–165, doi:10.1007/978-3-030-26732-2_7. 1

Weygand, J. M., and S. Wing (2016), Comparison of DMSP and SECS region-1 and region-2 ionospheric current boundary, *Journal of Atmospheric and Solar-Terrestrial Physics*, *143-144*, 8–13, doi:10.1016/j.jastp.2016.03.002. 1, 3.3

Weygand, J. M., M. J. Engebretson, V. A. Pilipenko, E. S. Steinmetz, M. B. Moldwin, M. G. Connors, Y. Nishimura, L. R. Lyons, C. T. Russell, S. I. Ohtani, and J. Gjerloev (2021), SECS Analysis of Nighttime Magnetic Perturbation Events Observed in Arctic Canada, *Journal of Geophysical Research: Space Physics*, *126*(11), e2021JA029,839, doi:10.1029/2021JA029839. 1

Yee, J. H., J. Gjerloev, and D. Wu (2021), Remote Sensing of Magnetic Fields Induced by Electrojets From Space: Measurement Techniques and Sensor Design, in *Space Physics and Aeronomy, Upper Atmosphere Dynamics and Energetics*, pp. 451–468, wiley, doi:10.1002/9781119815631.ch21. 8.2

Zmuda, A. J., J. H. Martin, and F. T. Heuring (1966), Transverse magnetic disturbances at 1100 kilometers in the auroral region, *Journal of Geophysical Research*, *71*(21), 5033–5045, doi:10.1029/jz071i021p05033. 3.3

Papers

Paper I

Statistical Temporal Variations in the Auroral Electrojet Estimated With Ground Magnetometers in Fennoscandia

S.J. Walker, K.M. Laundal, J.P. Reistad, A. Ohma, S.M. Hatch

Space Weather, **21**, https://doi.org/10.1029/2022SW003305 (2023)

Space Weather®

RESEARCH ARTICLE
10.1029/2022SW003305

Statistical Temporal Variations in the Auroral Electrojet Estimated With Ground Magnetometers in Fennoscandia

Simon Walker[1], **Karl Laundal**[1], **Jone Reistad**[1], **Anders Ohma**[1], **and Spencer Hatch**[1]

[1]Department of Physics and Technology, Birkeland Centre for Space Science, University of Bergen, Bergen, Norway

Key Points:

- A new inversion technique for Spherical Elementary Current analysis is implemented and tested
- A new data set based on a fixed set of ground magnetometers in Fennoscadia is presented
- We identify when and where temporal variations in the radial magnetic field are strongest

Correspondence to:

S. Walker,
simon.walker@uib.no

Citation:

Walker, S., Laundal, K., Reistad, J., Ohma, A., & Hatch, S. (2023). Statistical temporal variations in the auroral electrojet estimated with ground magnetometers in Fennoscandia. *Space Weather*, *21*, e2022SW003305. https://doi.org/10.1029/2022SW003305

Received 29 SEP 2022
Accepted 7 JAN 2023

Author Contributions:

Conceptualization: Simon Walker, Karl Laundal
Data curation: Simon Walker
Formal analysis: Simon Walker
Funding acquisition: Karl Laundal
Methodology: Simon Walker
Project Administration: Karl Laundal
Software: Simon Walker
Supervision: Karl Laundal, Jone Reistad
Validation: Simon Walker
Visualization: Simon Walker
Writing – original draft: Simon Walker
Writing – review & editing: Simon Walker, Karl Laundal, Jone Reistad, Anders Ohma, Spencer Hatch

Abstract We present the implementation of an improved technique to coherently model the high-latitude ionospheric equivalent current. Using a fixed selection of 20 ground magnetometers in Fennoscandia, we present a method based on Spherical Elementary Current Systems (SECS) to model the currents coherently during 2000–2020. Due to the north-south extent of the magnetometers, we focus on the model output along the 105° magnetic meridian. Our improvements involve fixed data locations and SECS analysis grid and using a priori knowledge of the large-scale currents improving the robustness of the inverse problem solution. We account for contributions from ground induced currents assuming so-called mirror currents. This study produces a new data set of divergence-free (DF) currents and magnetic field perturbations along the 105° magnetic meridian with 1-min resolution. By comparing averages of the data set with an empirical model of the ionosphere we demonstrate the validity of the data set. We show how our data set, in particular its temporal nature, is distinct from empirical models and other studies. Not only can the temporal evolution of the DF currents and magnetic field perturbations be investigated, but the time derivative of said quantities can be analyzed. For application in ground induced currents, we present the statistical properties of where (in magnetic latitude and local time) and at what rate ($\partial B_r/\partial t$) the radial magnetic field component fluctuates, a temporal derivative that has received very little attention. We show that $\partial B_r/\partial t$ is dependent on latitude, local time, and solar cycle. We present other applications such as Ultra Low Frequency Waves monitoring.

Plain Language Summary A number of Sun driven processes that can lead to phenomena such as the northern and southern lights, generate electric currents within the ionosphere, an ionized part of the atmosphere. We use a fixed set of ground magnetic field measurements in Fennoscandia to robustly map these currents. Taking advantage of the regularity of the measurements, we not only produce a 20 year time series of the currents and magnetic field but also present statistics of the temporal change of disturbances in the radial magnetic field. This derivative is an important property in understanding the impacts of space weather on modern infrastructure, in particular it can cause large current spikes that disrupt power grids over a relatively large area.

1. Introduction

The link between the Sun and geomagnetic field disturbances has been reported for a long time. In 1852 Sabine identified a link between the number of sunspots, which is an indicator of solar activity, and geomagnetic field disturbances. He found that during a minimum in the sunspot number we experience a reduction in geomagnetic field disturbances (Cliver & Cliver, 1994). Historical reports have shown that for centuries large scale features on the photosphere have coincided with observations of significant, intense geomagnetic activity in the form of low latitude aurora (Schove, 1983), however the mechanisms behind this were not understood. With the arrival of work by Chapman and Birkeland in the late 19th and early 20th century, the description of the Earth's magnetosphere immersed within the solar wind came into focus. Birkeland's early work introduced a current system, which bears his name, flowing in and out of the polar ionosphere. Despite his initial theories involving a stream of high velocity electrons being emitted from the Sun, he moved to the realization of a neutral solar wind made up of both electrons and positively charged ions (Birkeland, 1908; Chapman & Ferraro, 1931). Although a different current system and theory outlined by Chapman prevailed for some time, with the arrival of space based magnetometers Birkeland's theory proved fruitful as it explained the magnetic field perturbations observed (Zmuda et al., 1966). Chapman and Ferraro's work transformed the field of space physics when they described how magnetic storms are manifested through introduction of the magnetosphere and how it interacts with the solar wind (Chapman & Ferraro, 1931; Siscoe, 2001).

In more modern times we know that the solar wind is a quasi-neutral supersonic plasma streaming out of the Sun dragging with it the Sun's magnetic field, due to the frozen-in effect, into interplanetary space. How this interplanetary magnetic field (IMF) couples with the Earth's magnetic field holds particular importance for the dynamics of the polar ionosphere and magnetosphere. This can be described by the Dungey cycle. The Dungey cycle is a generalized, simplified, steady-state description of how, during periods of a southward oriented IMF, dayside geomagnetic flux is opened and reconnected with the IMF before being dragged over the polar cap, subsequently stimulating preexisting open flux in the magnetotail to reconnect. This newly closed flux then convects to the dayside magnetosphere (Dungey, 1961). In the region of the ionosphere, plasma flows are driven by the motion of magnetic flux around the ionosphere. At certain altitudes these plasma flows create a current system due to collisions between ions and neutrals causing a differential motion between the ions and electrons. Currents along the dawn and dusk flanks are referred to as the westward and eastward electrojets respectively. Ground magnetometers have been historically used to study the strength and extent of these electrojets. Such measurements are not affected by the magnetic field of the field aligned Birkeland currents and their associated connecting currents, a realization made by Fukushima and thus has been named Fukushima's theorem. Fukushima's theorem states that under the approximation of a radial magnetic field (which is most valid in the polar regions), the magnetic signature of curl-free (CF) currents, whose source and sink are the Birkeland currents, cancel below the current layer (Fukushima, 1976). Conversely, the magnetic signature of the divergence-free (DF) currents are observable above and below the current layer. Fukushima's theorem shows us why we needed space based magnetometers for Birkeland's theories to be confirmed (Fukushima, 1994; Zmuda et al., 1966). Harang utilized ground based magnetometers to identify a discontinuity between the westward and eastward electrojets (Harang, 1946; Koskinen & Pulkkinen, 1995). This discontinuity commonly coincides with the location of substorm onsets (Weygand et al., 2008), consequently relating the electrojets to the closure of magnetotail flux described in the Dungey cycle.

There is an abundance of ground based magnetometers providing good coverage of measurements of the auroral electrojets, particularly in regions such as North America and Fennoscandia. Spherical harmonic analysis has been a core part of modeling DF ionospheric currents using ground based magnetometers. More recent techniques still have the methodology of Chapman and Bartels (1940) at their core (Laundal et al., 2016, 2018). However, the meaning of the spherical harmonic model output in regions where magnetometer coverage is sparse is often unclear and difficult to interpret. Amm (1997) introduced a technique called spherical elementary current systems which focuses on modeling limited regions. This approach models the DF and CF components of the ionospheric currents on a 2D spherical shell independently using two different spherical elementary currents systems (SECS). Amm and Viljanen (1999) derived the magnetic field from the current a SECS produces. Therefore, we can recreate the magnetic field measured on ground using a weighted sum of DF SECS and consequently find a current that produces those magnetic field perturbations.

In previous studies DF SECS has proven to have a vast array of applications. Weygand et al. (2012) used DF SECS and ground magnetometers to produce estimates of the DF currents and compare them with measurements of convection with SuperDARN. During the summer they show that the DF currents can be used to predict the ionospheric convection, without the necessity of conditions for backscatter that limits the SuperDARN data set. In another study, the SECS amplitudes are compared with measurements of the region 1 and 2 currents using magnetometers on board the DMSP satellites (Weygand & Wing, 2016) and a significant resemblance is found. Many studies of the DF currents have focused on magnetospheric and ionospheric dynamics due to solar wind driving conditions and addressed questions of substorm onset phenomena (Vanhamäki & Juusola, 2020; Weygand et al., 2011, 2021). By placing SECS at both the ionospheric current layer and at a certain depth within the ground, the SECS method has been useful for separating observed magnetic perturbations into telluric and ionospheric sources (Juusola et al., 2020; Pulkkinen, Amm, Viljanen, et al., 2003).

In this study we build upon the DF SECS method and incorporate a new SECS inversion technique introduced by Laundal et al. (2021) for use with data from the Electrojet Zeeman Imaging Explorer (EZIE) mission, which will be launched in 2024. EZIE will be capable of making remote measurements of the magnetic field using the Zeeman effect (Yee et al., 2021). The inversion technique, used by Laundal et al. (2021), involves a priori information about the structure of the electrojet. Here we apply this technique to 20 ground magnetometers in Fennoscandia that were simultaneously available at 1-min resolution for a total of approximately 11 years between 2000 and 2020. The technique produces 2D maps of the electrojet and associated magnetic field, but we focus on an output along a 1D slice along the 105° magnetic meridian, in quasi-dipole co-ordinates, which is particularly

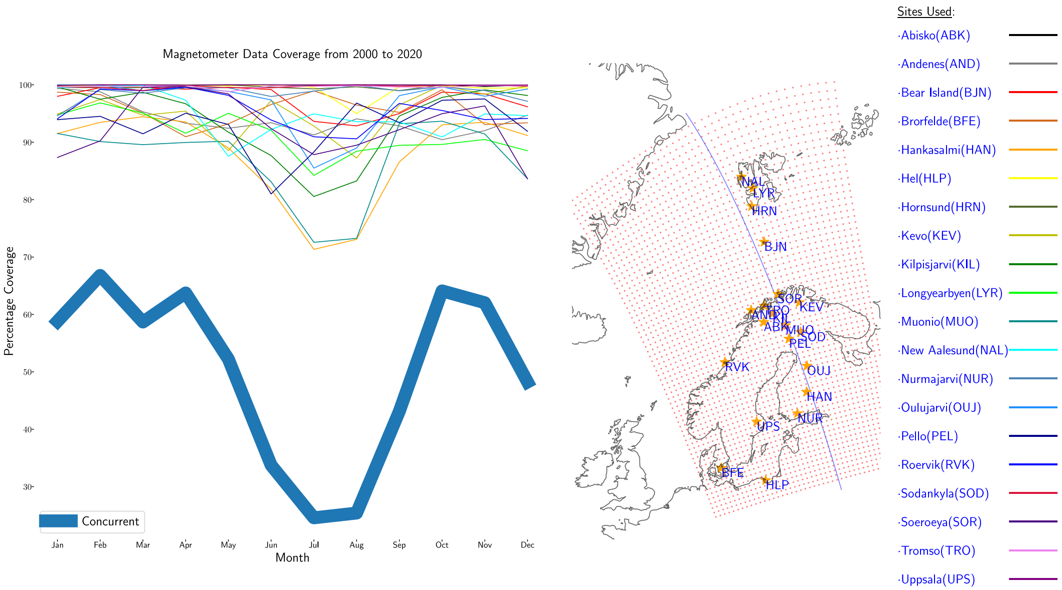

Figure 1. (Left panel) Monthly data coverage of each chosen magnetometer and their availability concurrently. (Right panel) Spherical Elementary Current Systems pole locations as red dots, orange stars to show the location of the magnetometers used in this study and a green line that is the 105° magnetic meridian that the model is evaluated along.

well covered by the magnetometers. The resulting data set, which is publicly available (Walker et al., 2022b), consists of ground magnetic field perturbations and ionospheric sheet current densities along this meridian. We also highlight the interpretation of the time derivative of the radial magnetic field dB_r/dt as the radial component of the curl of the geomagnetically induced electric field (GIE) (Vanhamäki et al., 2013) and present a statistical analysis of the properties of this quantity. This analysis stands in contrast to the analysis of the time derivative of the horizontal magnetic field (often denoted $\partial\mathbf{H}/\partial t$), which has received comparatively much more attention (Dimmock et al., 2020; Juusola et al., 2020; Rogers et al., 2020; Schillings et al., 2022; Tanskanen et al., 2001; Viljanen et al., 2001; Weigel et al., 2003).

In Sections 2 and 3, we respectively present the data and our application of SECS to derive the DF currents. In Section 4 we demonstrate the validity of the approach by comparing the large scale statistics of the DF current and associated radial magnetic field structure with those of an empirical model (Laundal et al., 2018). We also present our statistical analysis of $\partial B_r/\partial t$. In Section 5 we discuss our findings, and in Section 6 we conclude the paper.

2. Data

We use data with 1-min time resolution from 20 magnetometers in Fennoscandia obtained through the SuperMAG collaboration (Gjerloev, 2012), see Figure 1. SuperMAG has its own method of subtracting the baseline of the magnetic field from the magnetometer measurements. As outlined in Gjerloev (2012), there are three core components of the calculated baseline: the diurnal variations, the yearly trend and the remaining residual during quiet periods. The diurnal variations aim to include contributions from the solar quiet (Sq) currents and variations with a local time dependence, such as temperature effects on the instruments. The yearly trend primarily consists of the Earth's time dependent magnetic field. The residual component is determined by the remaining magnetic field during official magnetic quiet periods. It is unlikely that baseline methodology is able to remove all the influences listed, in particular those that vary on shorter time scales, such as the Sq currents, however considering the high latitude of observations we can be confident that their magnetic signature is small in comparison to that of the electrojets.

The SuperMAG data is provided in local magnetic co-ordinates, in which the northward component points along the quiet-day horizontal component of the main magnetic field. This study uses the geodetic co-ordinate system and as such the data needs to be rotated into this system. To rotate the horizontal magnetic field, a declination angle between the local magnetic north and geodetic north is required. We choose to use the CHAOS-7 core and crustal magnetic field model (Finlay et al., 2020) to find the declination angle at each station and rotate the vectors into the geodetic system.

To reduce ambiguity as to what causes variations in the modeled DF currents, we require that all the magnetometers that are chosen for the SECS inversion are available at the same time. Figure 1 shows how often our 20 magnetometers are available individually and simultaneously (thick blue line). This combination of stations has been chosen to maximize the total coverage of simultaneous measurements, approximately 11 years over a period from 2000 to 2020. We find a dip in coverage during the summer months in a number of magnetometers that impacts the overall concurrent coverage. We are also aware that there is little concurrent data in 2015 due to a drop in the availability of data from Hankasalmi and Muonio. Figure 1 also shows the grid that we use in our analysis (discussed in Section 3), and the 105° magnetic meridian, where we evaluate the currents and magnetic field components. We see from the figure that this meridian passes through a high density of magnetometers.

3. Method

In this study we apply a recently developed Spherical Elementary Current System (SECS) inversion technique to ground magnetometers. SECS analysis represents ionospheric and telluric currents as the weighted sum of multiple small-scale currents. The weights are determined from magnetometer measurements. It can thus be used as a way to interpolate magnetic fields and currents from a set of individual non-uniformly distributed magnetometers to a continuous map. Here we give a brief overview of the SECS analysis technique, describe our methodology and highlight how this methodology addresses problems within previous work.

Magnetic fields on ground can be modeled as 2D horizontal DF currents that flow on spherical shells above and/or below the Earth's surface (Chapman & Bartels, 1940). Such modeling has historically been accomplished using spherical harmonic analysis. Amm (1997) presented DF basis functions that are more suitable for regional analyses, which he called SECS. The SECS basis functions are global but with a short reach. Placed sufficiently dense, and scaled appropriately, they can be used to represent any well-behaved 2D vector field on a sphere (Vanhamäki & Juusola, 2020). With these basis functions, a DF surface current density $\vec{J}$ at a radius R can be written as

$$\vec{J}(\vec{r}) = \sum_i \frac{I_i \hat{\vec{e}}_{\phi_i}}{4\pi R} \cot\left(\frac{\theta_i}{2}\right) \tag{1}$$

where $\vec{r}$ is the position where $\vec{J}$ is evaluated. The sum is over a set of DF SECS with amplitudes I_i. θ_i is the angular distance from the SECS to $\vec{r}$, and $\hat{\vec{e}}_{\phi_i}$ is an eastward unit vector in a coordinate system where the SECS is at the pole. In Equation 1 R could be above ground (above R_E, radius of the Earth), for modeling ionospheric currents, or below ground, for modeling telluric currents.

The magnetic field of one single DF SECS was calculated by Amm and Viljanen (1999) through the Biot-Savart law. The analytic expressions for the θ (southward), ϕ (eastward), and r (radial) magnetic fields, in a local system centered on the SECS pole, are:

$$\Delta B_{\theta_i}(\theta_i, r) = \frac{-\mu_0 I_i}{4\pi r \sin\theta_i} \begin{cases} \dfrac{s - \cos\theta_i}{\sqrt{1 + s^2 - 2s\cos\theta_i}} + \cos\theta_i & r < R \\ \dfrac{1 - s\cos\theta_i}{\sqrt{1 + s^2 - 2s\cos\theta_i}} - 1 & r > R \end{cases} \tag{2}$$

$$\Delta B_{\phi_i}(\theta_i, r) = 0 \tag{3}$$

$$\Delta B_r(\theta_i, r) = \frac{\mu_0 I_i}{4\pi r} \begin{cases} \dfrac{1}{\sqrt{1 + s^2 - 2s\cos\theta_i}} - 1 & r < R \\ \dfrac{s}{\sqrt{1 + s^2 - 2s\cos\theta_i}} - s & r > R \end{cases} \tag{4}$$

$$s = \min(r, R)/\max(r, R). \tag{5}$$

In our case, we use magnetometers on ground, so $r = R_E$. However, we model currents both in the ionosphere ($R = R_I > R_E$) and below ground ($R = R_T < R_E$), so both versions of the equations are needed. These expressions are for a single elementary system, and the total magnetic field at $\vec{r}$ is the sum over all. This gives a linear relationship between magnetic field measurements and SECS amplitudes:

$$G\vec{m} = \vec{d}, \tag{6}$$

where $\vec{m}$ is a vector that contains the SECS amplitudes, $\vec{d}$ is a vector that contains all 60 magnetic field components from the 20 magnetometers, and G is a matrix that relates $\vec{m}$ and $\vec{d}$ according to the equations above. We return shortly to how we solve this system of equations for $\vec{m}$.

The grid of SECS can be as dense or as sparse as desired. Although a more dense grid of systems can capture finer structure, two points must be considered: (a) whether the measurements can resolve so fine a structure (for magnetometers one must take into account the spacing of the magnetometers and the smoothing of the magnetic signal with increasing distance from the source (Laundal et al., 2021)); (b) a denser grid requires more model parameters, therefore solving for these parameters becomes more computationally expensive. Furthermore, a number of previous studies have placed the elementary systems in a regular grid in longitude and latitude Vanhamäki and Juusola (2020), Juusola et al. (2006, 2016, 2020). This leads to a more dense grid in physical space at increasing latitudes. We choose to place our elementary current systems above and below the ground in a grid that is regular in cubed sphere coordinates (Ronchi et al., 1996; Sadourny, 1972). The cubed sphere grid is regular in physical space and does not have the same problem. The grid is displayed in the right panel in Figure 1, in a Lambert Conformal projection. The grid has been chosen with an average spacing of 50 km, positioned so that the magnetometers are not within 10 km of a SECS pole and oriented toward approximately magnetic north in magnetic Quasi-Dipole (QD) coordinates (Richmond, 1995), using an epoch of 2008. Furthermore, the radial placement of the elementary systems is an important consideration, as we model the ionospheric and telluric currents as two shells of sheet currents, we must pick an altitude and depth that can mimic the magnetic field created from the 3 dimensional ionospheric and telluric current systems. In total we have $N = 2{,}814$ grid cells, with $2N$ elementary currents, one set above the ground at 110 km altitude, and one set below the ground, where the chosen depth is introduced later in this section. However, a fixed depth for the telluric currents is either more problematic due to the variability in the 3 dimensional ground conductance and the variability in the temporal scales of variations in the ionospheric inducing current which results in the induction peaking at varying depths.

We clearly have many more elementary current systems than data points, which means that the inverse problem of finding the SECS amplitudes from a small set of measurements is severely under-determined. This can be partly rectified by using a simplifying assumption about how the ionospheric currents are related to their induced counterpart in the ground. We choose that the radial magnetic field perturbations from the ionospheric and telluric currents exactly cancel at a 500 km depth (the telluric poles are placed at a depth derived from Equation A5 in Juusola et al. (2016) that depends on the altitude of the ionospheric poles and the cancellation depth). Then, as detailed by Juusola et al. (2016), the mirror current magnitudes are precisely determined by the ionospheric current magnitudes, reducing the number of unknowns from $2N$ to N. This method ascribes the term "image currents" to the currents modeled by the telluric SECS poles. This name comes from the assumption that the telluric currents will mirror the ionospheric currents.

Even with this simplification, the problem remains under-determined; there are an infinite number of SECS amplitude combinations that will fit the observations within some fixed precision. In this section we address the criteria in which we choose the solution to the inverse problem. Most recent studies that use SECS analysis (Amm, 1997; Pulkkinen, Amm, & Viljanen, 2003; Pulkkinen, Amm, Viljanen, et al., 2003; Vanhamäki & Juusola, 2020; Weygand et al., 2021) handle this problem by using truncated singular value decomposition

(TSVD). By zeroing singular values below a certain cutoff, the spatial structure of the DF current is encouraged to be less complex. However, this approach implements very little prior knowledge of DF currents. In contrast, in this study we implement Tikhonov regularization, similar to a recent study by Laundal et al. (2021), who presented a technique for SECS analysis for mesospheric magnetic field data from the upcoming EZIE satellite mission. Using regularization we aim to encourage electrojet like structures, which exhibit small current gradients in the magnetic east-ward direction, and, much like TSVD, encourage reduced current complexity, something we expect due to the distance of the measurements from the source and the need for multiple magnetometers to measure the structure to resolve it. Following Laundal et al. (2021)'s approach, we find the set of SECS amplitudes, $\vec{m}$, that minimizes:

$$f = \|G\vec{m} - \vec{d}\|^2 + \lambda_1 \|I\vec{m}\|^2 + \lambda_2 \|L_e\vec{m}\|^2, \tag{7}$$

where I is the $N \times N$ identity matrix, and L_e is an $N \times N$ matrix that, when multiplied by $\vec{m}$, yields the gradient of the SECS amplitudes in the QD eastward direction. The first term in Equation 7 is the sum of squared errors. If we only minimized this term, $\vec{m}$ would be the least squares solution. The second term represents the squared length of the model vector, multiplied by the parameter λ_1. Increasing λ_1 will limit the overall magnitude of the components in the solution vector, effectively decreasing the spatial complexity of the solution. Increasing λ_1 has a similar effect as increasing the cutoff value in a TSVD inversion. The third term in Equation 7 describes the sum of the squared magnitudes of the magnetic eastward gradients in the SECS amplitude, scaled by λ_2. Increasing λ_2 limits the eastward gradients. The rationale for including this term is that ionospheric electrodynamics tends to be structured east-west (Harang, 1946).

Since the location of our magnetometers and SECS poles are fixed, we choose a constant set of values for λ_1 and λ_2. If λ_1 is too much larger than λ_2 the amplitudes no longer have a smooth gradient in the magnetic east-west direction. If λ_2 is too much larger than λ_1 the amplitudes become thin bands in the east-west direction because there is no restriction in the variation in the north-south direction. Furthermore, even if the λ values are well balanced, if both are too large the model will not represent the data because the first term (the data-model misfit) will not be significant enough. With these things in mind, and after inspecting a great number of cases, we chose $\lambda_1 = 10^{-23}$ and $\lambda_2 = 10^{-21}$. These numbers are based on the use of SI units. Since the magnetometer locations, SECS locations, and regularization parameters are all fixed, our inversion results are directly comparable across the whole data set.

3.1. Examples

Figures 2 and 3 show two examples where the technique described above was applied. The left panels show the magnetic field on the ground, where the background color represents the modeled radial magnetic field perturbations, and black the arrows represent the modeled horizontal component. The orange stars show the locations of the magnetometers. The red arrows represent the measured horizontal magnetic field and the colored dot in the center of the star the radial component. The second panels from the left shows the SECS pole amplitudes in color. In the third panels, the arrows represent the modeled ionospheric currents and the color its magnitude. The final panel shows a slice of the ionospheric currents along the 105° magnetic meridian, which is particularly well covered by data. The publicly available data set, Walker et al. (2022b), includes the ground magnetic field and equivalent current along this meridian, with spacing ≈70 km.

With Equation 1, the DF current can be calculated at, in principle, any location. However, very close to a SECS pole, the magnitude approaches infinity. Therefore, we follow Vanhamäki and Juusola (2020) and introduce a correction (see their Equation 2.44) closer than 50 km from the SECS poles. This correction is only applied when evaluating the DF current, and not to the magnetic field, which is not as severely affected by the singularity due to the distance between the currents and the ground.

Figure 2 is based on 1 min of data taken at 22:34 UT on the 5th of February 2000. By looking at the left panel, we see that the model and the measurements are in good agreement. The second panel clearly shows that the SECS amplitudes have small gradients in the east-west direction and shows large areas of similar amplitude. This is a clear case of a strong east-west electrojet. Figure 3 shows another example, based on 1 min of magnetometer data at 20:25 UT on the same day. Again, the model and the measurements are in good agreement. Here, on the other hand, we see a strong northward current. This shows that the λ values in Equation 7 are not so large as to prevent north-south structures when the data indicates that such structures exist.

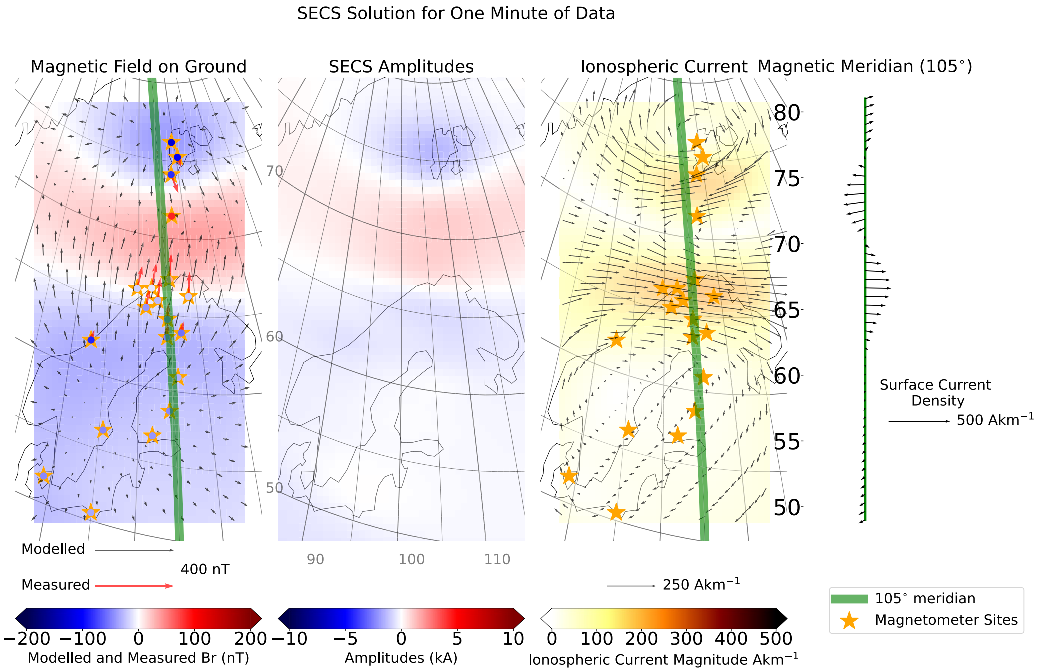

Figure 2. The figure shows the application of the methodology described in Section 3 where the currents and magnetic field are estimated by fitting Spherical Elementary Current Systems (SECS) amplitudes using magnetic field measurements. The left panel shows the estimated horizontal magnetic field as black arrows, the estimated radial magnetic field as the background color, the location of the magnetometers as orange stars, the measured horizontal magnetic field as red arrows and measured radial magnetic as colored dot in the center of the stars. The second panel from the left shows the SECS pole amplitudes as the background color. The third panel from the left shows the estimated divergence-free currents as black arrows and the magnitude of the currents with the background color. The third panel from the left also shows the location of the magnetometers as orange stars. The right panel shows the estimated divergence-free currents along the 105° magnetic meridian, at different magnetic latitudes, as black arrows. The location and extent of the 105° magnetic meridian, where the model is evaluated for every minute of data, is shown as a green line in the first panel and third panel from left. The time in UTC of the magnetometer data used for this inversion is 22:34 05/02/2000.

With the methodology tested through the use of case studies, we apply it to every instance where SuperMAG provides data from all 20 magnetometers. At each instance we calculate an independent set of model amplitudes and use them to estimate the DF currents in the ionosphere and the ground magnetic field along the 105° magnetic meridian. The resulting data set is N_t independent instances of currents and magnetic fields at 50 points, evenly spaced, between 49° and 81° mlat, where N_t is the total number of minutes where data from all 20 magnetometers has been provided.

4. Results

We now present results based on our data set, minute-cadence magnetic field perturbations and associated eastward and northward sheet current density along the 105° QD meridian. First we compare the currents and radial magnetic field from an empirical model to a large-scale average based on our data set. This comparison is used as validation. The data set's relatively high time resolution enables investigation of spatiotemporal structures in a way that is not possible with empirical large-scale, average models. We therefore subsequently present an analysis of the temporal changes in the radial magnetic field ($\partial B_r/\partial t$).

4.1. Large-Scale Average Current Structure

Here we compare a large-scale average current and radial magnetic field pattern to predictions from the Average Magnetic field and Polar current System (AMPS) model. The AMPS model (Laundal & Toresen, 2018; Laundal

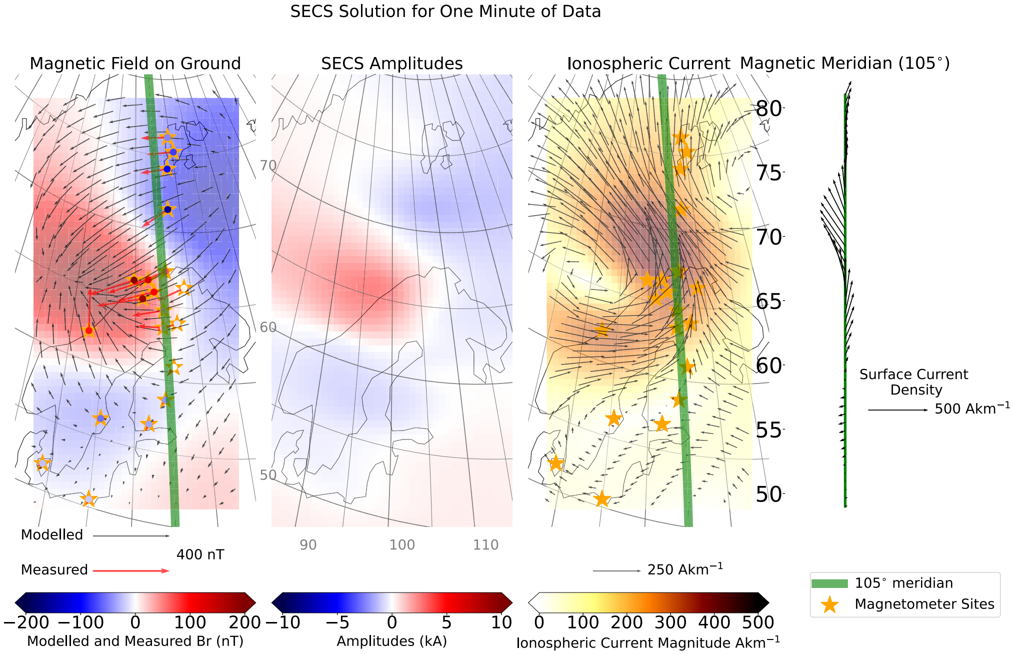

Figure 3. This figure uses the same set up as Figure 2. The time in UTC of the magnetometer data used for this inversion is 20:25 05/02/2000.

et al., 2018) is an empirical model of the ionospheric magnetic field and current system generated using magnetic field measurements from *Swarm* and the Challenging Minisatellite Payload (CHAMP) satellites. AMPS takes user inputs of solar F10.7 cm flux, solar wind speed, IMF B_y and B_z, and the Earth's dipole tilt.

To compare our data set to AMPS prediction it is important to make a selection of our data set that is restrictive enough for the average to be a good general description of the range of data within that selection, while having enough data to produce a reliable average. We have tested a variety of selections but for the purpose of paper we present three clock angles, −135°, 180°, and 135°. For each angle we select instances when the IMF clock angle is within a 45° wide window centered at that clock angle. To reduce the effects of extreme events and produce the typical electrodynamics expected from the Dungey cycle (i.e., the two cell convection pattern) we select our electrojet and radial magnetic field estimates when they occur during the following conditions: IMF B_y is between −10 and 10 nT, IMF B_z is between 0 and −10 nT, and the dipole tilt angle is less than 0°. Further measures are taken to ensure that the data selected is under the influence of these conditions by using a similar approach to Haaland et al. (2007): We apply a 30-min rolling average to OMNI data (King & Papitashvili, 2005), that is time shifted to the bow shock, and associate it with our data set by having the average made up of OMNI data 20 min prior and 10 min after the SECS meridian was evaluated. Furthermore, we calculate the circular variance of IMF B_y and B_z in the same windows as a measure of how stable the conditions are. We then add a further selection criteria that the circular variance associated with our data set must be less than 0.04.

Figure 4 (top row) shows the average horizontal sheet current and radial magnetic field based on this data selection, on a grid of magnetic latitude and local time. A corresponding AMPS prediction is shown on the bottom row, using the median conditions of the solar wind, IMF, solar flux and dipole tilt of the times selected to make the SECS based map. Figure 4 shows that the general shape of the radial magnetic field perturbations and electrojet are similar in the two approaches. This demonstrates that the technique produces results that are consistent with expectations from earlier studies. However, in Figure 4 there are some notable differences between the two plots particularly in terms of the magnitude of the currents and the radial magnetic field. We also see a difference in the shape and location of the cells of the radial magnetic field that are most prominent at higher latitudes. One

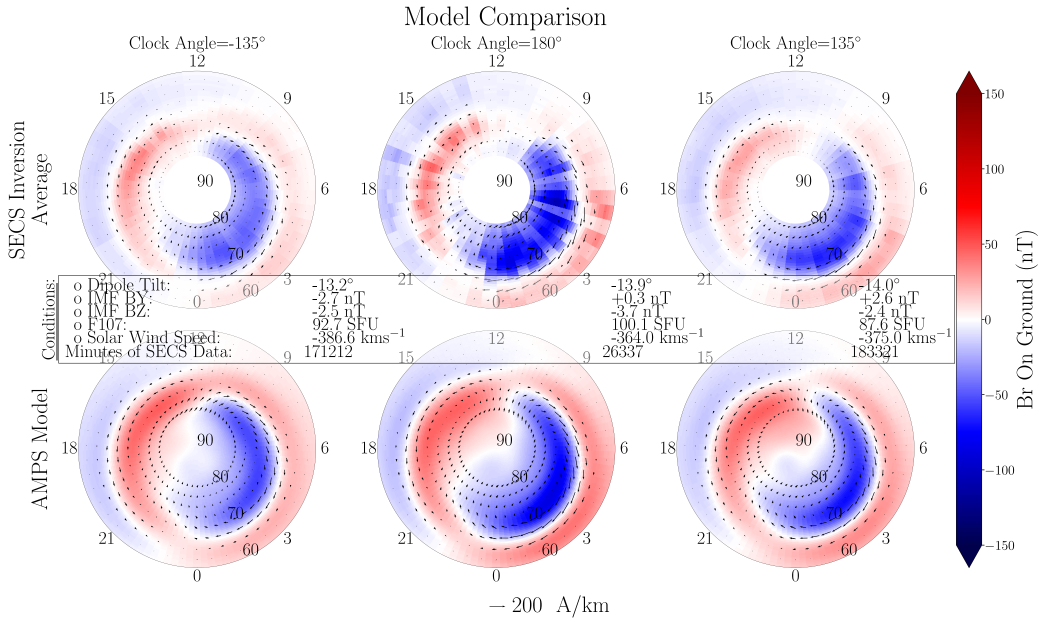

Figure 4. The figure shows three plots containing an average of each instance of the Spherical Elementary Current Systems (SECS) model output along the 105° meridian, that occur under different criteria, and three plots with a corresponding output from the Average Magnetic field and Polar current System (AMPS) model. The top row shows a polar view of the average divergence-free sheet current density in the ionosphere and radial magnetic field perturbations on the ground, modeled along the 105° meridian for each minute of simultaneous measurements from all 20 magnetometers, occurring under the range of conditions specified in Section 4.1 and have a clock angle that is within a window centered at −135°, 180°, and 135° respectively and with a width of 45°. The bottom row shows a polar view of the divergence-free sheet current density and radial magnetic field output from the AMPS model when run with each set of the conditions specified in the conditions box, which are the median conditions for the selected instances of each of the SECS model outputs.

difference between the two approaches is that the AMPS current by definition is DF, while our average current pattern in general is not. Our technique enforces DF currents at any given time, but averages composed of several meridians do not have this constraint. We reiterate that the main advantage of our approach over average models is that it allows analyses of spatio-temporal variations. We explore this further in the rest of this section.

4.2. Occurrence Rate of Large Magnetic Field Variations

Temporal variations in the radial component of the magnetic field ($\partial B_r/\partial t$) are equivalent to the radial component of the curl of the purely induced (DF) electric field, otherwise known as the GIE (Vanhamäki et al., 2013). The large amount of data (11 years' worth of 1-min data, spanning 20 years), and the consistency in the technique makes our data set ideal for analyzing how GIEs in Fennoscandia vary in relation to other parameters. This is also important for space weather applications, since variations in the magnetic field cause ground induced currents (GICs), which have negative consequences for human infrastructure, such as the electrical power grid (Albertson et al., 1993; Molinski, 2002; Oliveira & Ngwira, 2017).

Figure 5 shows the likelihood of observing temporal variations of the radial magnetic field perturbations (or equivalently, the radial component of the curl of GIEs), the difference in the radial magnetic field between two instances along the 105° meridian separated by 1 min, above a certain magnitude for the entire data set produced but excluding instances with a gap greater than 1 min. The y axis shows the magnetic latitude, and the x axis shows the threshold for a positive detection. Negative x corresponds to decreases in B_r and positive x corresponds to increases. The color and contours show the number of occurrences divided by the number of observations. The occurrence is presented in a logarithmic style where $10^{-5.7}$ is an occurrence of once per year. The figure is approximately symmetrical suggesting that large increases and large decreases are just as common at similar latitudes. Two peaks, identified by red ellipses in Figure 5, stand out, the first occurs at approximately 67° latitude,

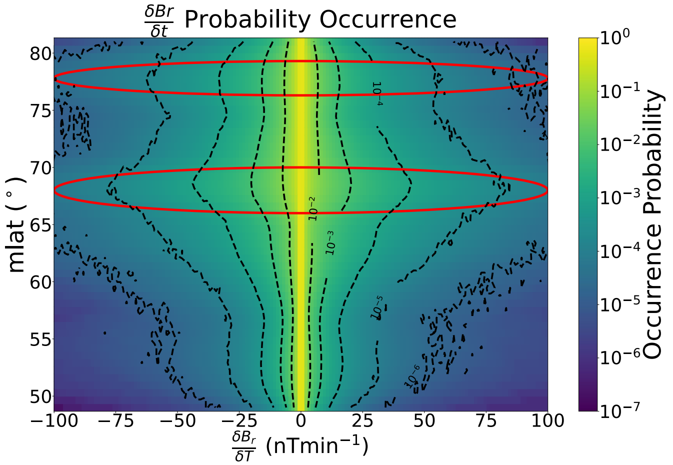

Figure 5. A plot of the statistics of fluctuations of the radial component of the magnetic field evaluated on the ground along the 105° mlon meridian. The contours and color are the cumulative probability of getting increases (decreases) in B_r that are at least the fluctuation indicated on the positive (negative) part of the x axis. Red ellipses highlight the two main peaks in the occurrence of a large derivative of B_r.

close to the northern most coast of Norway, and the second at approximately 77° latitude, close to Ny-Ålesund. The larger of the two is near the average latitude of substorm disturbances and the location of the electrojets. The smaller of the two may be related to high latitude return currents. Explanations for the double peak are explored further in Section 5.2.

Figure 6 shows the occurrence probability of large fluctuations as a function of magnetic local time and magnetic latitude for the entire data set produced but excluding instances with a gap greater than 1 min. We choose to regard fluctuations greater than 25 nT min^{-1} as large based on Figure 5. We see two peaks, the largest again at approximately 67° latitude, close to the northern coast of Norway, and the second at approximately 77° latitude, near to Ny–Ålesund. The strongest peak forms a smooth circle at similar latitudes for all MLTs, however, exhibiting higher occurrence probability in the pre-midnight sector. This is the typical location for substorm onsets (Frey et al., 2004). The high latitude peak is strongest in the pre-midnight and pre-noon regions. The pre-midnight high-latitude peak may also be associated with substorms. We discuss the occurrence probability distribution in greater detail in Section 5.2 and pay particular focus to the mechanisms that may be the cause of the pre-noon high latitude peak.

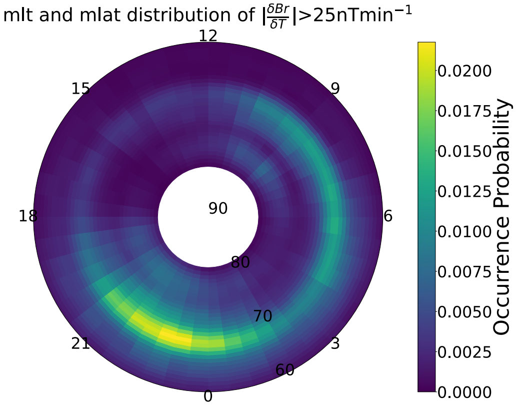

Figure 6. Figure showing the probability of a fluctuation of a radial magnetic field perturbation of magnitude greater than 25 nT/min. The figure is in mlt-mlat space where the color represents the occurrence probability.

Figure 7 shows how the probability of large fluctuations in the radial magnetic field perturbation varies over the solar cycle. The occurrence probability is calculated by finding the meridians that have $\delta B_r/\delta t$ greater than 25 nT/min at any latitude. The occurrence probability shows an approximate 3 year offset with the peak in sunspot number and peaks during the declining phase. This is the same behavior recorded in the solar wind velocity. This observation is in agreement with current literature where both wave phenomena and substorm occurrence statistics show a correlation with solar wind velocity (Dimmock et al., 2016; Hynönen et al., 2020; Newell et al., 2016; Nosé et al., 1995; Nykyri et al., 2017; Tanskanen et al., 2005).

5. Discussion

We have presented a technique to derive magnetic fields and equivalent currents along the 105° magnetic meridian, based on measurements from 20

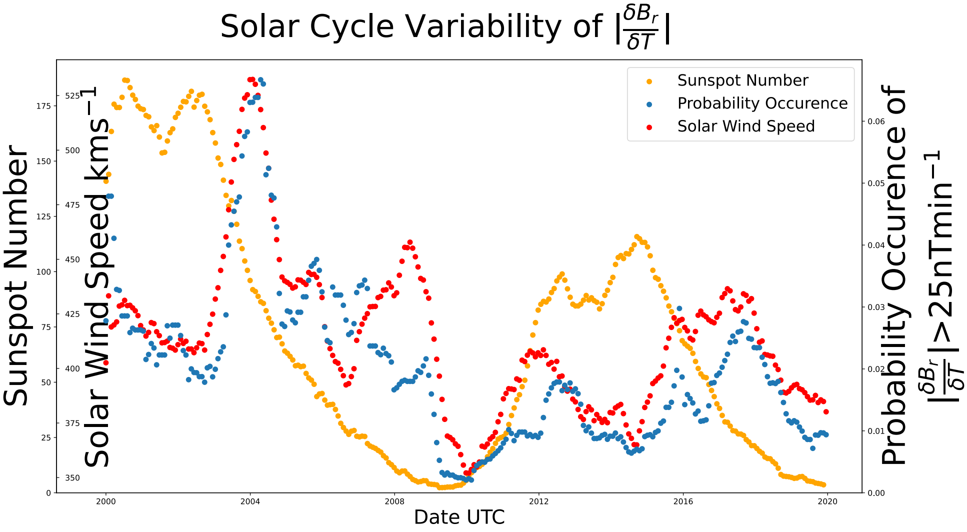

Figure 7. Figure showing the sunspot number, the solar wind speed, and the probability of observing fluctuations in B_r greater than 25 nT/min anywhere along the meridian. The quantities are first grouped into 27 days (one Carrington rotation), taking the mean, and then a 365 day window rolling mean is applied to remove relatively short time scale fluctuations.

magnetometers in Fennoscandia. Currents and magnetic field perturbations along this meridian are released in accompaniment with the paper (Walker et al., 2022b). The data set is not without limitations due to the decisions made in magnetometer choice, SECS grid choice and methodology. The temporal coverage of the magnetometers has a bias toward winter months and their spatial distribution impacts the scale size of currents that can be resolved, which we describe in Section 2 and discuss further in Section 5.4. The varying ground conductivity over the region, in particular between ground and sea water, can cause a bias in the magnetic field perturbations at a magnetometer and is another aspect of the impacts of choice of magnetometers. We discuss and explore impacts of this on the data set later in Section 5.2. As we discussed in Section 3, the ionospheric and telluric currents are simplified as two dimensional shells and the radial placement of these shells and the coverage of the grid limits its ability to create suitable current structures that are representative of the magnetic perturbations from the three dimensional DF currents. Different values for the regularization parameters, λ_1 and λ_2, that are chosen in Section 3 could yield different data set. Although repetition of the steps taken to reach said parameters, in particular by different users, may yield different values, the differences are likely small, if the criteria in Section 3 are met, and, therefore, will have little impact on the data set. Of course different regularization schemes, such as one in the temporal domain, will have implications on the data set produced and we return to the discussion of methodology development in further studies section, Section 5.4.

5.1. Relevance of the New Data Set and Technique

In this section we summarize the data set and the model introduced. We discuss the advantages of the approach used and the avenues of research where the data set can contribute.

A comparable study is Aakjær et al. (2016) that utilizes the magnetometers on board the European Space Agency's *Swarm* satellites. By using a similar approach to Olsen (1996), the auroral electrojet is modeled for each pass of a *Swarm* satellite by fitting a series of line currents orthogonal to the satellite track using the measured magnetic field magnitude. The use of satellites in Aakjær et al. (2016) has the advantage that they cover regions inaccessible to ground magnetometers. However, the *Swarm* satellites orbit above ≈450 km which means that their distance from the ionospheric current layer will limit the resolvable electrojet structure, compared to what can be achieved with a dense ground network. The constant location of measurements, the longevity of magnetometer operation and constant high latitude observations enables a much larger data set bringing greater confidence to the statistics produced and the ability to tackle temporal phenomena.

Compared to previous SECS based analyses of ground-based magnetometer measurements (Marsal et al., 2017; Vanhamäki et al., 2003; Weygand & Wing, 2016; Weygand et al., 2011, 2012), the present study is distinct in a number of ways: We keep a constant selection of ground magnetometers and SECS poles, thus keeping a constant model geometry, which allows us to produce a consistent data set that spans 20 years. This enables the study of long-term temporal variations and structures in the magnetic field, as demonstrated in Section 4.1. Also our application of Tikhonov regularization to solve the SECS inverse problem, in particular the use of first order Tikhonov regularization, is different to the more commonly applied, TSVD since it implies knowledge of electrojet structure to encourage solutions that are aligned in the magnetic east-west direction unless the data indicates otherwise.

In this study we use the regularization approach introduced by Laundal et al. (2021) for the application to the EZIE satellites that are planned for launch in 2024. EZIE will remotely detect the magnetic field at ≈80 km altitude using the Zeeman effect (Yee et al., 2021). At this altitude the influence of telluric currents is negligible. The high density of measurements and their vicinity to the electrojet will allow EZIE to resolve fine structures in the electrojets. One application of EZIE, as a continuation of this and other studies, is to utilize two layers of measurements (EZIE and ground magnetometers) to improve the separation of magnetic fields from telluric and ionospheric currents. Combining EZIE measurements at 80 km altitude with both ground and low Earth orbit measurements of magnetic perturbations will allow for further investigation of large and small scale features with unprecedented 3D coverage.

There are many avenues to developing this technique further. First, the methodology by Juusola et al. (2020) can be used to improve upon the approach used to account for the influence of telluric currents, thus modeling the ionospheric currents more accurately. Second, much like Green et al. (2007) did with spherical cap harmonics, we can use a combination of ground and satellite measurements of the magnetic field to constrain a superposition of DF and CF SECS (Amm, 1997; Amm & Viljanen, 1999). This allows us to take advantage of a regional approach to estimate currents with finer structure than is achieved by the Active Magnetosphere and Planetary Response Experiment (AMPERE) (Anderson et al., 2014). Furthermore, we can now use shorter data windows than Green et al. (2007). We can then analyze the ionospheric currents at time scales closer to substorm dynamics. Unlike other studies (Laundal et al., 2022) we will estimate the ionospheric currents based only on the magnetic field data, without further knowledge of the ionospheric state.

5.2. $\partial B_r/\partial t$

Figures 5 and 6 show that there are two clear peaks in the probability of large temporal variations in B_r, one at auroral latitudes and one at higher latitudes. There are several possible explanations for the latitudinal distribution of the occurrence of large fluctuations in the radial magnetic field: The density of magnetometers is necessarily smaller in the ocean region between northern Norway and Svalbard, with a single magnetometer at Bjørnøya. This may increase the relative importance of the damping terms in our cost function (Equation 7), leading to a smaller B_r and thus smaller $\partial B_r/\partial t$. Another explanation is that the peak coincides with the peak in the latitudinal distribution of electrojets.

An alternative geological explanation for the double peak is that the difference between the high conducting sea water and less conductive ground around coastal magnetometers leads to an enhanced radial magnetic field from the induced currents, as discussed by Juusola et al. (2020). The method that we use to take into account ground-induced currents is incapable of accounting for this effect of varying conductivity. While this does not affect our estimates of the magnetic field it will affect our estimates of the DF ionospheric current. A repeat of this study on magnetometers in other regions may allow us to eliminate the effects of geography in the model by comparing the occurrence distributions from the different data sets. Improved techniques in accounting for the influence of telluric currents, such as that presented by Juusola et al. (2020), can be used in future research to perform a better separation of the ionospheric and telluric contributions to the magnetometer measurements. In any case, improving our model of the telluric currents is not likely to have any influence on the results shown in Figures 5–7 as we are fitting B_r, and either approach will be a similar interpolation of the measurements of the radial magnetic field perturbation.

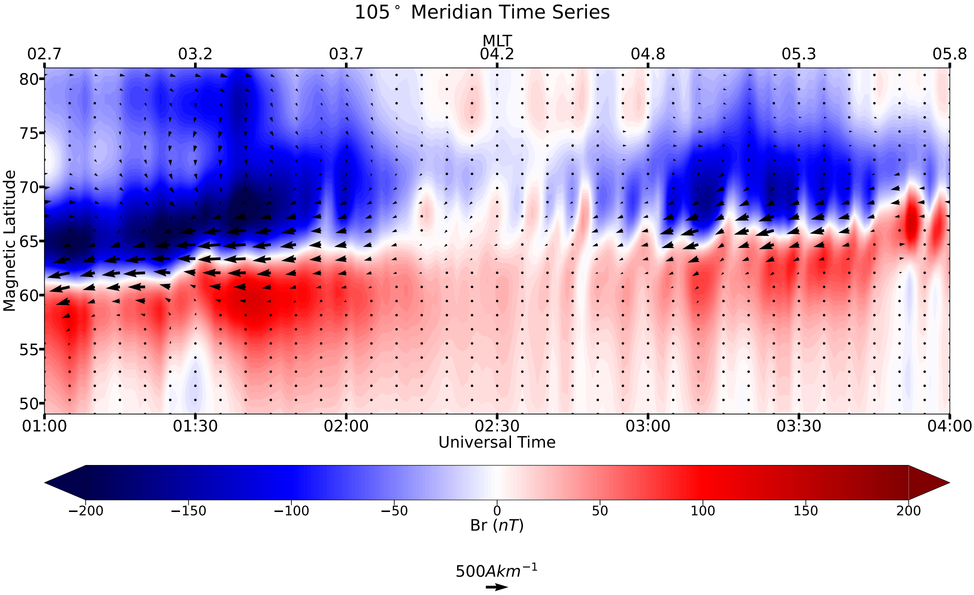

Figure 8. Time series of the data set with sheet current density vectors reduced to a cadence of 5 min and 25 data points along the meridian. The data is from the morning sector on the 28th of January 2000.

While the latitudinal distribution, in Figures 5 and 6, may be influenced by geological effects unique to our data set (i.e., the local effect of the coastline), the MLT distribution, in Figure 6, is less affected. Therefore the MLT distribution and latitudinal distribution, excluding the region between the Norwegian coast and Svalbard, can be interpreted in terms of ionospheric dynamics. Figure 6 shows that there is a peak in the occurrence of large $\partial B_r/\partial t$ at the common location of substorm onsets, 23 hr MLT, with a second peak at high latitudes at around 9 hr MLT. We also observe but have not presented that the time derivative of the horizontal magnetic field, as reported by Viljanen et al. (2001), evinces a similar MLT and MLAT distribution. In Figure 6 we also see a peak in the occurrence probability at high latitudes in the pre-noon sector. This peak may be associated with the current driven by a rapid solar wind pressure increase as described by Madelaire et al. (2022). This hypothesis can be addressed in future work by reproducing these statistics under common favorable conditions, such as a northward orientated IMF, to see if the features in the statistics become enhanced. Another theory is that the peak is related to a high occurrence of ULF waves. Conditions are known to be favorable for ULF waves in the solar wind on the dawn side of the magnetosphere (Plaschke et al., 2018). Nosé et al. (1995) identified a distribution in ULF waves, from the magnetometer on-board Dynamics Explorer 1, that also peaks pre-noon at a high latitude. Furthermore, Weigel et al. (2003) investigated the time derivative of the horizontal magnetic field and found the occurrence of strong $\delta H/\delta t$ at a similar location, attributing this peak to the influence of ULF waves. Section 5.3 shows that the SECS methodology implemented in this study does reproduce waves and can be used to investigate such phenomena. The hypothesis, in regards to the distribution of ULF waves, can be addressed in future work by analyzing the periodicity of these fluctuations and their contribution to the presented statistics.

5.3. ULF Wave Visualization

Figure 8 shows an example of the magnetic field and DF current at the 105° meridian as a function of time and MLT. The color shows the radial magnetic field on ground, including both ionospheric and internal contributions. The vectors show the equivalent current corresponding to the ionospheric contribution to the observed magnetic field. The figure was produced by stacking vertical latitudinal profiles horizontally. The lower x-axis shows the universal time, and the top x-axis shows the magnetic local time of the 105° meridian. This "magnetic field keogram" shows how the electrojet can change over time and how the zero point of the radial magnetic field perturbations tracks the center of the electrojet.

Figure 8 shows clear evidence of ULF waves in periodic fluctuations of the radial magnetic field perturbations. This is most clearly seen between 2:10 and 3:00 universal time (UT). The figure illustrates that the 1-min resolution magnetic field model, evaluated along the 105° meridian allows easy visual identification of waves, and wave characteristics such as amplitude, phase and frequency. An investigation into the occurrence and magnitude of ULF waves could help test the hypothesis presented in Section 4.2, that the pre-noon high latitude peak may be explained by such phenomena.

5.4. Future Studies

The technique presented here is also applicable with other data sets. A number of magnetometers have higher cadence measurements than are used in this study. The IMAGE chain has a 10-s cadence for all their magnetometers, some even have 1-s cadence. Using these magnetometers, this study could be repeated and higher frequency waves in the magnetic field evaluated along the meridian could be resolved. Furthermore, we show that in Section 2 and Figure 1 that there is a seasonal bias in our data set due to the availability of some magnetometers selected, a selection of magnetometers could be made with the reduction of data availability bias in mind rather than to maximize the overall data, as was done in this study. Additionally, as stated previously, the methodology could be applied to different regions and the study repeated. For example, North America has great coverage on magnetometers; performing a similar study using those magnetometers could allow us to verify or refute the geological hypotheses surrounding the peaks in the latitudinal distribution of the occurrence of large $\partial B_r/\partial t$. The study can also be repeated for conjugate chains of magnetometers, such as those in Greenland and Antarctica, to investigate inter-hemispheric differences. Finally, the inversion methodology could have additional regularization parameters, where further expectations could be imposed on the electrojet structure, for example, a temporal regularization parameter could be used to imply a degree of smoothness in the evolution of the electrojet structure. However, in this case one must consider the impact on the validity of the derivative statistics investigated in this study.

6. Conclusions

We have presented a new technique for the application of DF SECS and applied it to 20 ground magnetometers in Fennoscandia. This has yielded a new data set of DF currents along the 105° magnetic meridian covering the period of 2000–2020, with the total amount of data being 11 years at 1-min cadence. The data set is publicly available (Walker et al., 2022b). It has been demonstrated that large scale average patterns of this data set follow expected behavior. Furthermore, the ability to represent the large scale currents, and their magnetic perturbation on ground is advantageous for interpreting the magnetospheric sources of the changes in the magnetic field on ground. This new data set sets itself apart from empirical models with its temporal nature. Consequently, we have investigated the temporal and spatial variations in the auroral electrojets and the radial magnetic field. We also take advantage of the ability to derive the temporal derivatives by presenting and investigating the time derivative of the radial magnetic field, which has seen little attention in comparison to the horizontal component. The occurrence of stronger time derivatives of the radial magnetic field is shown to have peaks in magnetic latitude, at approximately 67 and 77 magnetic latitude, and the occurrence of a time derivative greater than 25 nT is shown to have peak locations in magnetic local time and magnetic latitude. We suggest that the latitudinal distribution is due to a common latitude of the electrojets or because of the distribution of the magnetometers or due to conductivity effects on coastal magnetometers. We attribute pre midnight peaks in the occurrence of time derivatives greater than 25 nT to the occurrence of substorm onsets and the high latitude peak centered on 9 MLT we suggest is due to PC5 waves, of which our data set is well suited to investigate, or current vortices.

Data Availability Statement

The code for producing Figures 4–6 and Figure 8 is available at Walker et al. (2022a). The data set of divergence-free currents and ground magnetic field perturbations created in this study is publicly available at Walker et al. (2022b). The ground magnetometer data has been retrieved from the SuperMAG collaboration: https://supermag.jhuapl.edu/mag, where data from all stations were downloaded as yearly files, in June 2020 and has data revision number 5. The solar wind and interplanetary magnetic field measurements has been downloaded from the OMNI database: https://cdaweb.gsfc.nasa.gov/sp_phys/data/omni/hro_1min/. The sunspot number has been retrieved from SILSO: https://www.sidc.be/silso/datafiles.

Acknowledgments
This work was supported by Research Council of Norway under contracts 223252/F50 and 300844/F50 and by the Trond Mohn Foundation. For the ground magnetometer data we thank the institutes who maintain the IMAGE Magnetometer Array: Tromsø Geophysical Observatory of UiT the Arctic University of Norway (Norway), Finnish Meteorological Institute (Finland), Institute of Geophysics Polish Academy of Sciences (Poland), GFZ German Research Centre for Geosciences (Germany), Geological Survey of Sweden (Sweden), Swedish Institute of Space Physics (Sweden), Sodankylä Geophysical Observatory of the University of Oulu (Finland), Polar Geophysical Institute (Russia), and DTU Technical University of Denmark (Denmark). For the processing, baseline removal and distribution of the ground magnetometer data we acknowledge: SuperMAG, PI Jesper W. Gjerloev. For the sunspot number we acknowledge: The World Data Center SILSO, Royal Observatory of Belgium, Brussels. We extend our gratitude to the members of the Understanding Mesoscale Ionospheric Electrodynamics Using Regional Data Assimilation team for the discussions and insight into the topic of study. We also thank the International Space Science Institute in Bern, Switzerland for hosting the team.

References

Aakjær, C. D., Olsen, N., & Finlay, C. C. (2016). Determining polar ionospheric electrojet currents from Swarm satellite constellation magnetic data. *Earth Planets and Space*, *68*(1), 1–14. https://doi.org/10.1186/s40623-016-0509-y

Albertson, V. D., Bozoki, B., Feero, W. E., Kappenman, J. G., Larsen, E. V., Nordell, D. E., et al. (1993). Geomagnetic disturbance effects on power systems. *IEEE Transactions on Power Delivery*, *8*(3), 1206–1216. https://doi.org/10.1109/61.252646

Amm, O. (1997). Ionospheric elementary current systems in spherical coordinates and their application, technical report no. 7 (Vol. *49*). https://doi.org/10.5636/jgg.49.947

Amm, O., & Viljanen, A. (1999). Ionospheric disturbance magnetic field continuation from the ground to the ionosphere using spherical elementary current systems. *Earth Planets and Space*, *51*(6), 431–440. https://doi.org/10.1186/BF03352247

Anderson, B. J., Korth, H., Waters, C. L., Green, D. L., Merkin, V. G., Barnes, R. J., & Dyrud, L. P. (2014). Development of large-scale Birkeland currents determined from the active magnetosphere and planetary electrodynamics response experiment. *Geophysical Research Letters*, *41*(9), 3017–3025. https://doi.org/10.1002/2014GL059941

Birkeland, K. (1908). *The Norwegian aurora polaris expedition, 1902–1903*. H. Aschelhoug. https://doi.org/10.5962/bhl.title.17857

Chapman, S., & Bartels, J. (1940). Geomagnetism, volume II: Analysis of the data, and physical theories.

Chapman, S., & Ferraro, V. C. A. (1931). A new theory of magnetic storms. *Terrestrial Magnetism and Atmospheric Electricity*, *36*(2), 77–97. https://doi.org/10.1029/TE036i002p00077

Cliver, W., & Cliver, E. W. (1994). Solar activity and geomagnetic storms: The first 40 years. *EOS Transactions*, *75*(49), 569–575. https://doi.org/10.1029/94EO02041

Dimmock, A. P., Nykyri, K., Osmane, A., & Pulkkinen, T. I. (2016). Statistical mapping of ULF Pc3 velocity fluctuations in the Earth's dayside magnetosheath as a function of solar wind conditions. *Advances in Space Research*, *58*(2), 196–207. https://doi.org/10.1016/j.asr.2015.09.039

Dimmock, A. P., Rosenqvist, L., Welling, D. T., Viljanen, A., Honkonen, I., Boynton, R. J., & Yordanova, E. (2020). On the regional variability of dB/dt and its significance to GIC. *Space Weather*, *18*(8), e2020SW002497. https://doi.org/10.1029/2020SW002497

Dungey, J. W. (1961). Interplanetary magnetic field and the auroral zones. *Physical Review Letters*, *6*(2), 47–48. https://doi.org/10.1103/PhysRevLett.6.47

Finlay, C. C., Kloss, C., Olsen, N., Hammer, M. D., Tøffner-Clausen, L., Grayver, A., & Kuvshinov, A. (2020). The CHAOS-7 geomagnetic field model and observed changes in the South Atlantic Anomaly. *Earth Planets and Space*, *72*(1), 1–31. https://doi.org/10.1186/s40623-020-01252-9

Frey, H. U., Mende, S. B., Angelopoulos, V., & Donovan, E. F. (2004). Substorm onset observations by IMAGE-FUV. *Journal of Geophysical Research*, *109*(A10), A10304. https://doi.org/10.1029/2004JA010607

Fukushima, N. (1976). Generalized theorem for no ground magnetic effect of vertical currents connected with Pedersen currents in the uniform-conductivity ionosphere. *Report of Ionosphere and Space Research in Japan*, *30*(1–2), 35–40.

Fukushima, N. (1994). Some topics and historical episodes in geomagnetism and aeronomy. *Journal of Geophysical Research*, *99*(A10), 19113. https://doi.org/10.1029/94ja00102

Gjerloev, J. W. (2012). The SuperMAG data processing technique. *Journal of Geophysical Research*, *117*(9), A09213. https://doi.org/10.1029/2012JA017683

Green, D. L., Waters, C. L., Korth, H., Anderson, B. J., Ridley, A. J., & Barnes, R. J. (2007). Technique: Large-scale ionospheric conductance estimated from combined satellite and ground-based electromagnetic data. *Journal of Geophysical Research*, *112*(5), e2022JA030573. https://doi.org/10.1029/2006JA012069

Haaland, S. E., Paschmann, G., Förster, M., Quinn, J. M., Torbert, R. B., McIlwain, C. E., et al. (2007). High-latitude plasma convection from Cluster EDI measurements: Method and IMF-dependence. *Annales Geophysicae*, *25*(1), 239–253. https://doi.org/10.5194/angeo-25-239-2007

Harang, L. (1946). The mean field of disturbance of polar geomagnetic storms. *Journal of Geophysical Research*, *51*(3), 353. https://doi.org/10.1029/te051i003p00353

Hynönen, R., Tanskanen, E. I., & Francia, P. (2020). Solar cycle evolution of ULF wave power in solar wind and on ground. *Journal of Space Weather and Space Climate*, *10*, 43. https://doi.org/10.1051/swsc/2020046

Juusola, L., Amm, O., & Viljanen, A. (2006). One-dimensional spherical elementary current systems and their use for determining ionospheric currents from satellite measurements. *Earth Planets and Space*, *58*(5), 667–678. https://doi.org/10.1186/BF03351964

Juusola, L., Kauristie, K., Vanhamäki, H., Aikio, A., & van de Kamp, M. (2016). Comparison of auroral ionospheric and field-aligned currents derived from Swarm and ground magnetic field measurements. *Journal of Geophysical Research A: Space Physics*, *121*(9), 9256–9283. https://doi.org/10.1002/2016JA022961

Juusola, L., Vanhamäki, H., Viljanen, A., & Smirnov, M. (2020). Induced currents due to 3D ground conductivity play a major role in the interpretation of geomagnetic variations. *Annales Geophysicae*, *38*(5), 983–998. https://doi.org/10.5194/angeo-38-983-2020

King, J. H., & Papitashvili, N. E. (2005). Solar wind spatial scales in and comparisons of hourly Wind and ACE plasma and magnetic field data. *Journal of Geophysical Research*, *110*(A2), A02104. https://doi.org/10.1029/2004JA010649

Koskinen, H. E. J., & Pulkkinen, T. I. (1995). Midnight velocity shear zone and the concept of Harang discontinuity. *Journal of Geophysical Research*, *100*(A6), 9539. https://doi.org/10.1029/95ja00228

Laundal, K. M., Finlay, C. C., Olsen, N., & Reistad, J. P. (2018). Solar wind and seasonal influence on ionospheric currents from Swarm and CHAMP measurements. *Journal of Geophysical Research: Space Physics*, *123*(5), 4402–4429. https://doi.org/10.1029/2018JA025387

Laundal, K. M., Gjerloev, J. W., Østgaard, N., Reistad, J. P., Haaland, S., Snekvik, K., et al. (2016). The impact of sunlight on high-latitude equivalent currents. *Journal of Geophysical Research A: Space Physics*, *121*(3), 2715–2726. https://doi.org/10.1002/2015JA022236

Laundal, K. M., Reistad, J. P., Hatch, S. M., Madelaire, M., Walker, S. J., Hovland, A. Ø., et al. (2022). Local mapping of polar ionospheric electrodynamics. *Journal of Geophysical Research: Space Physics*, *127*(5), e2022JA030356. https://doi.org/10.1029/2022JA030356

Laundal, K. M., & Toresen, M. (2018). klaundal/pyAMPS: pyAMPS 0.1.0. https://doi.org/10.5281/ZENODO.1182931

Laundal, K. M., Yee, J.-H. H., Merkin, V. G., Gjerloev, J. W., Vanhamäki, H., Reistad, J. P., et al. (2021). Electrojet estimates from mesospheric magnetic field measurements. *Journal of Geophysical Research: Space Physics*, *126*(5), 1–17. https://doi.org/10.1029/2020ja028644

Madelaire, M., Laundal, K. M., Reistad, J. P., Hatch, S. M., & Ohma, A. (2022). Transient high latitude geomagnetic response to rapid increases in solar wind dynamic pressure. *Frontiers in Astronomy and Space Sciences*, *9*, 188. https://doi.org/10.3389/FSPAS.2022.953954/BIBTEX

Marsal, S., Torta, J. M., Segarra, A., & Araki, T. (2017). Use of spherical elementary currents to map the polar current systems associated with the geomagnetic sudden commencements on 2013 and 2015 St. Patrick's Day storms. *Journal of Geophysical Research: Space Physics*, *122*(1), 194–211. https://doi.org/10.1002/2016JA023166

Molinski, T. S. (2002). Why utilities respect geomagnetically induced currents. *Journal of Atmospheric and Solar-Terrestrial Physics*, *64*(16), 1765–1778. https://doi.org/10.1016/S1364-6826(02)00126-8

Newell, P. T., Liou, K., Gjerloev, J. W., Sotirelis, T., Wing, S., & Mitchell, E. J. (2016). Substorm probabilities are best predicted from solar wind speed. *Journal of Atmospheric and Solar-Terrestrial Physics*, *146*, 28–37. https://doi.org/10.1016/j.jastp.2016.04.019

Nosé, M., Iyemori, T., Sugiura, M., & Slavin, J. A. (1995). A strong dawn/dusk asymmetry in Pc5 pulsation occurrence observed by the DE-1 satellite. *Geophysical Research Letters*, *22*(15), 2053–2056. https://doi.org/10.1029/95GL01794

Nykyri, K., Ma, X., Dimmock, A., Foullon, C., Otto, A., & Osmane, A. (2017). Influence of velocity fluctuations on the Kelvin-Helmholtz instability and its associated mass transport. *Journal of Geophysical Research: Space Physics*, *122*(9), 9489–9512. https://doi.org/10.1002/2017JA024374

Oliveira, D. M., & Ngwira, C. M. (2017). Geomagnetically induced currents: Principles. *Brazilian Journal of Physics*, *47*(5), 552–560. https://doi.org/10.1007/s13538-017-0523-y

Olsen, N. (1996). A new tool for determining ionospheric currents from magnetic satellite data. *Geophysical Research Letters*, *23*(24), 3635–3638. https://doi.org/10.1029/96GL02896

Plaschke, F., Hietala, H., Archer, M., Blanco-Cano, X., Kajdič, P., Karlsson, T., et al. (2018). *Jets downstream of collisionless shocks* (Vol. 214). Springer Netherlands. https://doi.org/10.1007/s11214-018-0516-3

Pulkkinen, A., Amm, O., & Viljanen, A. (2003). Separation of the geomagnetic variation field on the ground into external and internal parts using the spherical elementary current system method. *Earth Planets and Space*, *55*(3), 117–129. https://doi.org/10.1186/BF03351739

Pulkkinen, A., Amm, O., Viljanen, A., Korja, T., Hjelt, S. E., Kaikkonen, P., & Tregubenko, V. (2003). Ionospheric equivalent current distributions determined with the method of spherical elementary current systems. *Journal of Geophysical Research*, *108*(A2), 1053. https://doi.org/10.1029/2001JA005085

Richmond, A. (1995). Ionospheric electrodynamics. In H. Volland (Ed.), *Handbook of atmospheric electrodynamics* (Vol. 1, pp. 249–290). CRC Press. https://doi.org/10.1201/9780203713297

Rogers, N. C., Wild, J. A., Eastoe, E. F., Gjerloev, J. W., & Thomson, A. W. (2020). A global climatological model of extreme geomagnetic field fluctuations. *Journal of Space Weather and Space Climate*, *10*, 5. https://doi.org/10.1051/SWSC/2020008

Ronchi, C., Iacono, R., & Paolucci, P. S. (1996). The "Cubed sphere": A new method for the solution of partial differential equations in spherical geometry. *Journal of Computational Physics*, *124*(1), 93–114. https://doi.org/10.1006/jcph.1996.0047

Sadourny, R. (1972). Conservative finite-difference approximations of the primitive equations on quasi-uniform spherical grids. *Monthly Weather Review*, *100*(2), 136–144. https://doi.org/10.1175/1520-0493(1972)100⟨0136:CFAOTP⟩2.3.CO;2

Schillings, A., Palin, L., Opgenoorth, H. J., Hamrin, M., Rosenqvist, L., Gjerloev, J. W., et al. (2022). Distribution and occurrence frequency of dB/dt spikes during magnetic storms 1980–2020. *Space Weather*, *20*(5), e2021SW002953. https://doi.org/10.1029/2021SW002953

Schove, D. J. (1983). Sunspot cycles.

Siscoe, G. L. (2001). 70 years of magnetospheric modeling. In *Geophysical monograph series* (Vol. 125, pp. 211–227). American Geophysical Union (AGU). https://doi.org/10.1029/GM125p0211

Tanskanen, E. I., Slavin, J. A., Tanskanen, A. J., Viljanen, A., Pulkkinen, T. I., Koskinen, H. E., & Eastwood, J. (2005). Magnetospheric substorms are strongly modulated by interplanetary high-speed streams. *Geophysical Research Letters*, *32*(16), 1–4. https://doi.org/10.1029/2005GL023318

Tanskanen, E. I., Viljanen, A., Pulkkinen, T. I., Pirjola, R., Häkkinen, L., Pulkkinen, A., & Amm, O. (2001). At substorm onset, 40% of AL comes from underground. *Journal of Geophysical Research*, *106*(A7), 13119–13134. https://doi.org/10.1029/2000ja900135

Vanhamäki, H., Amm, O., & Viljanen, A. (2003). One-dimensional upward continuation of the ground magnetic field disturbance using spherical elementary current systems. *Earth Planets and Space*, *55*(10), 613–625. https://doi.org/10.1186/BF03352468

Vanhamäki, H., & Juusola, L. (2020). Introduction to spherical elementary current systems. In *Ionospheric multi-spacecraft analysis tools* (pp. 5–33). Springer International Publishing. https://doi.org/10.1007/978-3-030-26732-2{_}2

Vanhamäki, H., Viljanen, A., Pirjola, R., & Amm, O. (2013). Deriving the geomagnetically induced electric field at the Earth's surface from the time derivative of the vertical magnetic field. *Earth Planets and Space*, *65*(9), 997–1006. https://doi.org/10.5047/eps.2013.03.013

Viljanen, A., Nevanlinna, H., Pajunpää, K., & Pulkkinen, A. (2001). Time derivative of the horizontal geomagnetic field as an activity indicator. *Annales Geophysicae*, *19*(9), 1107–1118. https://doi.org/10.5194/angeo-19-1107-2001

Walker, S. J., Laundal, K. M., Reistad, J. P., Hatch, S. M., & Ohma, A. (2022a). 08walkersj/SECpy_Plotting: SECpy_Plotting 0.1.0. https://doi.org/10.5281/zenodo.7138948

Walker, S. J., Laundal, K. M., Reistad, J. P., Hatch, S. M., & Ohma, A. (2022b). Statistics of temporal variations in the auroral electrojets over Fennoscandia [Dataset]. Zenodo. http://www.doi.org/10.5281/zenodo.6505230

Weigel, R. S., Klimas, A. J., & Vassiliadis, D. (2003). Solar wind coupling to and predictability of ground magnetic fields and their time derivatives. *Journal of Geophysical Research*, *108*(A7), 1298. https://doi.org/10.1029/2002JA009627

Weygand, J. M., Amm, O., Angelopoulos, V., Milan, S. E., Grocott, A., Gleisner, H., & Stolle, C. (2012). Comparison between SuperDARN flow vectors and equivalent ionospheric currents from ground magnetometer arrays. *Journal of Geophysical Research*, *117*(5), 5325. https://doi.org/10.1029/2011JA017407

Weygand, J. M., Amm, O., Viljanen, A., Angelopoulos, V., Murr, D., Engebretson, M. J., et al. (2011). Application and validation of the spherical elementary currents systems technique for deriving ionospheric equivalent currents with the North American and Greenland ground magnetometer arrays. *Journal of Geophysical Research*, *116*(3), A03305. https://doi.org/10.1029/2010JA016177

Weygand, J. M., Engebretson, M. J., Pilipenko, V. A., Steinmetz, E. S., Moldwin, M. B., Connors, M. G., et al. (2021). SECS analysis of nighttime magnetic perturbation events observed in Arctic Canada. *Journal of Geophysical Research: Space Physics*, *126*(11), e2021JA029839. https://doi.org/10.1029/2021JA029839

Weygand, J. M., McPherron, R. L., Frey, H. U., Amm, O., Kauristie, K., Viljanen, A., & Koistinen, A. (2008). Relation of substorm onset to Harang discontinuity. *Journal of Geophysical Research*, *113*(4), A04213. https://doi.org/10.1029/2007JA012537

Weygand, J. M., & Wing, S. (2016). Comparison of DMSP and SECS region-1 and region-2 ionospheric current boundary. *Journal of Atmospheric and Solar-Terrestrial Physics*, *143–144*, 8–13. https://doi.org/10.1016/j.jastp.2016.03.002

Yee, J. H., Gjerloev, J., & Wu, D. (2021). Remote sensing of magnetic fields induced by electrojets from space: Measurement techniques and sensor design. In *Space physics and aeronomy, upper atmosphere dynamics and energetics* (pp. 451–468). Wiley. https://doi.org/10.1002/9781119815631.ch21

Zmuda, A. J., Martin, J. H., & Heuring, F. T. (1966). Transverse magnetic disturbances at 1100 kilometers in the auroral region. *Journal of Geophysical Research*, *71*(21), 5033–5045. https://doi.org/10.1029/jz071i021p05033

Paper II

A comparison of auroral oval proxies with the boundaries of the auroral electrojets

S.J. Walker, K.M. Laundal, J.P. Reistad, A. Ohma, S.M. Hatch, G. Chisham, M. Decotte
Space Weather, (Under Review as of October 2023)

Paper III

The Ionospheric Leg of the Substorm Current Wedge: Combining Iridium and Ground Magnetometers

S.J. Walker, K.M. Laundal, J.P. Reistad, S.M. Hatch, A. Ohma, J. Gjerloev
JGR Space Physics, (Under Review as of January 2024)

NORDIC ECOLABEL
241 PRINTED MATTER 731

Graphic design: Communication Division, UiB / Print: Skipnes Kommunikasjon AS

uib.no

ISBN: 9788230864715 (print)
9788230862605 (PDF)